Universitetet i Stavanger

Faculty of Science and Technology

MASTER'S THESIS

Study program / Specialization **Engineering Structures and Materials / Renewable Energy**	Spring Semester, 2020 **Open / ~~Restricted Access~~**
Writer: **Rachel Catherine Zeringue**	Rachel C. Zeringue
Faculty Supervisor: Dr. Charlotte Obhrai	
Thesis Title: **The Influence of Unstable Wind Models on the Motions and Loads of a Semi-Submersible Floating Wind Turbine**	
Credits (ECTS): **30**	
Keywords: Floating Offshore Wind turbine, OC4-DeepCwind, Højstrup's Unstable Spectra Model, Pointed-Blunt Model, Atmospheric Stability, Damage Equivalent loads	Pages: 96 Stavanger 14th July, 2020

Abstract

As the wind turbine industry continues to play a part in the production of energy, the need for larger and more powerful wind turbines keeps increasing. The movement towards offshore wind turbine structures provides opportunities to increase power production, but there are still adjustments that need to come to compensate with the challenges of moving into deeper waters. Floating offshore wind turbines have different structural and environmental factors when compared to onshore or even bottom-fixed offshore wind turbines. The two recommended models for generating wind profiles come from research on onshore wind turbines, with neutral atmospheric stability. In deeper waters, it is much more harmful to ignore the effects of unstable atmospheric stability conditions on the loading of a floating offshore wind turbine (FOWT).

This master's thesis will examine the influence of unstable atmospheric conditions on a FOWT. The OC4-DeepCwind semi-submersible FOWT is the model that has been chosen for this work. To generate the wind profiles, the Pointed-Blunt Model and Højstrup's Unstable Spectra Model will be used to examine the influence of unstable wind on a FOWT. The turbulent wind fields are generated in MATLAB before analysis in SIMA.

In general, it is noted that Højstup's Unstable Spectra Model provides greater turbulence intensity values, greater energy profiles, and greater damage equivalent loads. As the atmospheric stability grows increasingly unstable, Højstrup's Model produces a notable change in the response of the FOWT. The Pointed-Blunt Model has limited change from neutral to unstable to very unstable conditions and generates smaller responses and loads. The tower base fore-aft moment produces the greatest damage equivalent loads in both cases and is affected by both increasing wind speed and the shift from neutral to more unstable conditions. However, there can be improvements to the models and expanding of the simulations that could contribute to a more extensive study.

Acknowledgements

I want to sincerely thank my supervior, Dr. Charlotte Obhrai, and Rieska Mawarni Putri for all the advice and help throughout this semester. I am grateful to have the opportunity to learn from such knowledgeable people in a field I am really passionate about.

I want to thank my family and friends who constantly supported me and provided me with all the opportunities to grow as a student and as a person. I couldn't have done it without their encouragement and support.

To all those random and unplanned moments in life that brought me here, and to all the future moments that will bring me to someplace new in the future.

Stavanger, July 14th, 2020

Rachel Catherine Zeringue

Contents

List of Figures v

List of Tables vi

Nomenclature vii

Abbreviations x

1 Introduction **1**

1.1 Background 1

1.2 Objectives 2

1.3 Scope of Work 2

1.4 Methodology and Organization 3

2 Theory **4**

2.1 Offshore Wind Turbines 4

2.2 Atmospheric Stability 5

2.3 Wind Profiles 7

2.3.1 Power Law wind Profile 9

2.3.2 Logarithmic wind profile 9

2.4 Turbulence and Turbulence Models 13

2.4.1 Turbulence Intensity 14

2.4.2 Wind Spectral Density Function 14

2.4.3 Pointed-Blunt Model 15

2.4.4 Højstrup's Unstable Spectra Model 16

2.5 Coherence Models 19

2.5.1 Davenport Exponential Coherence Model 20

2.5.2 Modified Coherence model 21

2.6 Damage Equivalent Loads 23

3 Methodology **25**

3.1 Semi-Submersible Wind Turbine Model - OC4 DeepCwind 25

3.1.1 Tower Properties 27

3.1.2 Floating Platform Properties 28
3.1.3 Mooring Line Properties 28
3.2 Wind Simulation Model 30
3.2.1 Input Parameters 31
3.2.2 Decay Coefficients 32

4 Results and Discussion **33**
4.1 Wind Spectra 33
4.2 Spectral Densities 34
4.2.1 Tower Base Fore-Aft 34
4.2.2 Tower Base Side-Side 41
4.2.3 Tower Top Torsion Moment 44
4.2.4 Blade Root Flap-Wise 47
4.2.5 Blade Root Edge-Wise 50
4.3 Damage Equivalent Loads 53
4.3.1 Normalized Damage Equivalent Loads 55

5 Conclusion **62**
5.1 Suggestions for Future work 63

A Appendix **A1**
A.1 U-Component Spectra A1
A.2 Spectral Density Results A3
A.2.1 Neutral Results A3
A.2.2 Højstrup's Model, Varying Atmospheric Conditions A11
A.2.3 Pointed-Blunt Model, Varying Atmospheric Conditions A17
A.3 Damage Equivalent Loads A23
A.3.1 Neutral DELs A23
A.3.2 Højstrup Normalized DELs A25
A.3.3 Pointed-Blunt Normalized DELs A27

List of Figures

2.1 Wind Turbine Power curve (From Sohoni, Gupta, and Nema, 2016) . 5

2.2 Wind Speed Profiles with Varying Atmospheric Stability (From Oke, 1978) . . . 6

2.3 Wind Turbine Power curve (From Crasto, 2007) . . . 8

3.1 DeepCwind floating offshore wind turbine design . . . 26

3.2 Distributed Tower Properties . . . 27

3.3 Mooring Line Arrangement . . . 29

3.4 Dimensions and Orientation of the turbulence box (t, Y, Z) . . . 31

4.1 Spectra of the u-component for Højstrup's Model, Very Unstable . . . 34

4.2 Spectral Density for Tower Base Fore-Aft Moment, Højstrup's Model, 8m/s . . . 35

4.3 Spectral Density for Tower Base Fore-Aft Moment, Højstrup's Model, 11.4m/s . . . 36

4.4 Spectral Density for Tower Base Fore-Aft Moment, Højstrup's Model, 15m/s . . . 36

4.5 Spectral Density for Tower Base Fore-Aft Moment, Pointed-Blunt Model, 8m/s . . . 37

4.6 Spectral Density for Tower Base Fore-Aft Moment, Pointed-Blunt Model, 11.4m/s . . . 37

4.7 Spectral Density for Tower Base Fore-Aft Moment, Pointed-Blunt Model, 15m/s . . . 38

4.8 Tower Base Fore-Aft Moment for Højstrup and Pointed-Blunt, 8m/s, Unstable . . . 38

4.9 Tower Base Fore-Aft Moment for Højstrup and Pointed-Blunt, 8m/s, Very Unstable . . . 39

4.10 Tower Base Fore-Aft Moment for Højstrup and Pointed-Blunt, 11m/s, Unstable . . . 39

4.11 Tower Base Fore-Aft Moment for Højstrup and Pointed-Blunt, 11m/s, Very Unstable . . . 40

4.12 Tower Base Fore-Aft Moment for Højstrup and Pointed-Blunt, 15m/s, Unstable . . . 40

4.13 Tower Base Fore-Aft Moment for Højstrup and Pointed-Blunt, 15m/s, Very Unstable . . . 41

4.14 Tower Base Side-Side Moment for Højstrup and Pointed-Blunt, 8m/s, Unstable 42

4.15 Tower Base Side-Side Moment for Højstrup and Pointed-Blunt, 8m/s, Very Unstable 42

4.16 Tower Base Side-Side Moment for Højstrup and Pointed-Blunt, 11m/s, Unstable 43

4.17 Tower Base Side-Side Moment for Højstrup and Pointed-Blunt, 11m/s, Very Unstable 43

4.18 Tower Base Side-Side Moment for Højstrup and Pointed-Blunt, 15m/s, Unstable 44

4.19 Tower Base Side-Side Moment for Højstrup and Pointed-Blunt, 15m/s, Very Unstable 44

4.20 Tower Top Torsion for Højstrup and Pointed-Blunt, 8m/s, Unstable . 45

4.21 Tower Top Torsion for Højstrup and Pointed-Blunt, 8m/s, Very Unstable 45

4.22 Tower Top Torsion for Højstrup and Pointed-Blunt, 11m/s, Unstable 46

4.23 Tower Top Torsion for Højstrup and Pointed-Blunt, 11m/s, Very Unstable 46

4.24 Tower Top Torsion for Højstrup and Pointed-Blunt, 15m/s, Unstable 47

4.25 Tower Top Torsion for Højstrup and Pointed-Blunt, 15m/s, Very Unstable 47

4.26 Blade Root Flap-Wise Moment for Højstrup and Pointed-Blunt, 8m/s, Unstable 48

4.27 Blade Root Flap-Wise Moment for Højstrup and Pointed-Blunt, 8m/s, Very Unstable 48

4.28 Blade Root Flap-Wise Moment for Højstrup and Pointed-Blunt, 11m/s, Unstable 49

4.29 Blade Root Flap-Wise Moment for Højstrup and Pointed-Blunt, 11m/s, Very Unstable 49

4.30 Blade Root Flap-Wise Moment for Højstrup and Pointed-Blunt, 15m/s, Unstable 50

4.31 Blade Root Flap-Wise Moment for Højstrup and Pointed-Blunt, 15m/s, Very Unstable 50

4.32 Blade Root Edge-Wise Moment for Højstrup and Pointed-Blunt, 8m/s, Unstable 51

4.33 Blade Root Edge-Wise Moment for Højstrup and Pointed-Blunt, 8m/s, Very Unstable 51

4.34 Blade Root Edge-Wise Moment for Højstrup and Pointed-Blunt, 11m/s, Unstable 52

4.35 Blade Root Edge-Wise Moment for Højstrup and Pointed-Blunt, 11m/s, Very Unstable 52

4.36 Blade Root Edge-Wise Moment for Højstrup and Pointed-Blunt, 15m/s, Unstable 53

4.37 Blade Root Edge-Wise Moment for Højstrup and Pointed-Blunt, 15m/s, Very Unstable 53

4.38 DEL for the Tower Base Fore-Aft Moment, Højstrup's Unstable Spectra Model 56

4.39 DEL for the Tower Base Fore-Aft Moment, Pointed-Blunt Model . . . 56

4.40 DEL for the Tower Base Fore-Aft Moment, Unstable conditions . . . 57

4.41 DEL for the Tower Base Fore-Aft Moment, Very Unstable conditions 57

4.42 DEL for the Tower Base Side-Side Moment, Unstable conditions . . . 58

4.43 DEL for the Tower Base Side-Side Moment, Very Unstable conditions 58

4.44 DEL for the Tower Top Torsion, Unstable conditions 59

4.45 DEL for the Tower Top Torsion, Very Unstable conditions 59

4.46 DEL for the Blade Root Flap-Wise Moment, Unstable conditions . . 60

4.47 DEL for the Blade Root Flap-Wise Moment, Very Unstable conditions 60

4.48 DEL for the Blade Root Edge-Wise Moment, Unstable conditions . . 61

4.49 DEL for the Blade Root Edge-Wise Moment, Very Unstable conditions 61

List of Tables

2.1 Roughness length z_0 9
2.2 Stability Function at Different Atmospheric Conditions 11
2.3 Atmospheric Stability Classifications 13
3.1 Offshore Wind Turbine Specifications 25
3.2 Frequencies of the Blades for NREL 5MW Wind Turbine 26
3.3 Eigen frequencies for the first 10 modes of the OC4-DeepCwind FOWT 26
3.4 Semi-Submersible Floating Platform Geometry 28
3.5 Mooring System Specifications 29
3.6 Stability Input Parameters 31
3.7 Friction Velocity (m/s) inputs 32
3.8 Decay Coefficients 32
4.1 Turbulence Intensity (%) 33
4.2 Tower Base Fore-Aft Moment 1Hz DEL Values (kNm) 54
4.3 Tower Base Side-Side Moment DEL Values (kNm) 54
4.4 Tower Top Torsion DEL Values (kNm) 54
4.5 Blade Root Flap-Wise Moment DEL Values (kNm) 55
4.6 Blade Root Edge-Wise Moment DEL Values (kNm) 55

Nomenclature

Latin Symbols:

A: cross-sectional area

A: neutral length scale

A_c: Charnock's constant

c: rate of exponential of decay c_p: specific heat of the air at constant pressure

Co: co-spectrum

Cp: power coefficient

c_y: coherence decay constant in the lateral direction

c_z: coherence decay constant in the vertical direction

d_x: grid spacing in the x-direction

d_y: grid spacing in the y-direction

d_z: grid spacing in the z-direction

D: separation distance

D: damage

EA: extensional stiffness

f: non-dimensional reduced frequency

f_i: non-dimensional reduced frequency based on inversion height (z_i)

f_s: sampling frequency

F: force

g: gravity

GJ: torsional stiffness

I_u: turbulence intensity in the longitudinal direction

I_v: turbulence intensity in the lateral direction

I_w: turbulence intensity in the vertical direction

L: Monin-Obukhov length

L_x: length of turbulence box in the longitudinal direction

L_y: length of turbulence box in the lateral direction

L_z: length of turbulence box in the vertical direction

m: Wöhler exponent

n: frequency

n: number of cycles

N: number of time steps

N_f: number of cycles to failure

N_x: number of turbulence box grid points in the longitudinal direction

N_y: number of turbulence box grid points in the lateral direction

N_z: number of turbulence box grid points in the vertical direction

P: power production

P_{rated} rated power production

q: heat flux

Q: quadrature spectrum

Ri: Richardson number

S_eq: damage equivalent load

S_i: considered load range $S_L(n)$: low-frequency part of the spectra

$S_M(n)$: high-frequency part of the spectra

S_u: longitudinal wind spectral density

S_v: lateral wind spectral density

S_w: vertical wind spectral density

S_1 and S_2: power spectra

T_0: mean temperature of the surface layer

U: mean wind speed

u_*: friction velocity

$U(z)$: mean wind speed at height z

U_{hub}: mean wind speed at hub height

U_{ref}: mean wind speed at a reference height

v_*: characteristic velocity scale

z: considered height

z_i: inversion height

z_0: surface roughness

z_{ref}: reference height

Latin Symbols:

α: power-law coefficient

ζ: stability measure

κ: von Kármán constant

ρ: density of air

σ_u: standard deviation of the longitudinal wind component

σ_v: standard deviation of the lateral wind component

σ_w: standard deviation of the vertical wind component

τ: turbulent friction stress

ϕ_ϵ: non0dimensional dissipation rate φ: non-dimensional factor for Richardson number

ψ: stability function

Abbreviations

ABL: Atmospheric Boundary Layer

DEL: Damage Equivalent Load

DNV: Det Norske Veritas

DOWEC: Dutch Offshore Wind Energy Converter

FINO1: Forschungsplattformen in Nord-und Ostsee

FOWT: Floating Offshore Wind Turbine

IEC: International Electrotechnical Commission

MABL: Marine Atmospheric Boundary Layer

NREL: National Renewable Energy Laboratories

OC4: Offshore Code Comparison Collaboration Continuation

PSD: Power Spectral Density

RIFLEX: Riser System Analysis Program

SIMA: Simulation and Engineering Analysis of Marine Operations and Floating Systems

SIMO: Simulation of Marine Operations

SWL: Still water level

TI: Turbulence Intensity

1 Introduction

1.1 Background

Research pertaining to wind turbines, particularly offshore, has become increasingly valuable as the world strives to find sustainable energy solutions to the ever growing energy demand. The principle ways to increase the potential power generation of a wind turbine is to increase the size of the turbine and/or increase the wind speed. Moving to offshore wind turbines provides the space and weather conditions to increase in both areas. However, going offshore does provide considerable drawbacks. The maintenance and installation processes in particular are more costly and complex when compared to onshore turbines. Despite the drawbacks, offshore wind turbines have a greater resource potential and growing support from the industry to push innovation and cost-effectiveness forward.

The average distance of a wind turbine to shore has been increasing steadily throughout the past few decades. In 2001, the average distance of offshore wind turbines from the shore was 5km. by 2013, it was up to almost 30km (Kaldellis & Kapsali, 2013). Moving turbines further away from the shore increases productivity due to the higher wind speeds, but increases complexity as the depth of the ocean increases. Standard monopile foundations becomes less feasible in terms of cost and reliability, so floating foundations are utilized in order to have stabilized wind turbines in deeper waters.

Offshore wind data is limited, so models are essential to approximate wind conditions and fatigue loads that an offshore wind turbine will experience. The International Electrotechnical Commission (IEC) has two recommended standards for wind models: Kaimal Spectra and Exponential Coherence, and the Mann Spectral Tensor Model (TC88-MT, 2005). The issue with these models in terms of offshore wind turbine engineering is that they are not set up to consider unstable

atmospheric conditions. When a turbine is onshore, atmospheric stability is mostly stable, but offshore the predominant atmospheric condition is unstable (Sathe, Mannn, Barlas, Bierbooms, & van Bussel, 2013). There are, however some models that do incorporate unstable atmospheric conditions. The Pointed-Blunt Model was made to be able to simulate wind fields at different atmospheric conditions, from neutral to very unstable (Cheynet, Jakobsen, & Reuder, 2018). Additionally, the Højstrup Unstable Spectra Model emphasizes unstable conditions, which is pertinent for offshore structures (Knight, 2019).

This thesis will be using Højstrup's Unstable Spectra Model and the Pointed-Blunt model to investigate the fatigue loads on a floating semi-submersible offshore wind turbine. There will also be comparisons between the models to examine the differences in loads that the models produce.

1.2 Objectives

The objectives of this master's thesis are as follows:

- Generate turbulent wind fields based on Højstrup's Model and the Pointed-Blunt Model
- Investigate how the different turbulent wind simulations affect a semi-submersible floating wind turbine and compare their results
- See how the wind turbine model responds with the natural frequencies of the offshore wind turbine model
- Investigate the damage response of the wind turbine with both models

1.3 Scope of Work

The scope of work of this master's thesis are as follows:

- MATLAB was used to generate wind profiles and SIMA was used to simulate the wind profiles with the offshore wind turbine model
- The OC4-DeepCwind semi-submersible design was used to model the wind turbine
- The two turbulence models analyzed are the Højstrup Unstable Spectra Model and the Pointed-Blunt Model
- A constant wave input is applied in order to focus purely on the influence of the wind

1.4 Methodology and Organization

This thesis will contain the following:

- Chapter 1: Introduction - includes general information about the thesis regarding the background, objectives, limitations, and organization of the report.
- Chapter 2: Theory - contains information on offshore wind power, atmospheric stability, turbulence and turbulence models, coherences, and damage equivalent loads.
- Chapter 3: Methodology- details the specifications of the models used to represent the wind turbine and how the simulations are set up.
- Chapter 4: Results and Discussion - presentation and discussion of the simulation results including comparison of turbulence intensity, spectral density plots, and damage equivalent loads.
- Chapter 5: Discussion and Conclusion - conclusions on the overall study and recommendations for future work.

2 Theory

2.1 Offshore Wind Turbines

Utilizing offshore wind can have a significant impact on the global energy demand as the technology continues to improve and become more efficient. "Offshore wind turbines continue to get more powerful. On average, turbine capacity has increased by 16% every year since 2014" (Ramírez, Fraile, & Brindley, 2020, p. 17). As the industry continues to go further offshore and produce larger turbines, the potential power production continues to increase. The ability to move offshore means that the turbines are less intrusive for people and can utilize the higher offshore wind speeds, which increases the power production.

The maximum power in the wind going through a turbine depends on the wind speed and the area of rotor blades.

$$P = \frac{1}{2} A \rho U^3 \tag{2.1}$$

Where:

A is the area of the sweep area of the blades

ρ is the air density (1.23 kg/m^3)

U is the wind speed.

However, not all the power in the wind that passes through a wind turbine can be extracted and converted. There is a power coefficient (C_p), which includes the losses from converting kinetic energy from the wind to mechanical energy. The theoretical maximum limit is known as the Betz limit, when $C_p = 0.59$. So, the theoretical maximum power generated from a turbine becomes (Royal Academy of Engineering, 2010):

$$P = \frac{1}{2} A \rho U^3 C_p \tag{2.2}$$

There are more factors that influence the power extraction potential of wind turbines. Inefficiencies in the gearbox and generator of the wind turbine will also create some losses. In practice, extraction is typically around 35-45% as opposed to the theoretical maximum of 59% (Royal Academy of Engineering, 2010).

Wind turbines convert power at certain ranges of wind speeds, shown in Figure 2.1. In region 1, the turbine does not operate because wind speeds are too low. Region 2 starts at the cut in speed, which is where the turbine starts to produce and optimize the power output. In region 3 the turbine continues to produce but the power is capped off at rated power (P_{rated}) by adjusting the pitch angle to avoid high loads. Region 4 starts with the cut out wind speed, meaning the wind speed is too high for the turbine to safely generate power. The blades are pitched to feather to stop the power output.

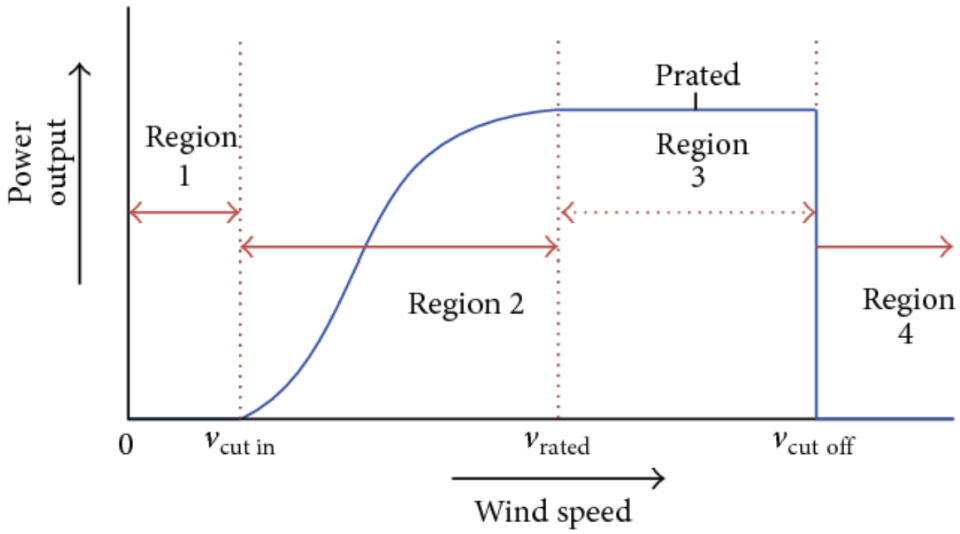

Figure 2.1: Wind Turbine Power curve (From Sohoni, Gupta, and Nema, 2016)

2.2 Atmospheric Stability

Atmospheric stability is defined as the vertical movement of a parcel in the atmosphere (Schroeder & Buck, 1970). There are three characteristics that determine the stability of the atmosphere: "(1) The temperature lapse rate

through the layer; (2) temperature of the parcel at its initial level; and (3) initial dew point of the parcel" (Schroeder & Buck, 1970, p. 50). The temperature lapse rate is the rate at which temperature changes with altitude. The atmosphere is stable if the parcel's vertical movement is being damped. This occurs with a lapse rate of less than 9.8°C per km (The Editors of Encyclopaedia Britannica, 2016). A lapse rate greater than that will favor vertical movement and thus be unstable. This happens when the temperature of the air decreases as the altitude increases. In neutral conditions the parcel and the atmosphere are at the same temperature, so vertical movement is not increased or hindered. (Schroeder & Buck, 1970). Figure 2.2 (b), (c), and (d) show the wind profiles at the various atmospheric stability conditions. (e) shows the same grabs re-plotted on a logarithmic scale to compare the unstable, neutral, and stable conditions.

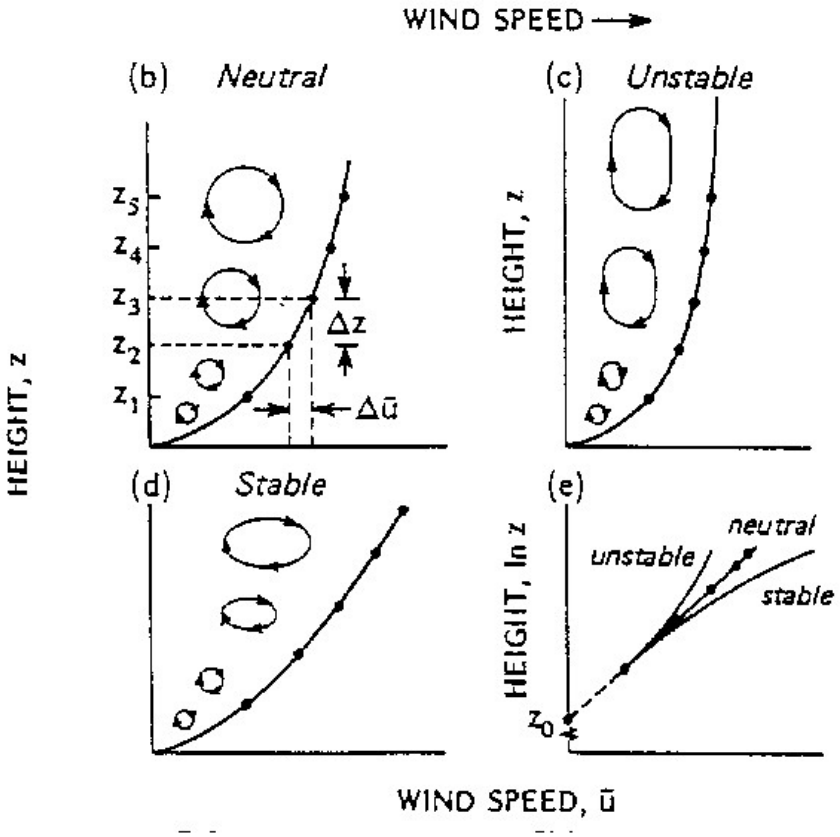

Figure 2.2: Wind Speed Profiles with Varying Atmospheric Stability (From Oke, 1978)

Unstable atmospheric conditions increases the amount of buoyant-generated

turbulence (Putri, 2016). Unstable conditions are more common offshore and can increase fatigue loads on the wind turbine (Knight, 2019). It is characterized by an increased amount of vertical mixing and a lower velocity shear. In contrast, stable conditions are associated with less vertical mixing and a higher velocity shear.

The cycle of stability varies in onshore and offshore conditions. Onshore, the atmospheric stability changes daily. During the night, the cooling of the surface of the earth makes the air close to the surface stay below the warmer air above, creating stable atmospheric conditions. In contrast, during the day, the sunrise heats up the ground and the air close the earth is warmer than the air above, causing it to rise and establish unstable atmospheric conditions (Abdalla, El-Osta, & Dekam, 2017). Since the heat from the sun doesn't affect the ocean in the same way it affects the land on earth, there is no daily change in stability offshore. Instead, there is a seasonal variation. During the summer months, stable conditions are more dominant due to the sea surface being colder than the warm air. In winter, the air temperature is cooler than the sea surface and causes unstable conditions (Krogsæter & Reuder, 2015).

2.3 Wind Profiles

The Earth's atmosphere is made up of four layers: the troposphere, the stratosphere, the mesosphere, and the thermosphere. The troposphere is the closest to Earth and contains the upper potion the free atmosphere and the planetary boundary layer. The planetary boundary layer is generally the governing atmospheric layer for both onshore and offshore wind turbines. The boundary layer contains the Ekman layer and the surface layer. Figure 2.3 shows the wind profile in the planetary boundary layer (also known as the atmospheric boundary layer and referred to as ABL). It is important to distinguish between onshore and offshore when discussing the boundary layer. Due to the variable nature of waves offshore as opposed to the constant level of the ground onshore, the marine atmospheric boundary layer (MABL) is used to refer

to the atmosphere that is in direct contact with the ocean. It will be affected by the exchange of energy, mass, and momentum between the ocean and the atmosphere (Knight, 2019).

Most wind turbines will be inside of the surface layer, where the wind profile is nearly logarithmic. There is a large amount of friction, vertical variation, and turbulence in the surface layer. Additionally, the height of the boundary layer varies dependsing on a roughness value z_0. Open sea has a very low roughness compared to an urban setting, where the buildings and structures influence the movement of the wind. The more obstructions, the greater the friction and shear turbulence, causing high values of z_0 (Putri, 2016)

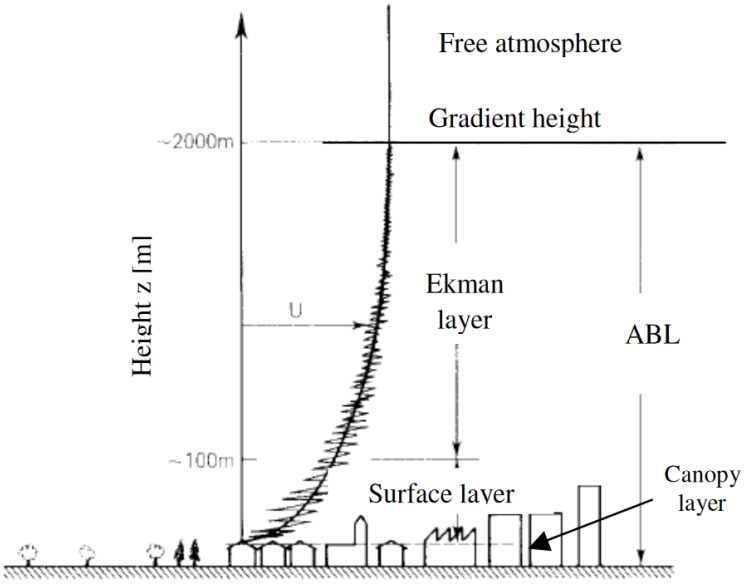

Figure 2.3: Wind Turbine Power curve (From Crasto, 2007)

Due to the variation of the surface layer thickness due to the roughness length z_0, there are ways to estimate the wind speed profile in the surface layer which are dependant on the roughness length. Namely the power law and the logarithmic law. There are different recommendations for the roughness length. DNV recommended practices contains typical values (Table 2.1) based on several previous publications. This also includes the power-law coefficient α, which is relevant for the power law wind profile.

Table 2.1: Roughness length z_0

Terrain type	**Roughness parameter z_0 (m)**	**Power-law coefficient α**
Open sea without waves	0.0001	
Open sea with waves	0.0001-0.01	0.12
Open country without significant buildings and vegetation	0.01	
Cultivated land with scattered buildings	0.05	0.16
Forests and suburbs	0.3	0.30
City centres	1-10	0.40

From (*DNV-RP-C205: Environmental Conditions and Environmental Loads*, 2010, p. 16)

2.3.1 Power Law wind Profile

The power law profile is only valid for neutral atmospheric conditions. The formula utilizes wind speed at a reference height and the power-law coefficient, which describes the atmospheric stability. So the mean wind speed at a height z is:

$$U(z) = U_{ref}\left(\frac{z}{z_{ref}}\right)^{\alpha} \tag{2.3}$$

Where:

z_{ref} is the reference height

U_{ref} is the mean wind velocity at the reference height

z is the height considered

α is the power-law coefficient

2.3.2 Logarithmic wind profile

Also for neutral atmospheric conditions, the logarithmic wind profile describes the mean wind speed at a height z (*DNV-RP-C205: Environmental Conditions and*

Environmental Loads, 2010):

$$U(z) = \frac{u_*}{\kappa} ln\left(\frac{z}{z_0}\right) \tag{2.4}$$

Where:

u_* is the friction velocity = $\sqrt{\overline{uw} + \overline{vw}}$

κ is the von Kármán constant = 0.4

z is the height being considered

z_0 is the roughness length

The surface roughness can be found implicitly from Equation 2.5 rather than from the typical values in Table 2.1. The formula involves Charnock's constant (A_c), which considers the development of waves. Young developing waves have higher values than fully developed waves. A_c between 0.011 and 0.014 is recommended, with the highest values applying for near-coastal locations (*DNV-RP-C205: Environmental Conditions and Environmental Loads*, 2010).

$$z_0 = \frac{A_c}{g}\left(\frac{\kappa U(z)}{ln\left(\frac{z}{z_0}\right)}\right)^2 \tag{2.5}$$

Where:

A_c is Charnock's constant

g is the acceleration of gravity

The logarithmic law can also consider wind speed at reference heights. The equation then becomes:

$$U(z) = U_{ref}\frac{ln\left(\frac{z}{z_0}\right)}{ln\left(\frac{z_{ref}}{z_0}\right)} \tag{2.6}$$

Although the logarithmic wind profile is also valid in neutral conditions, it is possible

to adjust Equations 2.4 and 2.6 by including a stability correction function in order to simulate unstable atmospheric conditions:

$$U(z) = \frac{u_*}{\kappa}\left(ln\frac{z}{z_0} - \psi\right) \tag{2.7}$$

$$U(z) = \frac{ln\left(\frac{z}{z_0}\right) - \psi\left(\frac{z}{L}\right)}{ln\left(\frac{z_{ref}}{z_0}\right) - \psi\left(\frac{z_{ref}}{L}\right)}U_{ref} \tag{2.8}$$

Where:

ψ is the stability function

L is the Monin-Obukhov length (m)

The stability function depends on the stability measure, which is non-dimensional (*DNV-RP-C205: Environmental Conditions and Environmental Loads*, 2010):

$$\zeta = \frac{z}{L} \tag{2.9}$$

ζ is positive for stable conditions, negative for unstable conditions, and $\zeta = 0$ for neutral conditions

Table 2.2: Stability Function at Different Atmospheric Conditions

Stable	**Neutral**	**Unstable**
$\psi = -4.8\zeta$	$\psi = 0$	$\psi = 2\ln(1+x) + \ln(1+x^2) - 2\arctan(x)$ in which $x = (1 - 19.3\zeta)^{1/4}$

The Monin-Obukhov length is "the length scale of energy-containing eddies" (Chougule, Mann, mark Kelly, & Larsen, 2017, p. 949). It is the height when the turbulence is made up of buoyant forces more than shear forces. The

Monin-Obukhov length is defined by (Monin & Obukhov, 1954):

$$L = -\frac{v_*^3}{\kappa \frac{g}{T_0} \frac{q}{c_p \rho}} \tag{2.10}$$

Where:

v_* is the characteristic velocity scale. Typically $v_* = \sqrt{\frac{\tau}{\rho}}$ (τ is the turbulent friction stress and ρ is the density of air)

κ is the von Kármán constant

$\frac{g}{T_0}$ is a dimensional constant (g is the acceleration of gravity and T_0 is the mean temperature of the surface layer)

$\frac{q}{c_p \rho}$ is the temperature flux (q is heat flux and c_p is the specific heat of the air)

The heat flux, q, determines whether the Monin-Obukhov length is positive or negative. When q is negative, L is positive, which means there are stable atmospheric conditions. For unstable atmospheric conditions, q is positive, making L negative. For neutral conditions, q=0 (Monin & Obukhov, 1954).

The Richardson number (Ri) is a dimensionless parameter that establishes if convection is free or forced (*DNV-RP-C205: Environmental Conditions and Environmental Loads*, 2010):

$$Ri = -\frac{g}{\rho_0} \frac{\frac{d\rho_0}{dz}}{\left(\frac{dU}{dz}\right)^2} \tag{2.11}$$

The Richardson equation can be combined with the Monin-Obukhov length using Equation 2.10 to make (Monin & Obukhov, 1954):

$$Ri = \frac{z}{L} \frac{1}{\varphi\left(\frac{z}{L}\right)} \tag{2.12}$$

Where:

$\varphi\left(\frac{z}{L}\right)$ is a non-dimensional factor that is determined with empirical data

When L approaches infinity, or the height of z is relatively small compared to L, $\varphi(0) = 1$. L is then defined as (Monin & Obukhov, 1954):

$$\frac{1}{L} = \left(\frac{\partial Ri}{\partial z}\right)_{z=0} \tag{2.13}$$

The atmospheric stability in this study will be classified with the Monin-Obukhov length with classes from (Gryning, Batchvarova, Brümmer, Jørgensen, & Larsen, 2007):

Table 2.3: Atmospheric Stability Classifications

Obukhov Length (m)	**Atmospheric Stability**
$-100 \leq L \leq -50$	very unstable
$-200 \leq L \leq -100$	unstable
$-500 \leq L \leq -200$	near unstable
$\mid L \mid \geq 500$	neutral
$200 \geq L \geq 500$	near stable
$50 \geq L \geq 200$	stable
$10 \geq L \geq 50$	very stable

2.4 Turbulence and Turbulence Models

Wind turbulence is a large contributor to the fatigue damage experienced by offshore wind turbines. “Wind turbulence is typically characterized using turbulence intensity (TI), which measures the fluctuation of wind speed about its mean value” (Knight, 2019, p. 12). Turbulence acts in the longitudinal (along wind), lateral (cross wind), and vertical (vertical wind) directions. Although the longitudinal wind component contributes the most to the forces on a structure, it is necessary to include all three components in the analysis of a wind turbine due to the flexibility of its structure (Eliassen & Obhrai, 2016). Wind turbulence is characterized by several parameters,

namely turbulence intensity and the spectral density function.

2.4.1 Turbulence Intensity

Turbulence intensity is defined as the ratio of the standard deviation of the velocity fluctuations and the mean wind speed:

$$I_i(z) = \frac{\sigma_i(z)}{U(z)} \tag{2.14}$$

Where:

i is a placeholder for u, v, w; the longitudinal, lateral, and vertical directions

$I_i(z)$ is the turbulence intensity

z is a particular reference height

σ is the standard deviation of the turbulent wind fluctuations

U is the mean wind speed.

Unstable conditions have increased turbulence intensity due to the vertical mixing creating more buoyant-generated turbulence.

2.4.2 Wind Spectral Density Function

The spectral density of a turbulent wind field describes the variation in that wind field and illustrates the energy in the system.

$$S_i(f) = \frac{\sigma_i^2}{df} \tag{2.15}$$

Where:

i represents u, v, w

This can be used to give the power spectral density (PSD) of the wind simulation, which shows the energy of the wind field over the frequency (Putri, 2016):

$$PSD_u(f,z) = \frac{fS_u(f)}{\sigma_u^2(z)} \approx \frac{fS_u(f)}{u_*^2} \tag{2.16}$$

Where:

i stands for the directions u, v, w

$PSD_i(f,z)$ is the power spectral density

$S_i(f)$ is the spectral density function

σ_i^2 is the standard deviation turbulent wind fluctuations

z is the height

u_* is the friction velocity

2.4.3 Pointed-Blunt Model

The Pointed-Blunt Model was made from the combination of 'pointed' low-frequency and 'blunt' high-frequency spectra along with two conditions: "(1) approximations to both the pointed and blunt spectrum models; (2) both S_u and S_w should have the same spectral form" (Cheynet et al., 2018, pp. 437–438). It was constructed using data from the FINO1 research platform from 2007 to 2008. It can be used to characterize velocity spectra at various stability conditions. It is applicable between the range of $-2 < \zeta < 2$, where ζ is the stability measure. The non-dimensional formula for the Pointed-Blunt Model is (Cheynet et al., 2018):

$$\frac{nS_i}{u_*^2} = \frac{a_1^i f}{(1 + b_1^i f)^{5/3}} + \frac{a_2^i f}{1 + b_2^i f^{5/3}} \tag{2.17}$$

Where:

i is a placeholder for directions u, v, w

a_1^i, a_2^i, b_1^i, and b_2^i are floating parameters that depend on the atmospheric stability and/or the measurement height (ranges of these parameters are given in (Cheynet et al., 2018))

The friction velocity, u_*, is found using Equation 2.3

This formula for the Pointed-Blunt Model can be used for all stability conditions within the appropriate range but is best suited for neutral conditions. For stable conditions, the Pointed-Blunt Model is adjusted to show a lower frequency range (Cheynet et al., 2018):

$$\frac{nS_i}{u_*^2} = \frac{a_1^i f}{\left(1 + b_1^i f\right)^{5/3}} + \frac{a_2^i f}{1 + b_2^i f^{5/3}} + a_3 f^{-2} + a_4 f^{-2/3} \tag{2.18}$$

This can be simplified down if mesoscale weather fluctuations become dominant:

$$\frac{nS_i}{u_*^2} \approx c_1 f^{-2/3} + \frac{a_2^i f}{1 + b_2^i f^{5/3}} + a_3 f^{-2} \tag{2.19}$$

The Pointed-Blunt equations depend only on the height (z) because the model was developed without the measurements of the inversion height z_i (Cheynet et al., 2018). In contrast, Højstrup's Unstable Spectra model has three scaling factors: the height z, the inversion height z_i, and the Obukhov length L.

2.4.4 Højstrup's Unstable Spectra Model

Højstrup's 1981 Unstable Spectra Model was created to provide a model that could simulate velocity spectra in the unstable surface layer (Højstrup, 1981). It is similar to the Pointed-Blunt Model in that it combines both the low and high-frequency spectra. Højstrup's Model is built on the foundation of the Kaimal Spectra Model, which is for neutral conditions (Kaimal, Wyngaard, Izumi, & Coté, 1972):

$$\frac{nS_u}{u_*^2} = \frac{105 f}{\left(1 + 33 f\right)^{5/3}} \tag{2.20}$$

$$\frac{nS_v}{u_*^2} = \frac{17f}{(1+9.5f)^{5/3}} \tag{2.21}$$

$$\frac{nS_w}{u_*^2} = \frac{2f}{1+5.3f^{5/3}} \tag{2.22}$$

Where:

n is the frequency (Hz)

f is a non-dimensional reduced frequency $\left(f = \frac{nz}{U}\right)$

$S_{u,v,w}$ is the longitudinal, lateral, and the vertical wind velocity, respectively (Kaimal et al., 1972).

The Kaimal model contains three parts, a low-frequency range (scaled by f_i, a non-dimensional frequency based on the inversion height), a high-frequency range (scaled by f), and an intermediate range (a linear interpolation). Højstrup proposed a formulation that the spectra could be written as a sum of two spectra (Højstrup, 1981):

$$S(n) = S_L(n) + S_M(n) \tag{2.23}$$

Where:

$S_L(n)$ is the low-frequency portion of the spectra

$S_M(n)$ is the high-frequency portion from the Kaimal model.

Højstrup used the formulas for the energy of the wind components from (H. Panofsky, Tennekes, Lenschow, & Wyngaard, 1976):

$$\frac{\sigma_u^2}{u_*^2} = 4.8 + 0.6\left(\frac{z_i}{-L}\right)^{2/3} \tag{2.24}$$

$$\frac{\sigma_u^2}{u_*^2} = 2.7 + 0.6\left(\frac{z_i}{-L}\right)^{2/3} \tag{2.25}$$

$$\frac{\sigma_w^2}{u_*^2} = 1.5 + 2.9\left(\frac{z}{-L}\right)^{2/3} \tag{2.26}$$

Where:

σ^2 is the standard deviation of the wind velocity components

u_* is the friction velocity z_i is the inversion height

L is the Monin-Obukhov length

Equations 2.24 and 2.25 have been rearranged by Højstrup from the original formula given by Panofsky by following the rule that $\sigma_u^2 = \sigma_w^2$ (Højstrup, 1981). With these energy equations and the Kaimal model, Højstup's Unstable Spectra Model becomes:

$$\frac{nS_u}{u_*^2} = \frac{0.5f_i}{1 + 2.2f_i^{5/3}}\left(\frac{z_i}{-L}\right)^{2/3} + \frac{105f}{(1 + 33f)^{5/3}} \tag{2.27}$$

$$\frac{nS_v}{u_*^2} = \frac{0.32f_i}{1 + 1.1f_i^{5/3}}\left(\frac{z_i}{-L}\right)^{2/3} + \frac{17f}{(1 + 9.5f)^{5/3}} \tag{2.28}$$

$$\frac{nS_w}{u_*^2} = \frac{32f}{(1 + 17f)^{5/3}}\left(\frac{z}{-L}\right)^{2/3} + \frac{2f}{1 + 5.3f^{5/3}} \tag{2.29}$$

Where:

z is the height

z_i is the inversion height

f_i is non-dimensionalized frequency based on the inversion height $\left(f_i = \frac{nz_i}{U}\right)$

Højstrup used the expression for the non-dimensional dissipation rate for turbulent kinetic energy $\left(\phi_\epsilon = \frac{kz\epsilon}{u_*^3}\right)$ to adjust the constants in the Unstable Spectra Model in order to produce the correct variance.

As the Monin-Obukhov length goes to infinity (neutral conditions), Equations 2.27,

2.28, and 2.29 reduce to the Kaimal spectrum formulas. With slight changes in the stability measure from neutral to unstable, there is a significant increase in the low-frequency energy in Højstrup's Model that is excluded in the Kaimal Model (Højstrup, 1981).

2.5 Coherence Models

Wind coherence is the normalized cross-spectra of the velocity fluctuations, and can be used to investigate the correlation of turbulence in the frequency domain (Cheynet et al., 2018). Most methods that simulate a turbulent wind field make use of a two-point statistic mean to describe the wind turbulence (Mann, 1998). The coherence of the wind speed fluctuations has traditionally been a function of frequency or spatial scale. There are two parts of the cross spectrum, the co-spectrum and quadrature spectrum. The quadrature spectrum is the imaginary part and the co-coherence is the real part (Cheynet, Jakobsen, & Snæbjörnsson, 2015). Although coherence refers to both the real and imaginary part of the spectrum, the real part of the cross-spectrum is more dominant (Saranyasoontorn, Manuel, & Veers, 2004). Thus, the discussion of coherence in this thesis will refer to the co-coherence of the wind spectrum. Højstrup defines the coherence in the square root definition (Højstrup, 1999):

$$coh(n) = \sqrt{\frac{Q(n)^2 + Co(n)^2}{S_1(n)S_2(n)}} \tag{2.30}$$

Where:

n is the frequency

Q is the quadrature spectrum

Co is the co-spectrum

S_1 and S_2 are the power spectra

Coherence falls between 1 and 0. When the coherence is 1 it means that all

frequencies are correlation across a given separation distance. If the coherence is approaching 0, it means that the the frequencies are insufficiently correlated across a given separation distance (Ropelewski, Tennekes, & Panofsky, 1973).

2.5.1 Davenport Exponential Coherence Model

The Davenport Exponential Coherence model is one of the widely used empirical coherence models. It is a good model for vertical coherence when the length scale of the turbulence is larger than the separation between points. The Davenport Coherence function assumes that the coherence only depends on the rate of exponential decay and the reduced frequency (Saranyasoontorn et al., 2004). The coherence of wind from vertically separated instruments is described as (Davenport, 1961):

$$\gamma(n) = exp\left(-c\left(\frac{nD}{U}\right)\right) \tag{2.31}$$

Where:

γ is the normalized co-spectrum

n is the frequency

c is the rate of exponential decay

$\frac{nD}{U}$ is the reduced frequency f

D is the separation distance

U is the mean wind speed

The equation can be generalized to include horizontal separations (Pielke & Panofsky, 1970):

$$\gamma_j^i(n) = exp\left(-c_j^i \Delta f_j\right) \tag{2.32}$$

Where:

$i = 1, 2, 3$ as an index that refers to the longitudinal, lateral, and vertical wind

components, respectively

$j = 1, 2, 3$ as an index that refers to the longitudinal, lateral, and vertical instrument separations, respectively

f is the reduced frequency

Davenport extended the expression to give the normalized co-spectrum decays horizontally and vertically for two points with a certain separation (Xu, 2013):

$$\gamma(n) = exp\left(-\frac{n}{U}\sqrt{(c_y D_y)^2 + (c_z D_z)^2}\right) \tag{2.33}$$

Where:

c_y and c_z are the lateral and vertical decay coefficients

D_y and D_z are the lateral and vertical separation distance

Decay coefficients are often recommended based on experimental results (Saranyasoontorn et al., 2004).

2.5.2 Modified Coherence model

Despite the fact that the Davenport Coherence Model is widely used, there are some potential problems. There is concern that the single decay coefficient is not enough to accurately represent the wind coherence (Solari, 1987). It has been found that, with large crossing separations, the coherence is not necessarily equal to 1, which means that the Davenport model is significantly overestimating the decay coefficient (Kristensen & Jensen, 1979). A large range of the decay coefficient has been found in practice, likely due to the multiple parameters the coherence depends on, such as spatial separation, measurement height, mean wind speed, atmospheric stability, turbulence intensity, and wind shear (Solari & Piccardo, 2001) (H. A. Panofsky & Mizuno, 1975).

Due to these shortcomings, it can be advantageous to modify the Davenport Model to improve the way it defines wind coherence. Cheynet (2018) developed a two-parameter coherence function in order to account for the dependency of the decay parameter on the spatial separation:

$$\gamma \approx exp\left(-\sqrt{\left(\frac{c_1^i n d_z}{U}\right)^2 + \left(\frac{d_z}{l_2}\right)^2}\right) \tag{2.34}$$

Where:

$d_z = |z_2 - z_1|$

$l_2 = \dfrac{U}{c_2^i}$ with c_2^i being the second decay coefficient and has the dimension of the inverse of time

This can be altered to include a decay coefficient in the y-direction:

$$\gamma \approx exp\left(-\sqrt{\left(\frac{c_y^i n d_y}{U}\right)^2 + \left(\frac{c_z^i n d_z}{U}\right)^2 + \left(\frac{d_z}{l_2}\right)^2}\right) \tag{2.35}$$

Additionally, the decay coefficients defined by Cheynet (2018), consider the atmospheric stability, ranging from $-2 < \zeta < 0.2$:

$$c_1^u = 11.0 + 1.8exp(4.5\zeta) \tag{2.36}$$

$$c_1^v = 7.1 + 3.4exp(6.8\zeta) \tag{2.37}$$

$$c_1^w = 3.5 + 0.7exp(0.7\zeta) \tag{2.38}$$

$$c_2^w = 0.05 + 0.13exp(5.0\zeta) \tag{2.39}$$

The vertical velocity component is the only one where the second decay coefficient has been defined. The second decay coefficient has a stronger dependency on stability than the first (Cheynet et al., 2018).

2.6 Damage Equivalent Loads

The aim of fatigue tests is to determine if a structure can withstand a full spectrum of loads during its operating lifetime. In order to find the equivalent fatigue loads on the wind turbine, the Palmgren-Miner linear damage rule (Miner's Rule) and the rainflow counting algorithm will be utilized together. Both are common methods for fatigue predictions. The rainflow algorithm is often used because of it is able to provide the average value with little error. Most rainflow algorithms use range counting, where two or more ranges are used for cycle determination as opposed to using two points (GopiReddy, Tolbert, & Ozpineci, 2012). Then, Miner's Rule describes the damage variable for each loading stress level (Peng, Huang, Zhou, & Li, 2018):

$$D_i = \frac{n_i}{N_{fi}} \tag{2.40}$$

Where:

D is the damage

n is the number of cycles for the considered stress level

N_f is the total number of cycles to cause failure

i is an iteration to represent the cumulative nature of Miner's rule

Generally, S-N curves (applied stress versus allowable cycles to failure) are used to convert loads to stresses. Due to the difficulty to establish S-N curves at specific components, the fatigue damage can instead be represented with the damage equivalent load (DEL) (Blasques & Natarajan, 2013):

$$S_{eq} = \left(\frac{\sum n_i S_i^m}{n_{eq}} \right)^{1/m} \tag{2.41}$$

Where:

S_{eq} is the damage equivalent load

n_i is the number of cycles

S_i is the considered load range

n_{eq} is a predefined number of cycles

m is the Wöhler exponent

The Wöhler exponent is specific to the type of material. For wind turbines, the relevant materials are glass fiber for the blades and steel for the hub and tower. These materials have a Wöhler exponent of 12 and 3, respectively. The DEL is a conversion from a load time series with varying amplitude to a sinusoidal load time series with a constant amplitude (Sathe et al., 2013).

3 Methodology

3.1 Semi-Submersible Wind Turbine Model - OC4 DeepCwind

The model of the wind turbine comes from the semi-submersible design from Phase II of the Offshore Code Comparison Collaboration Continuation (OC4) project. This model comes from DeepCwind a U.S. project for validating floating offshore wind turbines (Robertson et al., 2014). The specifications of the wind turbine are given in Table 3.1. Additionally, Figure 3.1 shows an illustration of the wind turbine and foundation (Robertson et al., 2014).

Table 3.1: Offshore Wind Turbine Specifications

Parameter	**Turbine Specification**
Power Production	5MW
Rotor Diameter	126m
Foundation	Semi-submersible
Hub height	90m
Cut-in, Rated, and Cut-Out wind Speed	3 m/s, 11.4m/s, 25 m/s
Cut-in and Rated Rotor Speed	6.9 rpm and 12.1 rpm
Control System	variable speed, variable blade-pitch-to-feather

The frequencies of the blades are extremely important for determining the responses of a FOWT. The 1P, 2P, and 3P frequencies shown in Table 3.2 are calculated from the rotor rotation speeds given in the NREL (National Renewable Energy Laboratory) standards. One should also consider the natural frequencies of the system itself. Table 3.3 gives the eigen frequencies of the first 10 modes of the OC4-DeepCwind FOWT (Robertson et al., 2015).

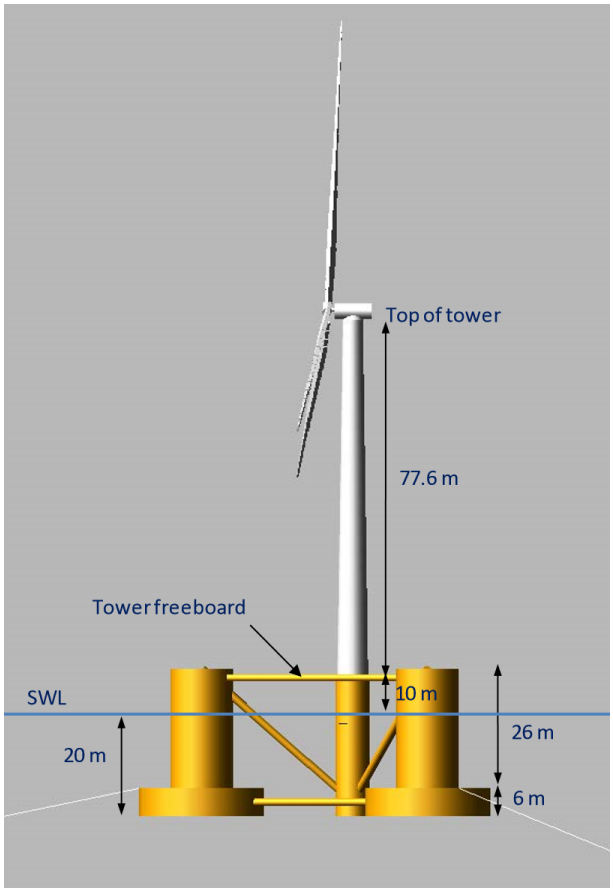

Figure 3.1: DeepCwind floating offshore wind turbine design

Table 3.2: Frequencies of the Blades for NREL 5MW Wind Turbine

Wind speed (m/s)	**Rotor Rotational Frequency (rpm)**	**1P Frequency (Hz)**	**2P Frequency (Hz)**	**3P Frequency (Hz)**
8	9.995	0.16	0.33	0.48
11.4	12.1	0.20	0.40	0.60
15	12.1	0.20	0.40	0.60

Table 3.3: Eigen frequencies for the first 10 modes of the OC4-DeepCwind FOWT

Mode	**Platform Motion**	**Semi-Submersible**
1	Surge	0.01 Hz
2	Sway	0.01 Hz
3	Heave	0.058 Hz
4	Roll	0.04 Hz
5	Pitch	0.04 Hz
6	Yaw	0.012 Hz
7	1^{st} Tower Fore-Aft	0.43 Hz
8	1^{st} Tower Side-Side	0.43 Hz
9	Drivetrain Torsion	0.63 Hz
10	Blade Flap-Wise	0.64 Hz

3.1.1 Tower Properties

As shown in Figure 3.1, the top of the top of the tower is 87.6m above still water level (SWL). This puts the hub height at 90m above SWL. The overall tower mass is 249718kg and the center of mass above SWL (along the tower centerline) is 43.4m. Additionally, the tower has a damping ratio of 1% (Robertson et al., 2014).

The distributed properties of the tower (Table 3.2) are made to match the DOWEC (Dutch Offshore Wind Energy Converter) study in 2003. With the base diameter of the main column of the semi-submersible foundation being 6.5m, tower-base thickness of 0.027m, top diameter of 3.87m and thickness of 0.019m (Robertson et al., 2003). In Figure 3.2 EA stiffness refers to the extensional stiffness while GJ stiffness refers to torsional stiffness (Robertson et al., 2014).

Elev (m)	HtFr (-)	TMassDen (kg/m)	TwFAStif ($N\text{-}m^2$)	TwSSStif ($N\text{-}m^2$)	TwGJStif ($N\text{-}m^2$)	TWEAStif (N)	TwFAIner (kg-m)	TwSSIner (kg-m)
10.0	0.0	4667.00	603.903E+9	603.903E+9	464.718E+9	115.302E+9	24443.7	24443.7
17.76	0.1	4345.48	517.644E+9	517.644E+9	398.339E+9	107.354E+9	20952.2	20952.2
25.52	0.2	4034.76	440.925E+9	440.925E+9	339.303E+9	99.682E+9	17847.0	17847.0
33.28	0.3	3735.44	373.022E+9	373.022E+9	287.049E+9	92.287E+9	15098.5	15098.5
41.04	0.4	3447.32	313.236E+9	313.236E+9	241.043E+9	85.169E+9	12678.6	12678.6
48.80	0.5	3170.40	260.897E+9	260.897E+9	200.767E+9	78.328E+9	10560.1	10560.1
56.56	0.6	2904.69	245.365E+9	245.365E+9	165.729E+9	71.763E+9	8717.2	8717.2
64.32	0.7	2650.18	176.028E+9	176.028E+9	135.458E+9	65.475E+9	7124.9	7124.9
72.08	0.8	2406.88	142.301E+9	142.301E+9	109.504E+9	59.464E+9	5759.8	5759.8
79.84	0.9	2174.77	113.630E+9	113.630E+9	87.441E+9	53.730E+9	4599.3	4599.3
87.60	1.0	1953.87	89.488E+9	89.488E+9	68.863E+9	48.272E+9	3622.1	3622.1

Elev = Elevation
HtFr = Height Fraction
TMassDen = Tower Mass Density
TwFAStif = Tower Fore/Aft Stiffness
TwSSStif = Tower Side/Side Stiffness
TwGJStif = Tower GJ Stiffness
TWEAStif = Tower EA Stiffness
TwFAIner = Tower Fore/Aft Inertia
TwSSIner = Tower Side/Side Inertia

Figure 3.2: Distributed Tower Properties
From (Robertson et al., 2014, p. 4)

3.1.2 Floating Platform Properties

The semi-submersible floating platform consists of a main column that attaches to the tower with three surrounding columns that connect through cross members. The geometry of the semi-submersible platform is outlined in Table 3.4 (Robertson et al., 2014).

Table 3.4: Semi-Submersible Floating Platform Geometry

Depth of platform base below SWL	20m
Elevation of main column (tower base) above SWL	10m
Elevation of offset columns above SWL	12m
Spacing between offset columns	50m
Length of upper columns	26m
Length of base columns	6m
Depth to top of base columns below SWL	14m
Diameter of main column	6.5m
Diameter of offset (upper columns)	12m
Diameter of base columns	24m
Diameter of pontoons and cross braces	1.6m

3.1.3 Mooring Line Properties

The semi-submersible model has 3 mooring lines with 120° between them when viewed from above. Figure 3.3 shows the orientation of the mooring lines. The base of the tower and at the top of the middle semi-submersible column is 10m above sea level. The platform base extends 20m below sea water level and the anchors are at a depth of 200m (Robertson et al., 2014). Further specifications of the mooring system are in Table 3.5

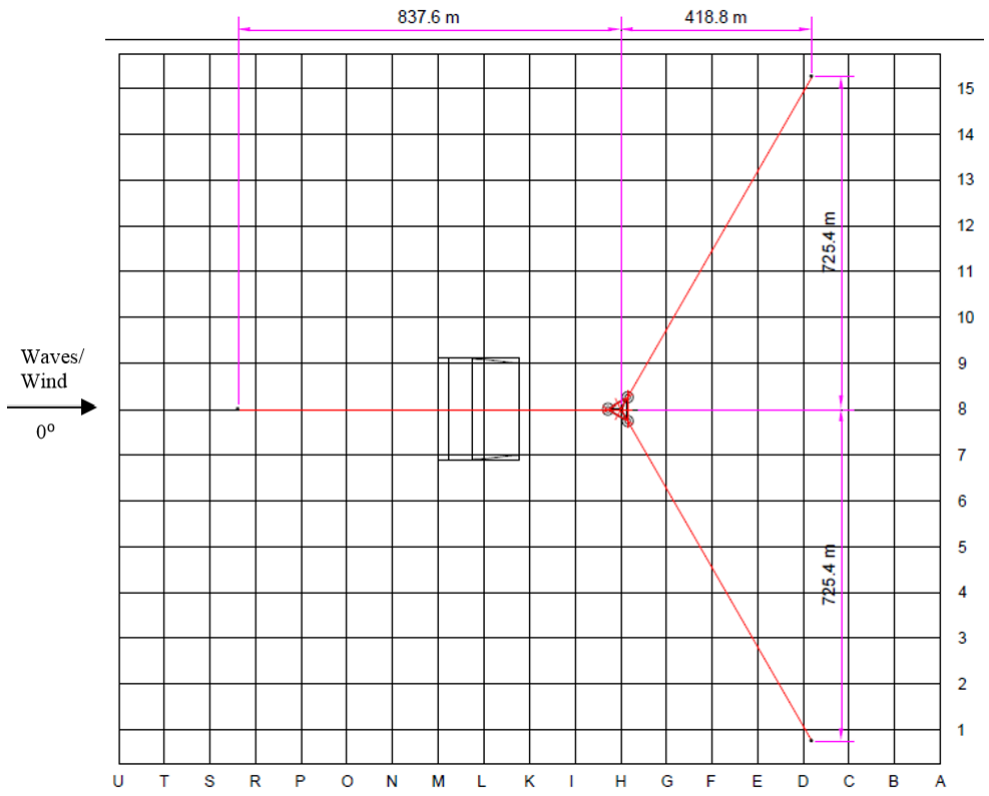

Figure 3.3: Mooring Line Arrangement

Table 3.5: Mooring System Specifications

Parameter	**Turbine Specification**
Depth to fairleads below SWL	14m
Radius to anchors from platform centerline	837.6
Radius to fairleads from platform centerline	40.868m
Unstretched mooring line length	835.5m
Mooring line diameter	0.0766m
Equivalent mooring line mass density	113.35kg/m
Equivalent mooring line mass in water	108.63kg/m
Equivalent mooring line extensional stiffness	753.6MN
Hydrodynamic Drag Coefficient for Mooring Lines	1.1
Hydrodynamic added-mass coefficient for mooring lines	1.0
Seabed drag coefficient for mooring lines	1.0
Structural damping of mooring lines	2.0%

3.2 Wind Simulation Model

MATLAB was used to develop the wind velocity spectra for the u, v, and w components using the Højstrup Model and the Pointed-Blunt Model. The Modified Davenport Coherence was used as the coherence model. Six random seeds were created during simulation of the wind spectra in order to more accurately model the changes in the wind and waves offshore. The six seeds were run at 8m/s, 11.4m/s, and 15m/s to showcase wind conditions below rated, rated, and above rated, respectively.

The function WindSimFast (Cheynet et al., 2018) was used to generate the wind fields that travel though the u-direction in a box that contains the wind profile. The turbulence box is based on previous work by (Putri, 2016) and (Knight, 2019) where the grid is Y by Z over the time duration of the study. The sampling frequency is based on the number of time steps: $N = 2^M$ where M was set to 15. This is the time portion of the turbulence box. That makes the time steps 32768 with a simulation time of one hour (3600 seconds) The sampling frequency is the ratio of time steps to the time duration of the sample. So for these simulations, the sampling frequency (f_s) is 9.1022s.

The Y and Z grid were made to contain the rotor blades and each have 32 nodes with 5m spacing between each node. This creates a t x Y x Z grid with the size of 32768 x 32 x 32. As the time domain goes from 0 to 32768, the wind box moves through the turbine. With the hub height at the center of the box at 90m in height, the box is placed where Y ranges from -77.5 to 77.5 meters and Z ranges from 12.5 to 167.5 meters, shown in Figure 3.4 (Knight, 2019).

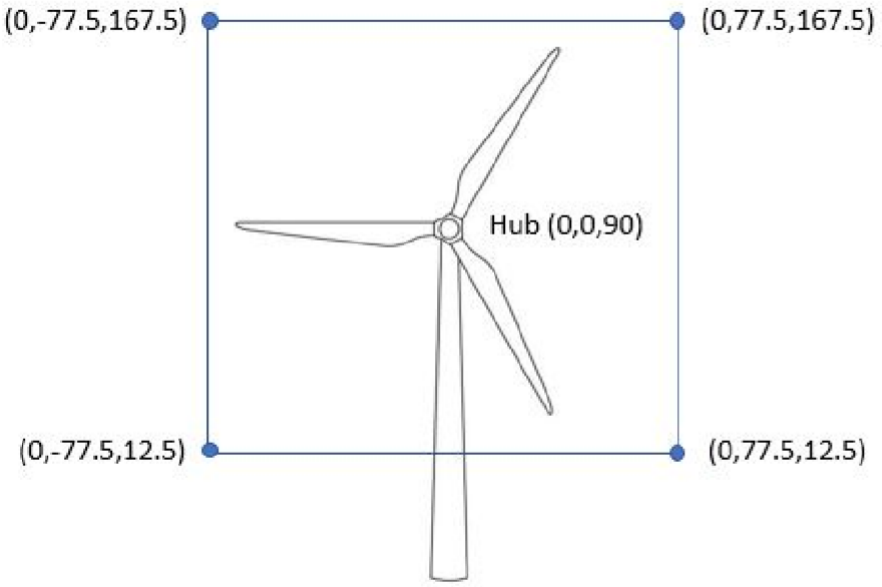

Figure 3.4: Dimensions and Orientation of the turbulence box (t, Y, Z)

3.2.1 Input Parameters

Very unstable conditions correspond with a value of -0.5 for the non-dimensional stability measure (ζ) (Højstrup, 1982). Since the hub height of the wind turbine is 90m, this corresponds to a Monin-Obukhov length (L) of -180m. Similarly, the Monin-Obukhov lengths for unstable and neutral conditions were also found (Table 3.6):

Table 3.6: Stability Input Parameters

Stability	**Stability measure** (ζ)	**Monin-Obukhov Length** (L)
Very Unstable	-0.5	-90m
Unstable	-1.0	-180m
Neutral	0	∞

Friction velocity (u_*) was calculated using Equation 2.4. z_0 was iterated with the starting value of $z_0 = 0.0001$ in Equation 2.5 before being inputted into Equation 2.4. Charnock's constant was approximated within an appropriate range for offshore conditions as 0.011 (*DNV-RP-C205: Environmental Conditions and Environmental Loads*, 2010). z_0 was iterated in order to give a more accurate value for the friction

velocity, instead of assuming an initial friction velocity. Table 3.7 shows the u_* values used in the simulations:

Table 3.7: Friction Velocity (m/s) inputs

	8m/s	**11.4m/s**	**15m/s**
Very Unstable	0.2537	0.3869	0.5386
Unstable	0.2472	0.3763	0.5231
Neutral	0.2323	0.3522	0.4878

3.2.2 Decay Coefficients

The decay coefficients are an important part of the Davenport Coherence function. The decay coefficients used (Table 3.8) come from a previous study (Solari & Piccardo, 2001). That study averaged decay coefficients that had been derived from measurements from each combination of (x,y,z) and (u,v,w) (Solari & Piccardo, 2001).

Table 3.8: Decay Coefficients

c_y^u	c_z^u	c_y^v	c_z^v	c_w^y	c_y^z
7	10	7	10	6.5	3

4 Results and Discussion

4.1 Wind Spectra

The turbulence intensity of the wind spectra were calculated from the u-component (Table 4.1). Under neutral conditions, the TI values are quite similar, although Højstrup's Model generates slightly higher values. However, as the atmospheric stability increases, there is a much greater separation of the two models. The increase of the TI values with Højstrup's Model is significantly greater as the stability is more unstable.

Table 4.1: Turbulence Intensity (%)

	Højstrup			Pointed-Blunt		
	Neutral	Unstable	Very Unstable	Neutral	Unstable	Very Unstable
8m/s	5.93	7.55	8.38	5.80	5.99	6.48
11m/s	6.38	8.03	8.95	6.27	6.49	7.01
15m/s	6.71	8.58	9.51	6.68	6.92	7.47

It is expected for turbulence intensity to increase with increasing wind speed and more unstable conditions due to the higher energy profiles. Figure 4.1 shows how the spectra energy increases with increasing wind speed. The u-component spectra for Højstrup's Model and the Pointed-Blunt Model are included in Appendix A.1. The wind spectra reflects the data given for the turbulence intensities, with neutral conditions being similar between the models and unstable/very unstable conditions showing that Højstrup's Model produces higher spectral energy.

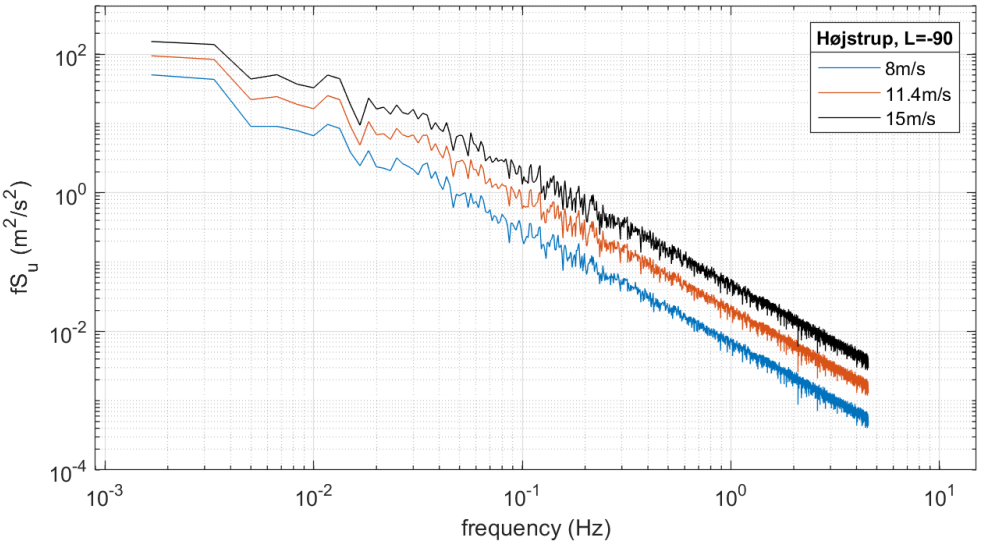

Figure 4.1: Spectra of the u-component for Højstrup's Model, Very Unstable

4.2 Spectral Densities

The Spectral densities are calculated to determine the primary excitations that influence the responses of the FOWT. For this study, the spectral densities will be created for the tower base fore-aft moment, tower base side-side moment, tower top torsion (yaw) moment, blade root flap-wise moment, and blade root edge-wise moment. Additionally, since this should focus on unstable wind conditions, the spectral densities of the neutral conditions for both models will only appear in Appendix A.2.1.

4.2.1 Tower Base Fore-Aft

Figures 4.2 through 4.4 show the spectral density for the tower base fore-aft moment for Højstrup's Spectra Model. As the atmospheric stability becomes more unstable, there is a greater separation between the spectral densities, particularly as the wind speed increases. The difference between unstable and very unstable conditions appears to be less significant than the difference between neutral and unstable. The separation between neutral, unstable, and very unstable remains the

same throughout the spectral densities for Højstrup's Model. Therefore, the results comparing atmospheric stability for the rest of the spectral density moments for Højstrup's Model will be a part of Appendix A.2.2.

The first main excitation is seen slightly above the wave spectral peak (0.0833 Hz). Then, there is an excitation with the 1st tower base fore-aft frequency (0.43 Hz). There is also an excitation at the 6P frequency, which is 0.96 for 8m/s and 1.21 for 11.4m/s and 15 m/s. Additionally in the 11.4m/s and 15m/s conditions, there is a peak around 0.6Hz which would correspond with the 3P frequency. For the 8m/s condition. It is likely that the 3P frequency (0.48Hz) and the 1st tower base fore-aft frequency (0.43Hz) are so close that they are indistinguishable.

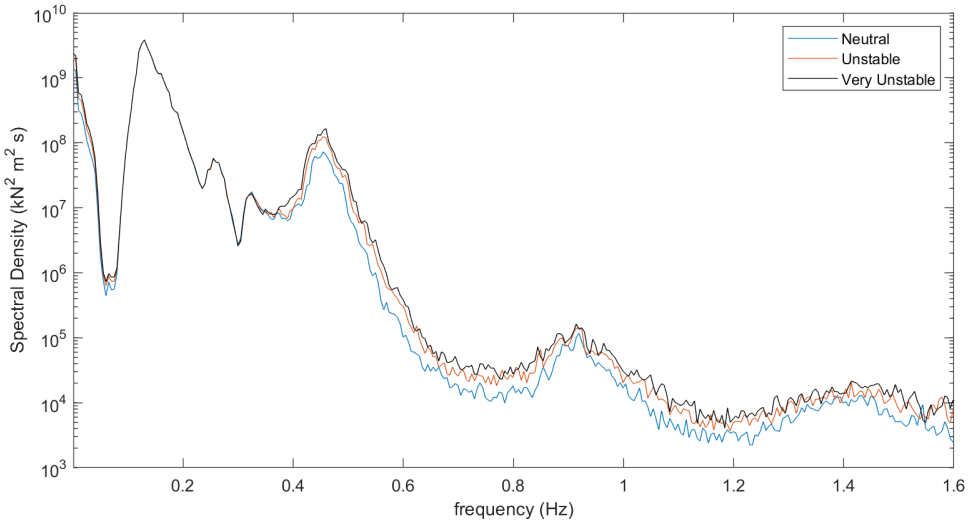

Figure 4.2: Spectral Density for Tower Base Fore-Aft Moment, Højstrup's Model, 8m/s

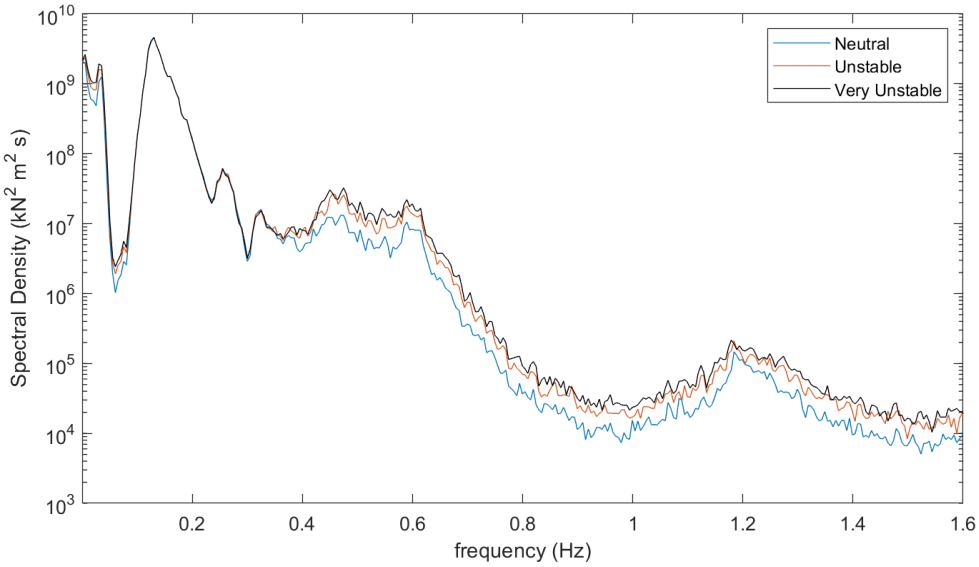

Figure 4.3: Spectral Density for Tower Base Fore-Aft Moment, Højstrup's Model, 11.4m/s

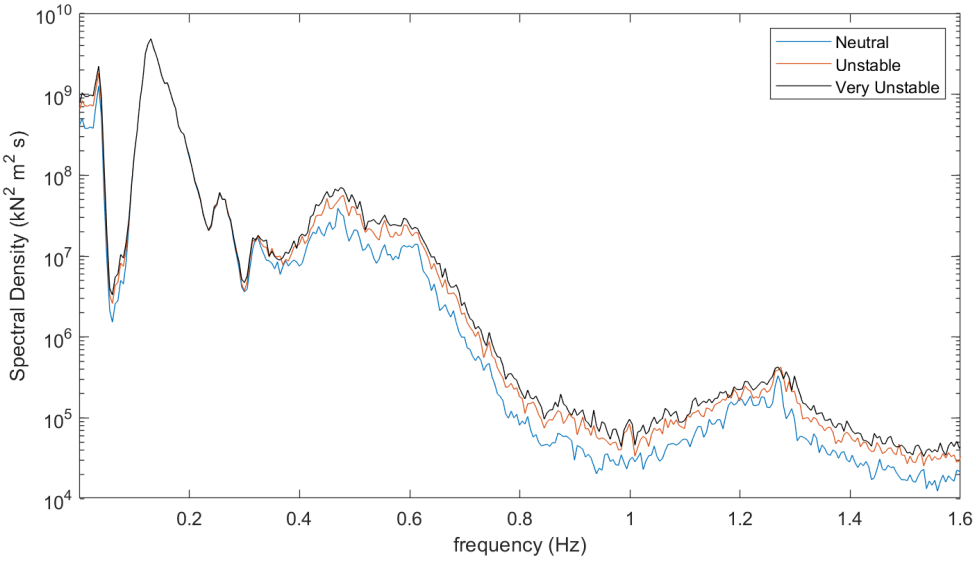

Figure 4.4: Spectral Density for Tower Base Fore-Aft Moment, Højstrup's Model, 15m/s

Figures 4.5 through 4.7 show the spectral density for the tower base fore-aft moment for the Pointed-Blunt Model. There is not a significant separation between neutral, unstable, and very unstable conditions. Throughout the spectral density plots for the Pointed-Blunt Model, the energy content for neutral, unstable, and very unstable remains extremely similar. The only exception being the tower top torsion, which

showed some separation between the different stability conditions. Knowing this, the results comparing atmospheric stability for the rest of the spectral density moments for the Pointed-Blunt Model will be a part of Appendix A.2.3.

As shown with Højstrup's Model, there are excitations near the wave peak, 1st tower base fore-aft frequency, 3P frequency, and 6P frequency.

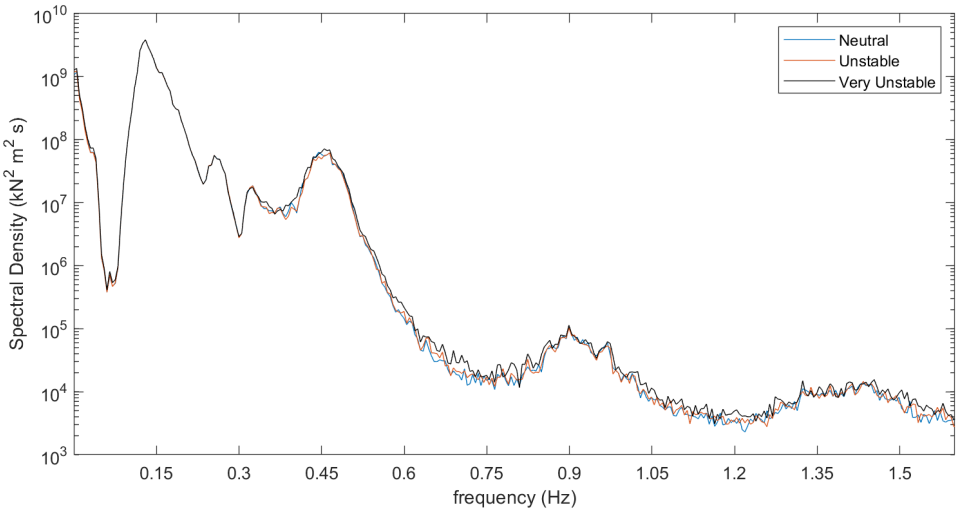

Figure 4.5: Spectral Density for Tower Base Fore-Aft Moment, Pointed-Blunt Model, 8m/s

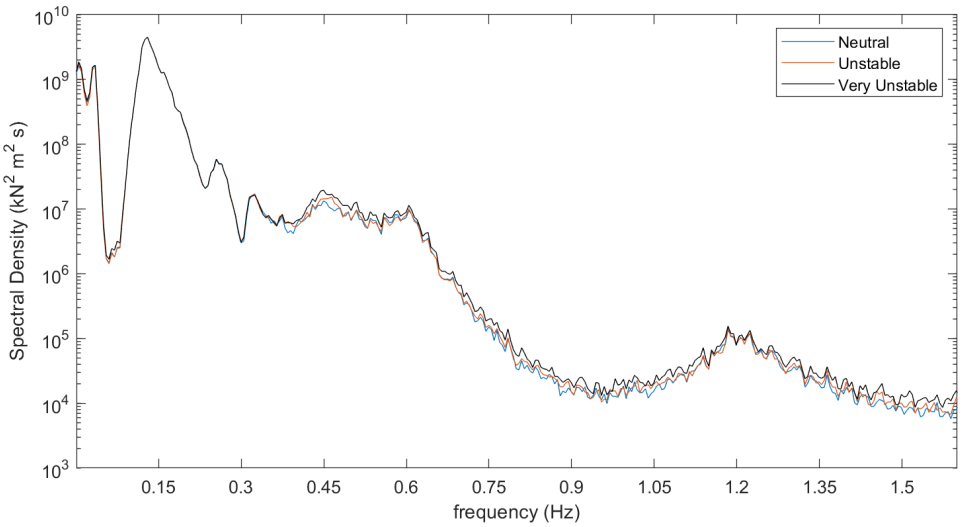

Figure 4.6: Spectral Density for Tower Base Fore-Aft Moment, Pointed-Blunt Model, 11.4m/s

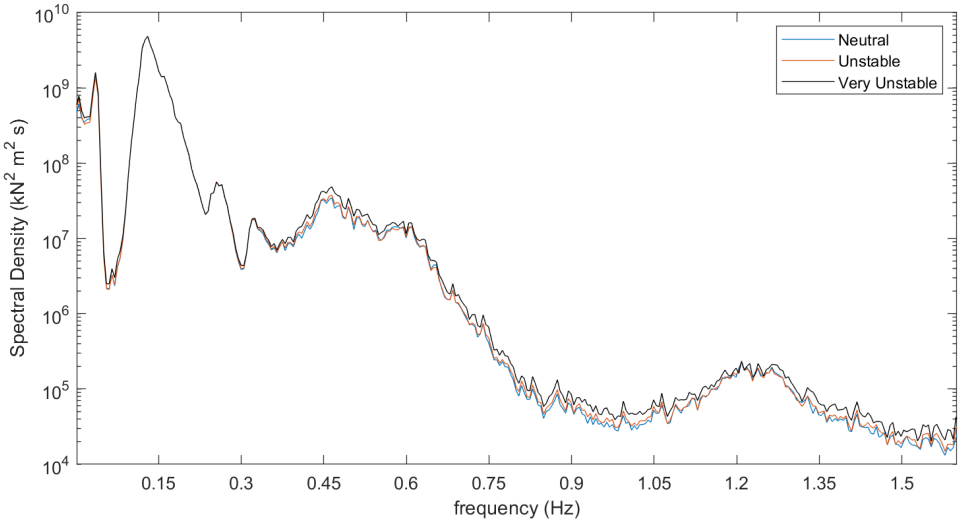

Figure 4.7: Spectral Density for Tower Base Fore-Aft Moment, Pointed-Blunt Model, 15m/s

Figures 4.8 to 4.13 give a comparison of the two models for unstable and very unstable conditions. The energy content is not drastically different, but there is some separation, with Højstrup giving a higher spectral density profile in all cases.

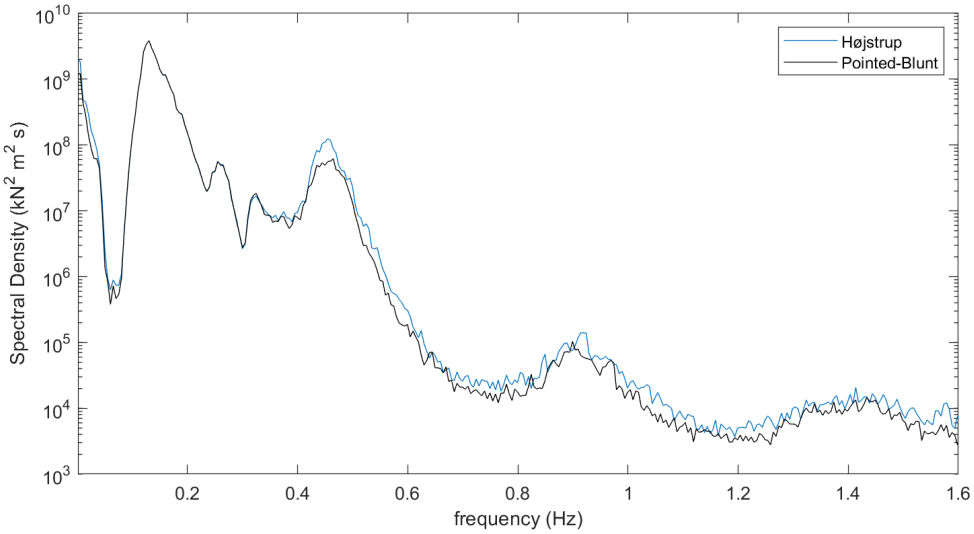

Figure 4.8: Tower Base Fore-Aft Moment for Højstrup and Pointed-Blunt, 8m/s, Unstable

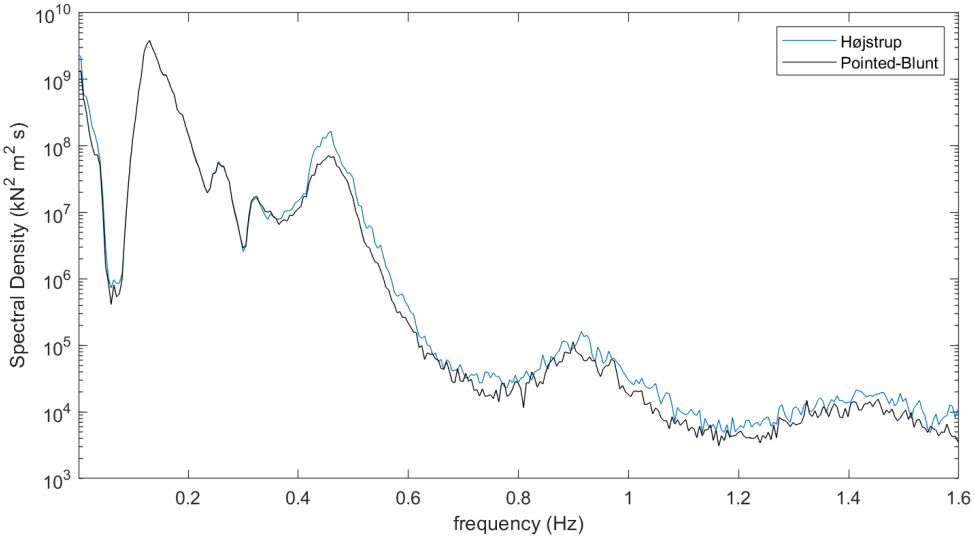

Figure 4.9: Tower Base Fore-Aft Moment for Højstrup and Pointed-Blunt, 8m/s, Very Unstable

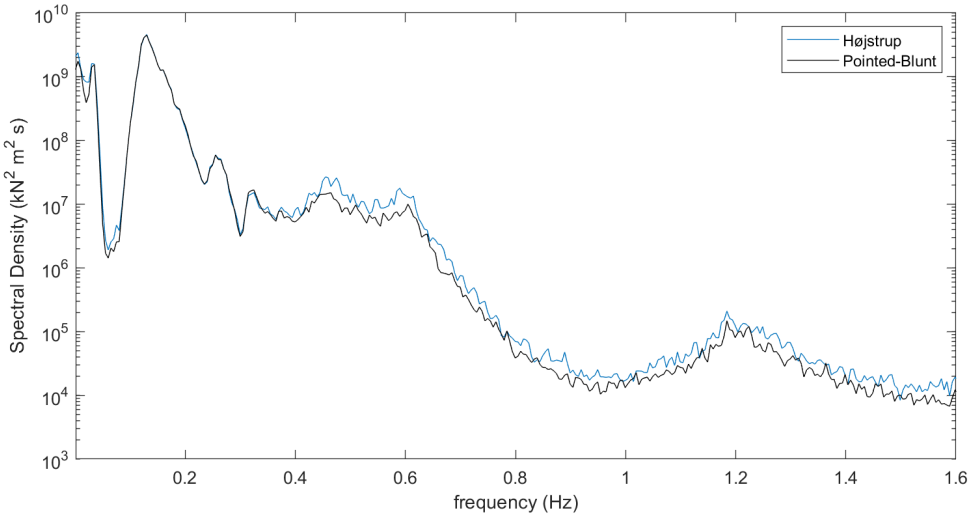

Figure 4.10: Tower Base Fore-Aft Moment for Højstrup and Pointed-Blunt, 11m/s, Unstable

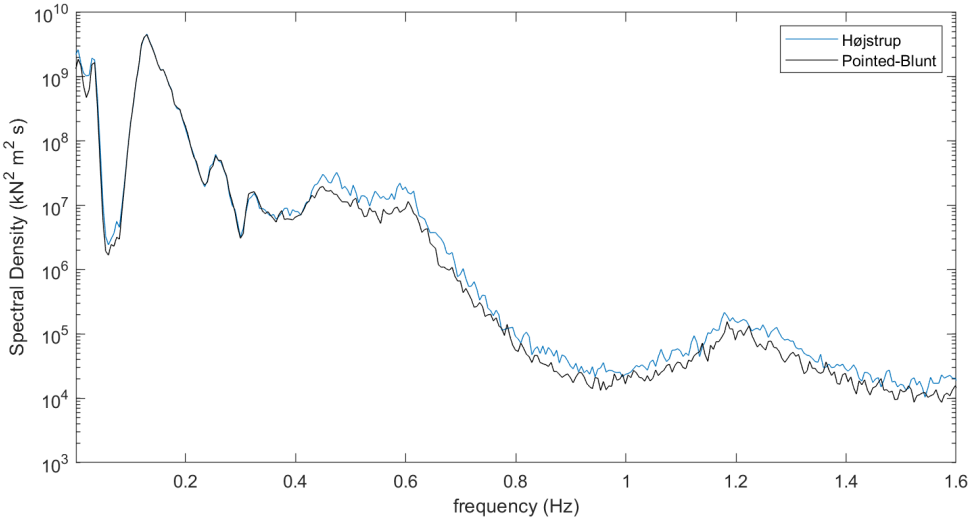

Figure 4.11: Tower Base Fore-Aft Moment for Højstrup and Pointed-Blunt, 11m/s, Very Unstable

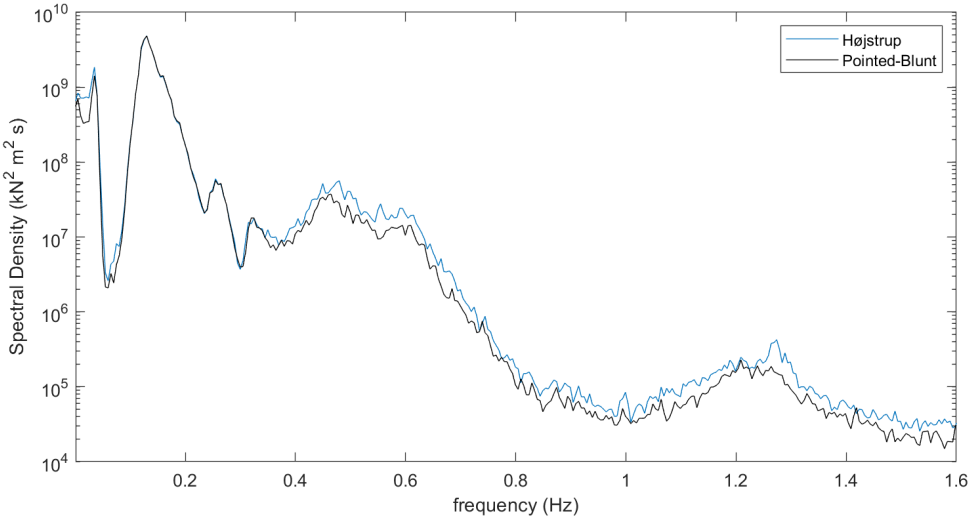

Figure 4.12: Tower Base Fore-Aft Moment for Højstrup and Pointed-Blunt, 15m/s, Unstable

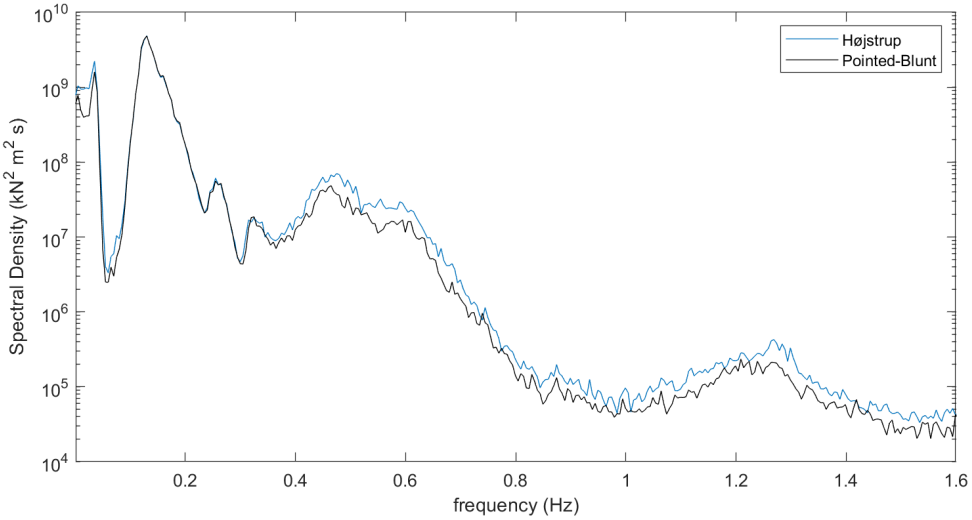

Figure 4.13: Tower Base Fore-Aft Moment for Højstrup and Pointed-Blunt, 15m/s, Very Unstable

4.2.2 Tower Base Side-Side

The tower base side-side moment spectral densities (Figures 4.14 to 4.19) show similar excitation responses due to the wave peak, 1st tower side-side frequency (0.43Hz), 3P and 6P frequency. conditions. Additionally, there is a much greater increase in the energy content as the wind speed increases, particularly going from below rated to rated wind speed. The 1st tower side-side frequency seems to have the most excitation influence on the spectral density.

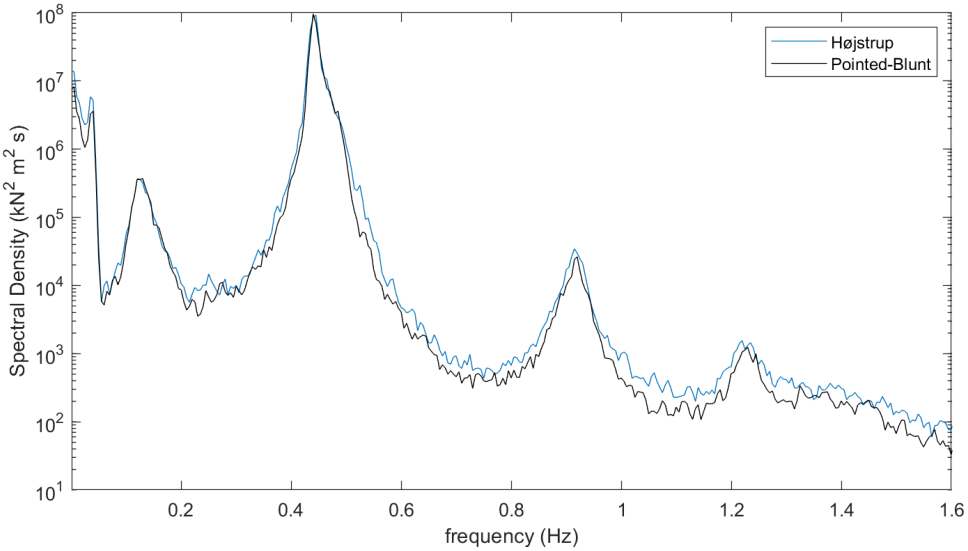

Figure 4.14: Tower Base Side-Side Moment for Højstrup and Pointed-Blunt, 8m/s, Unstable

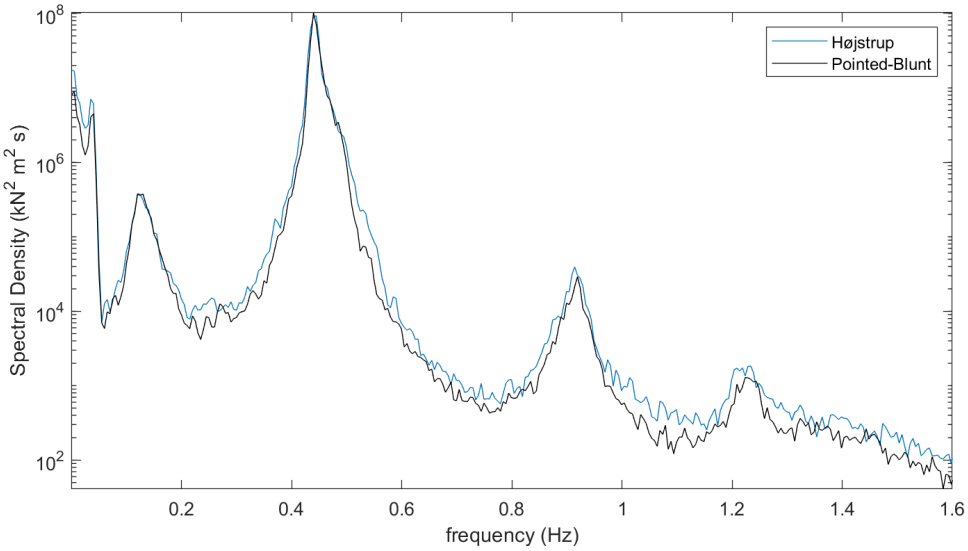

Figure 4.15: Tower Base Side-Side Moment for Højstrup and Pointed-Blunt, 8m/s, Very Unstable

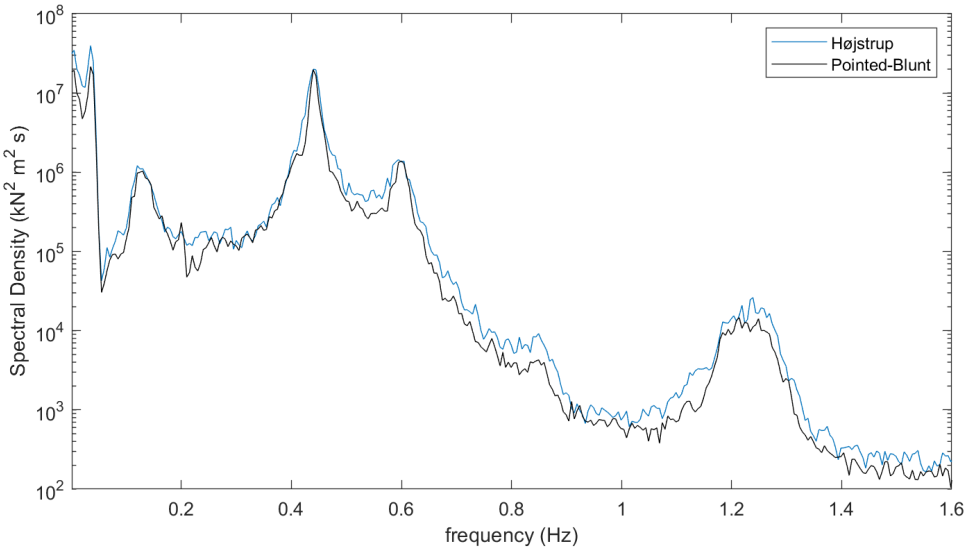

Figure 4.16: Tower Base Side-Side Moment for Højstrup and Pointed-Blunt, 11m/s, Unstable

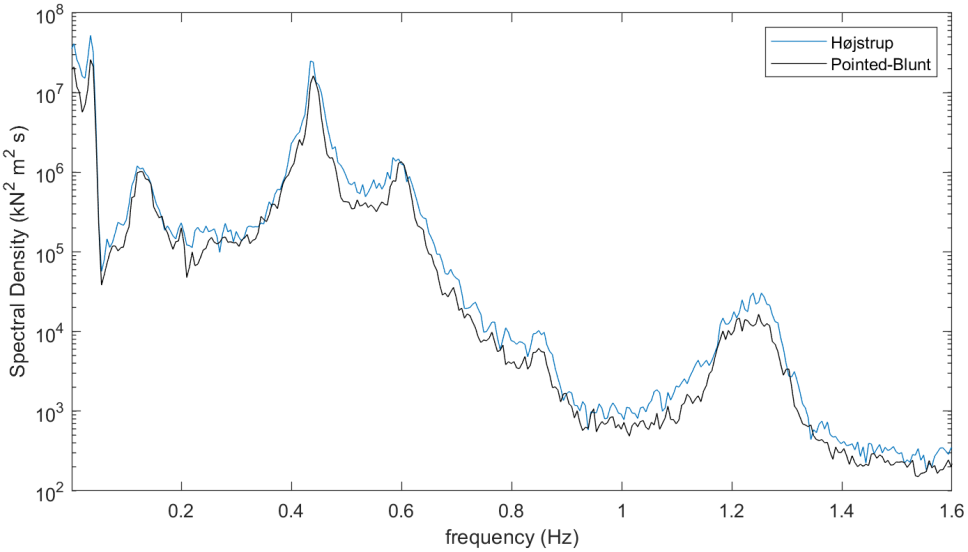

Figure 4.17: Tower Base Side-Side Moment for Højstrup and Pointed-Blunt, 11m/s, Very Unstable

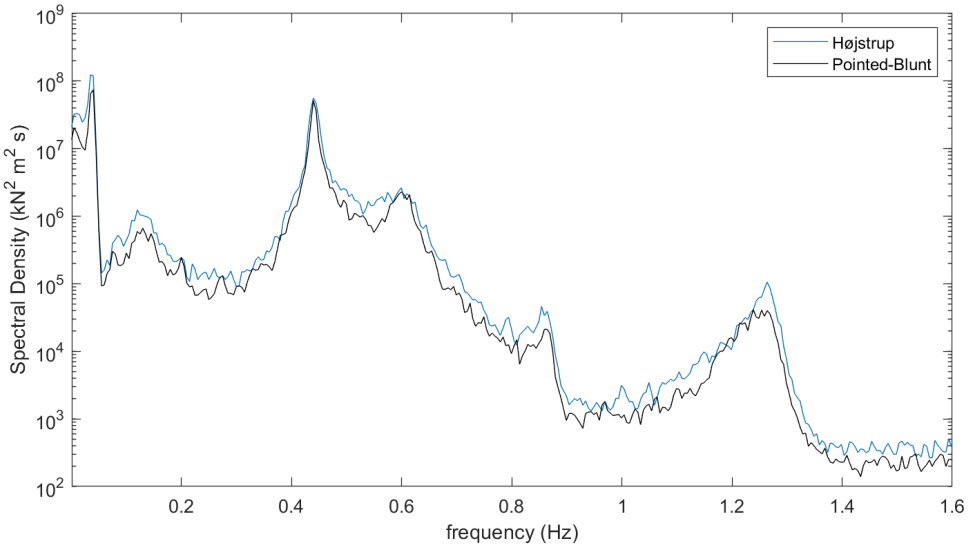

Figure 4.18: Tower Base Side-Side Moment for Højstrup and Pointed-Blunt, 15m/s, Unstable

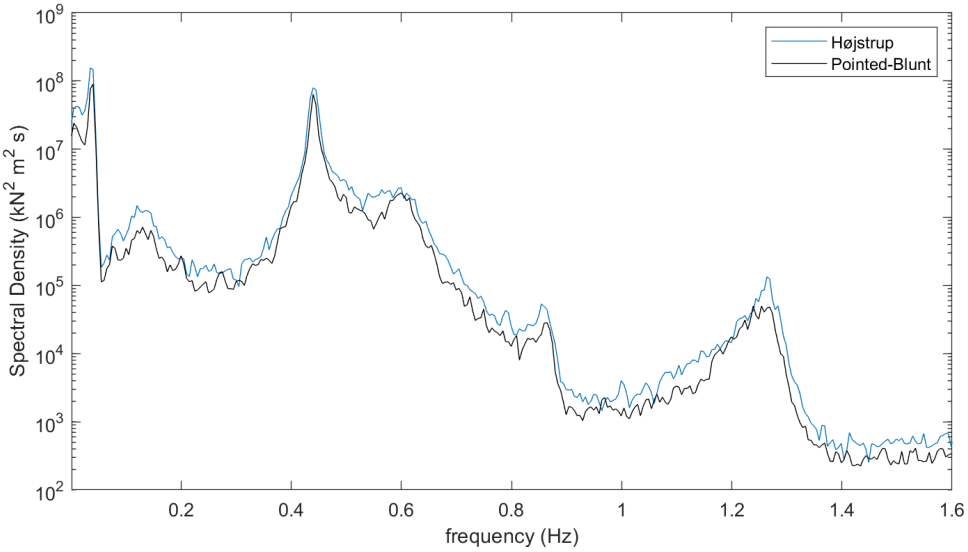

Figure 4.19: Tower Base Side-Side Moment for Højstrup and Pointed-Blunt, 15m/s, Very Unstable

4.2.3 Tower Top Torsion Moment

The tower top torsion spectral densities, Figures 4.20 to 4.25, show slightly more separation between the models. However, they both contain excitations at the wave peak, 3P frequency, and 6P frequency. As the wind speed increases, the wave spectral

peak (0.0833Hz) diminishes.

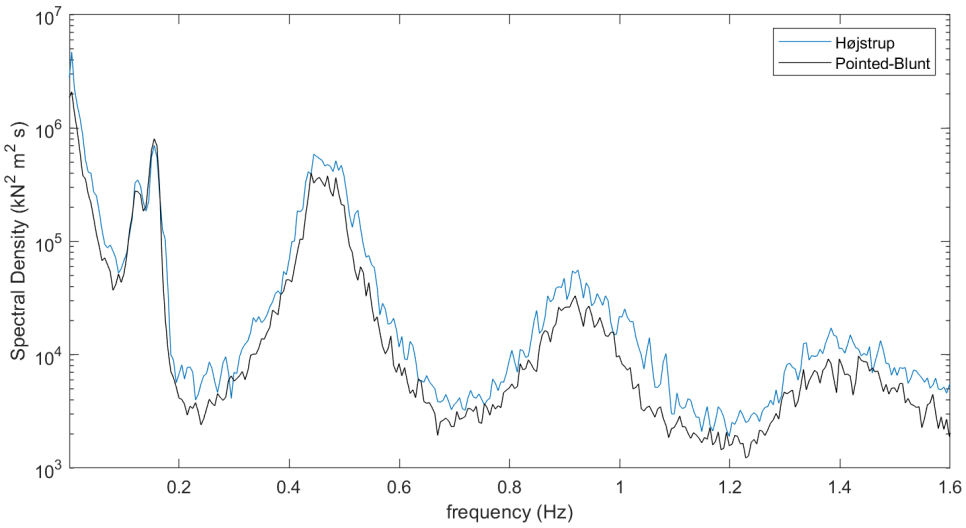

Figure 4.20: Tower Top Torsion for Højstrup and Pointed-Blunt, 8m/s, Unstable

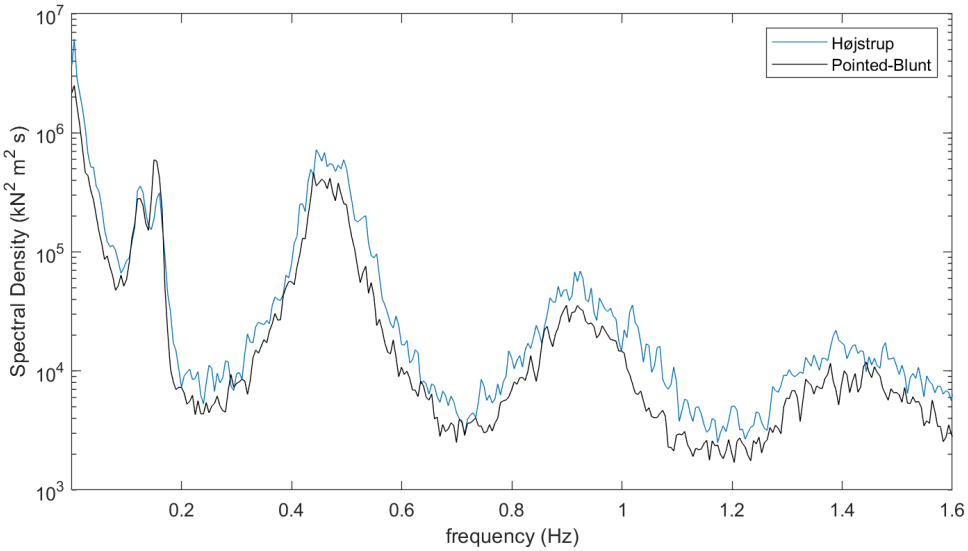

Figure 4.21: Tower Top Torsion for Højstrup and Pointed-Blunt, 8m/s, Very Unstable

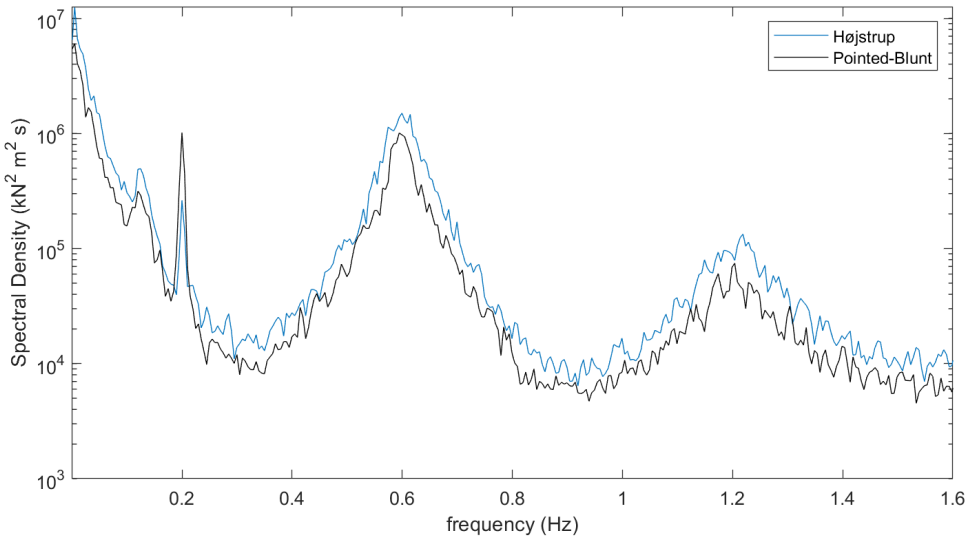

Figure 4.22: Tower Top Torsion for Højstrup and Pointed-Blunt, 11m/s, Unstable

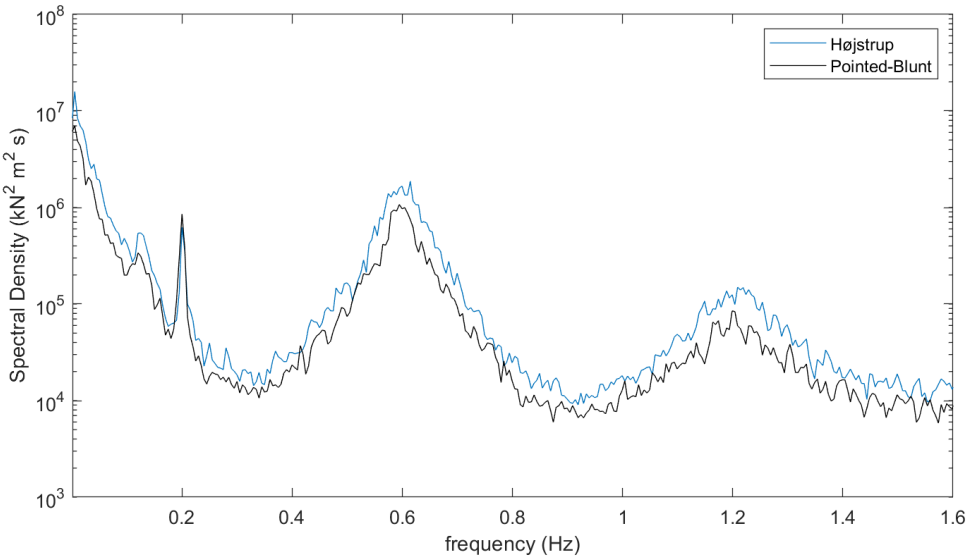

Figure 4.23: Tower Top Torsion for Højstrup and Pointed-Blunt, 11m/s, Very Unstable

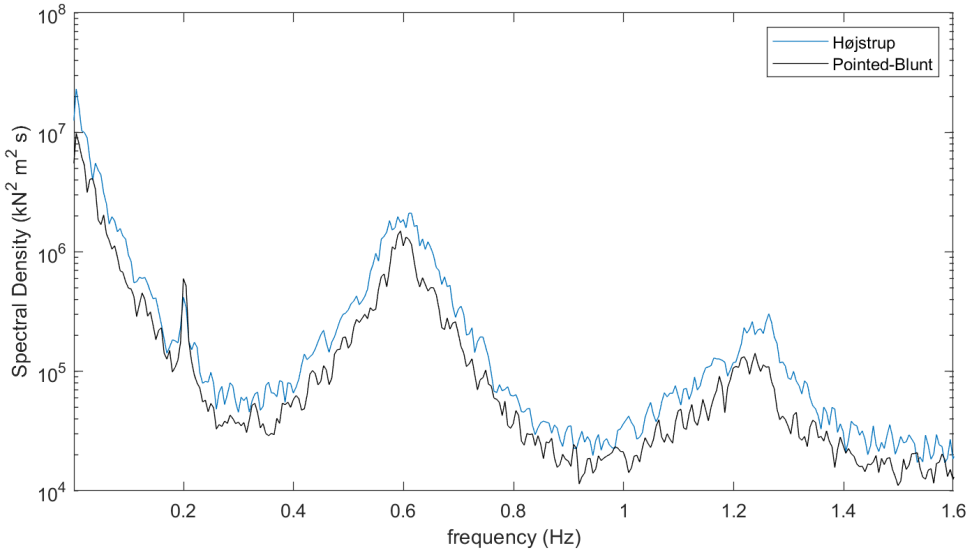

Figure 4.24: Tower Top Torsion for Højstrup and Pointed-Blunt, 15m/s, Unstable

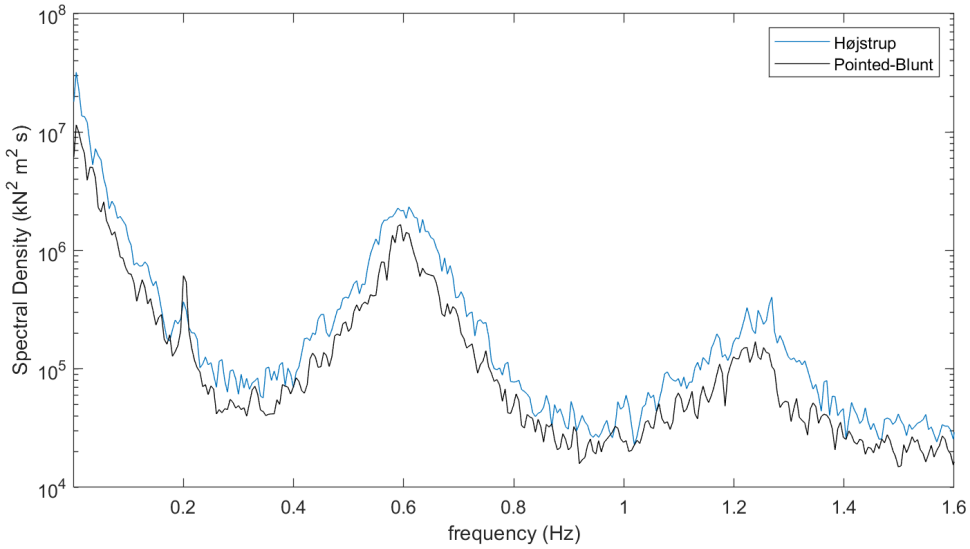

Figure 4.25: Tower Top Torsion for Højstrup and Pointed-Blunt, 15m/s, Very Unstable

4.2.4 Blade Root Flap-Wise

The spectral densities for the blade root flap-wise moment are shown in Figures 4.26 to 4.31. The blade root flap-wise moment is most effected by the rotational frequencies 1P, 2P, 3P, 4P and possibly 5P at the higher wind speeds. At rated and above rated wind speeds, there is a slight excitation due to the platform pitch

(0.04Hz) that is not seen at below rated wind speeds. Overall the energy content is similar throughout all wind speeds. However, the excitation due to the 1P frequency for 15m/s (0.2Hz) is notably higher than at the smaller wind speeds.

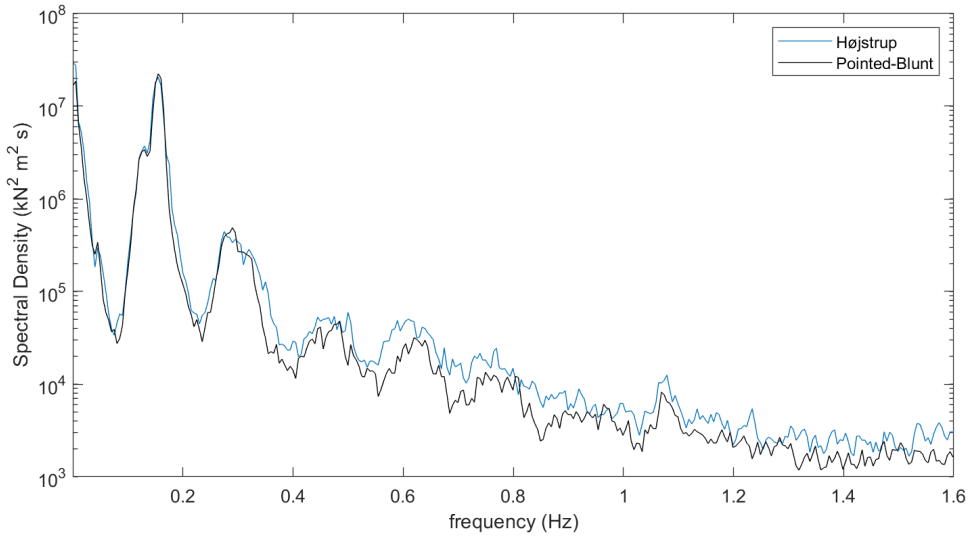

Figure 4.26: Blade Root Flap-Wise Moment for Højstrup and Pointed-Blunt, 8m/s, Unstable

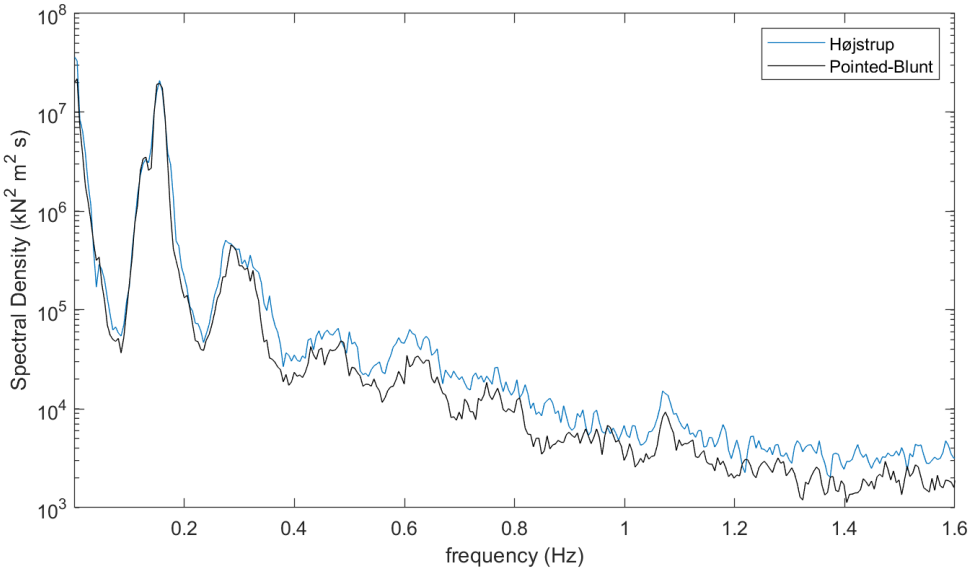

Figure 4.27: Blade Root Flap-Wise Moment for Højstrup and Pointed-Blunt, 8m/s, Very Unstable

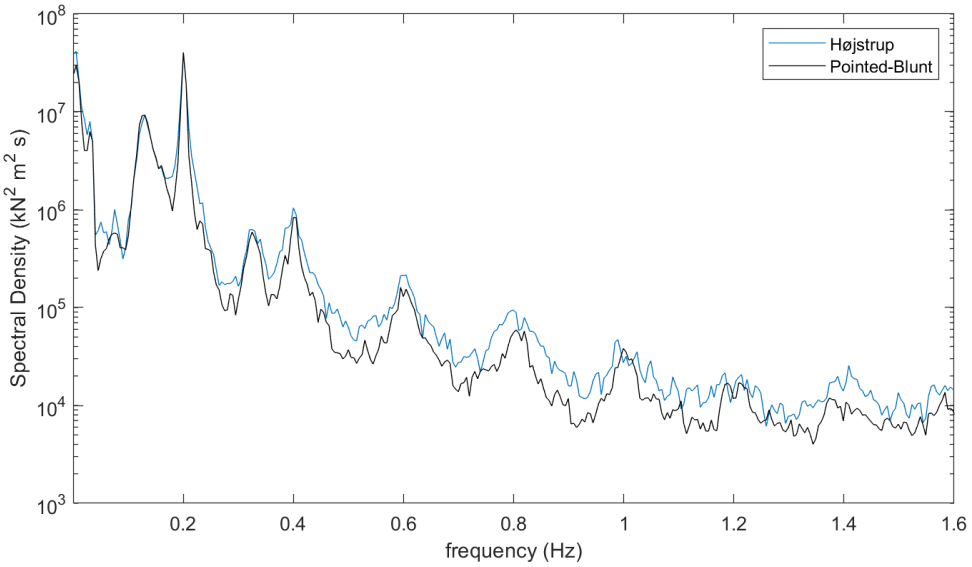

Figure 4.28: Blade Root Flap-Wise Moment for Højstrup and Pointed-Blunt, 11m/s, Unstable

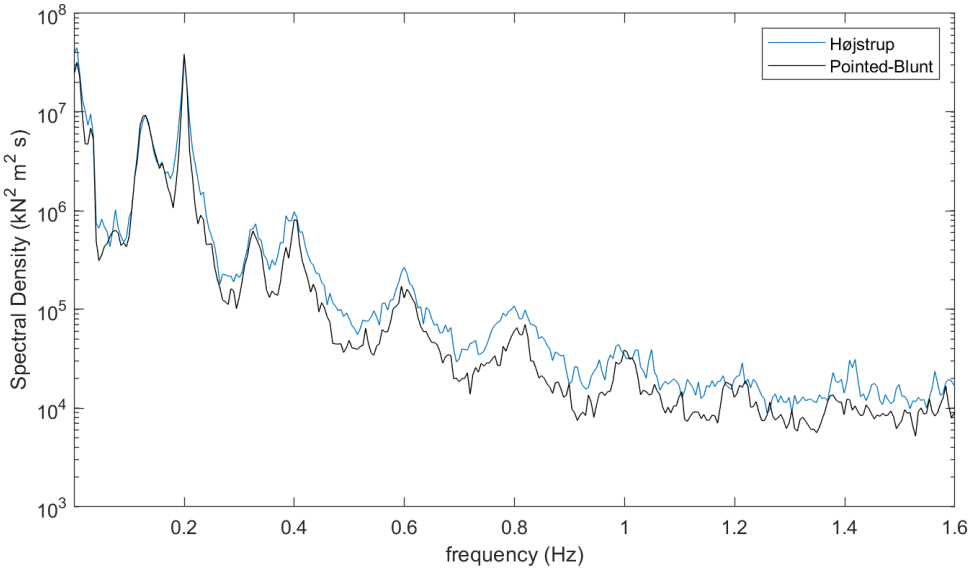

Figure 4.29: Blade Root Flap-Wise Moment for Højstrup and Pointed-Blunt, 11m/s, Very Unstable

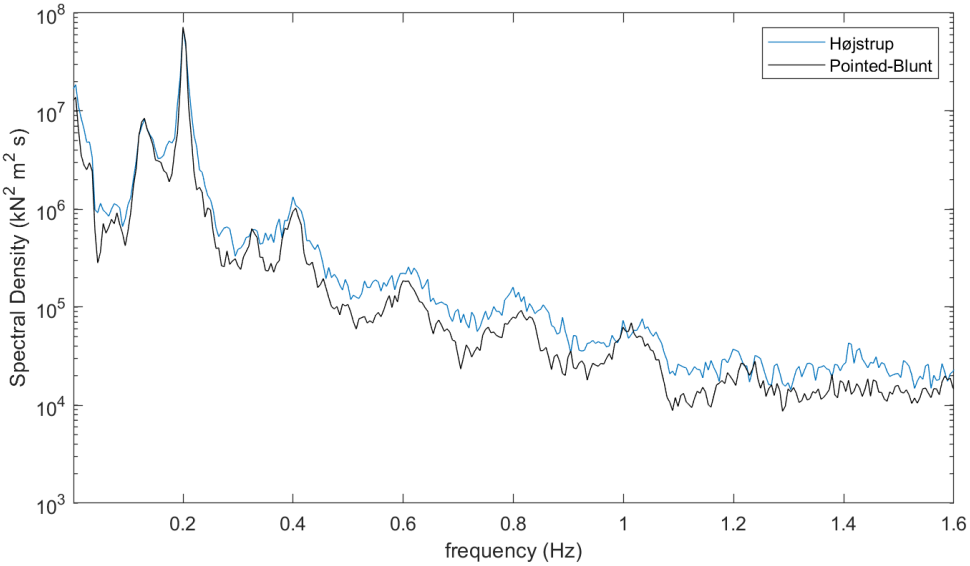

Figure 4.30: Blade Root Flap-Wise Moment for Højstrup and Pointed-Blunt, 15m/s, Unstable

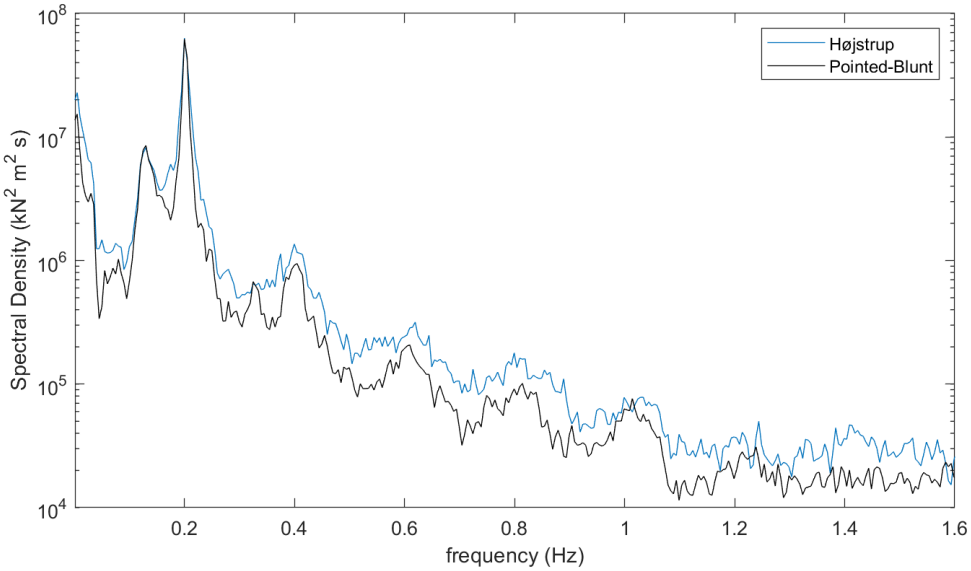

Figure 4.31: Blade Root Flap-Wise Moment for Højstrup and Pointed-Blunt, 15m/s, Very Unstable

4.2.5 Blade Root Edge-Wise

For the blade root edge-wise (Figures 4.32 to 4.37, the difference between the two models seems to be smaller. The excitations remain the same as the ones for the blade root flap-wise. Namely the wave peak, 1P, 2P, 3P, 4P, with the 5P as well

for rated and above rated wind speeds. Additionally the final rotational frequency seems to be quite large instead of getting progressively smaller as seen in the spectral densities for the blade root flap-wise moment. There is also a significant increase in the energy content when going from below rated to rated wind speed.

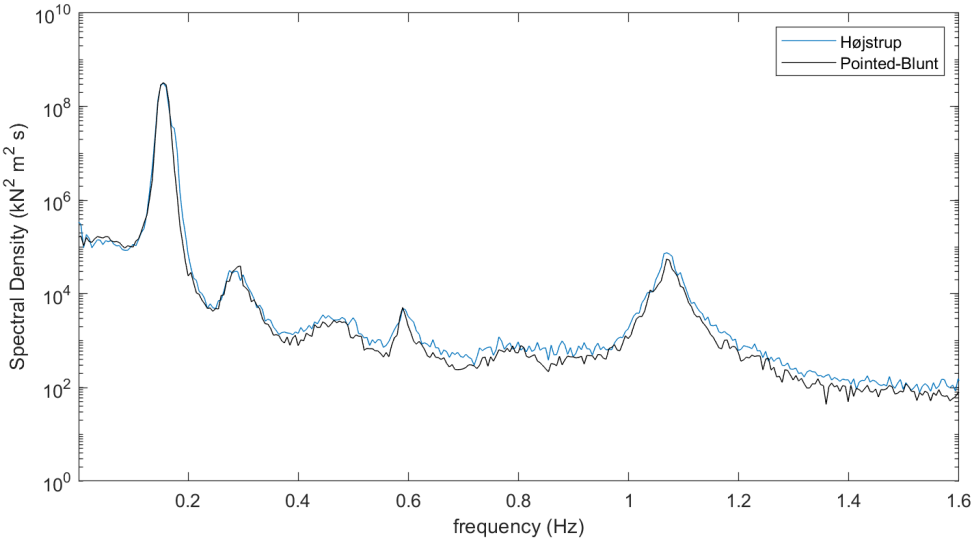

Figure 4.32: Blade Root Edge-Wise Moment for Højstrup and Pointed-Blunt, 8m/s, Unstable

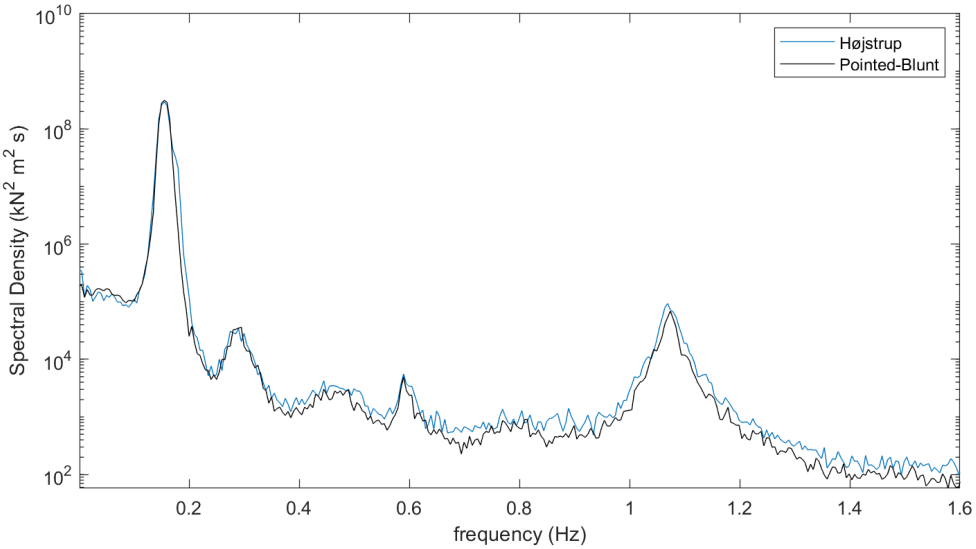

Figure 4.33: Blade Root Edge-Wise Moment for Højstrup and Pointed-Blunt, 8m/s, Very Unstable

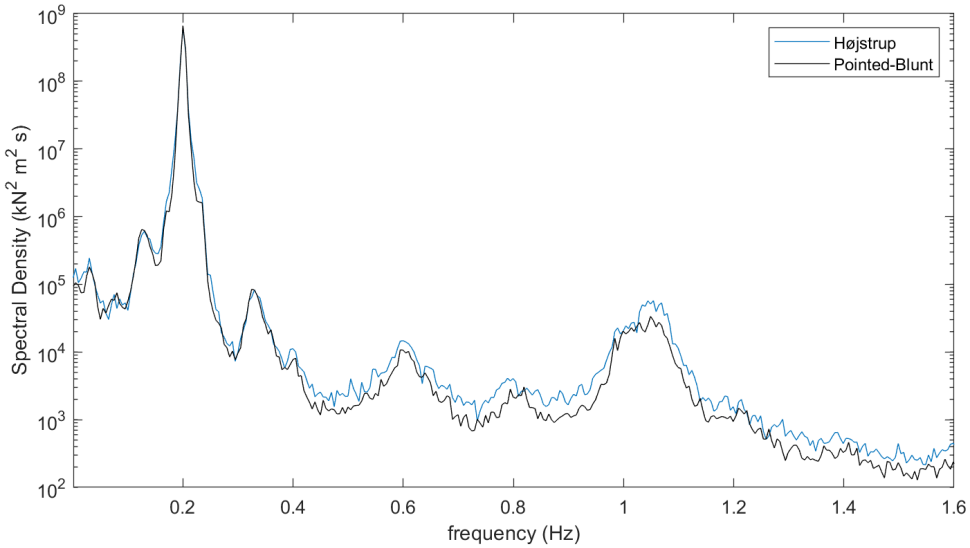

Figure 4.34: Blade Root Edge-Wise Moment for Højstrup and Pointed-Blunt, 11m/s, Unstable

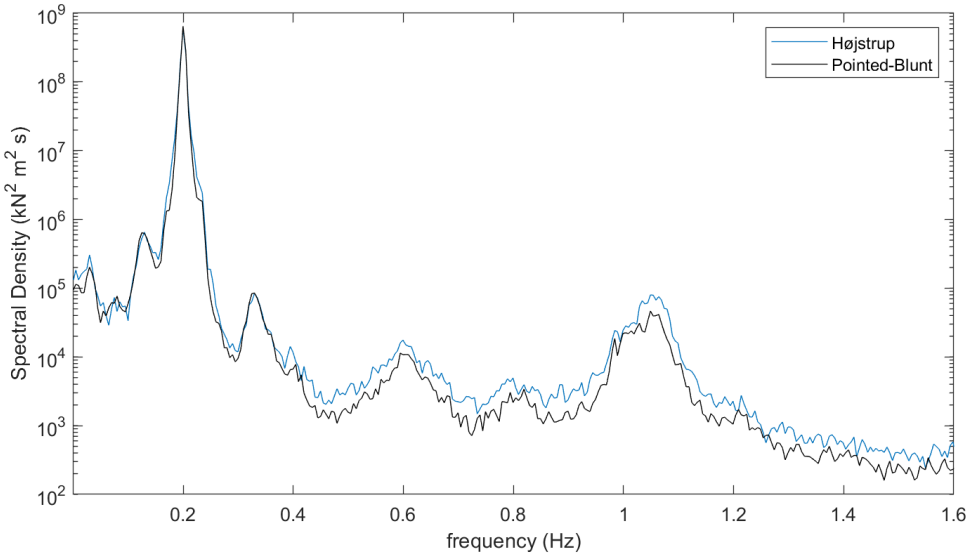

Figure 4.35: Blade Root Edge-Wise Moment for Højstrup and Pointed-Blunt, 11m/s, Very Unstable

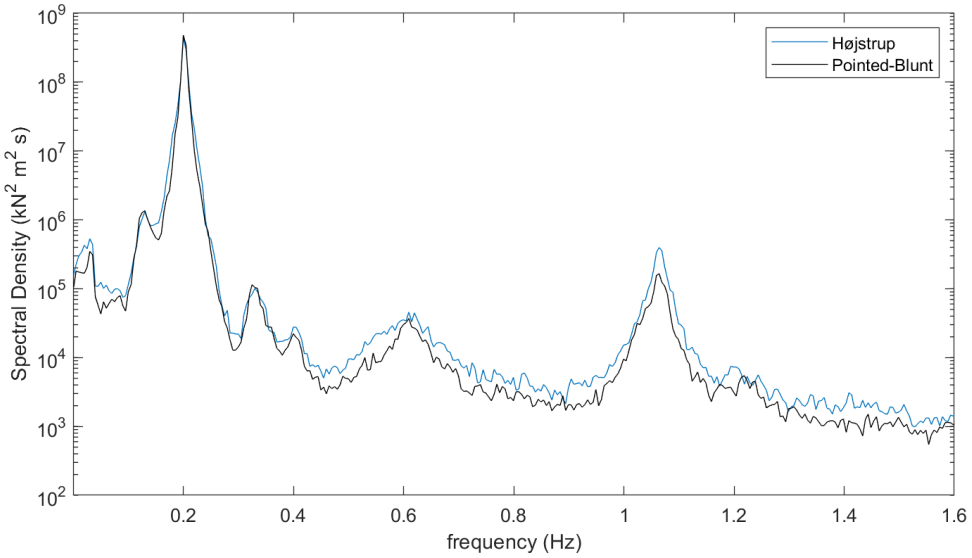

Figure 4.36: Blade Root Edge-Wise Moment for Højstrup and Pointed-Blunt, 15m/s, Unstable

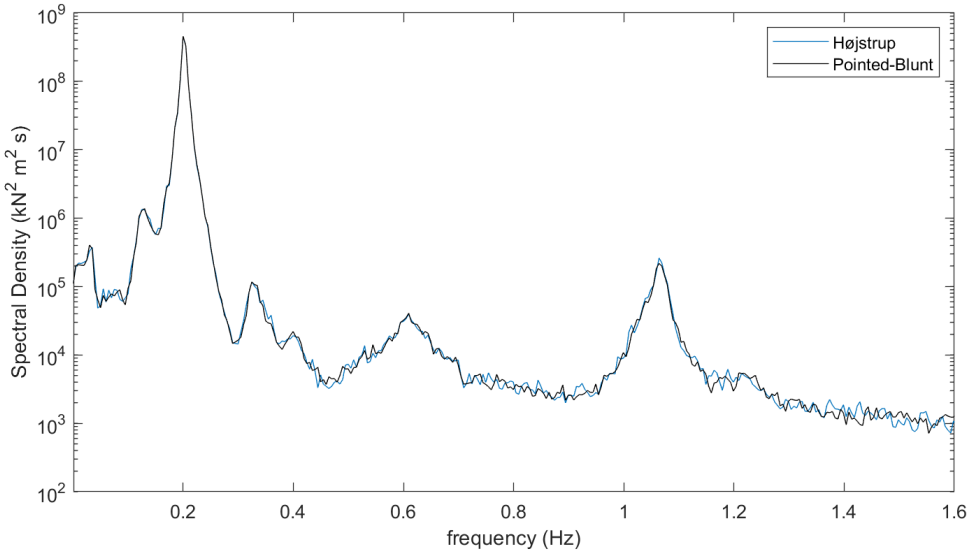

Figure 4.37: Blade Root Edge-Wise Moment for Højstrup and Pointed-Blunt, 15m/s, Very Unstable

4.3 Damage Equivalent Loads

The damage equivalent loads on the wind turbine were calculated for the tower base fore-aft moment, tower base side-side moment, tower top torsion, blade root flap-wise moment, and blade root edge-wise moment. The DEL is evaluated using the

1Hz duration, which is common practice for wind turbine DEL evaluation (Burton, Sharpe, Jenkins, & Bossanyi, 2001). For 1Hz DELs, the equivalent number of cycles (n_eq) represents the time that the wind turbine is in operation. For this study, n_eq is set to 3600 to represent the simulation duration of one hour. Tables 4.2 to 4.6 show the averaged 1Hz DEL values for the different tower and blade motions.

The magnitude of the damage equivalent loads is highest in the tower base fore-aft moment, with Højstrup's Model producing higher DEL values as the atmospheric stability becomes more unstable. All the DEL values increase somewhat linearly as the stability is more unstable except for the tower base side-side moment and blade root edge-wise.

Table 4.2: Tower Base Fore-Aft Moment 1Hz DEL Values (kNm)

	Højstrup			**Pointed-Blunt**		
	Neutral	**Unstable**	**Very Unstable**	**Neutral**	**Unstable**	**Very Unstable**
8m/s	10287.45	10562.92	10782.88	10348.93	10277.21	10368.52
11m/s	11240.81	11572.77	11734.67	11249.41	11241.92	11306.34
15m/s	11676.95	12090.69	12326.33	11819.94	11833.76	11992.10

Table 4.3: Tower Base Side-Side Moment DEL Values (kNm)

	Højstrup			**Pointed**-Blunt		
	Neutral	**Unstable**	**Very Unstable**	**Neutral**	**Unstable**	**Very Unstable**
8m/s	1484.56	1690.17	1748.94	1546.30	1578.27	1611.84
11m/s	996.71	1169.87	1274.45	1001.78	991.83	1025.17
15m/s	1281.20	1706.49	1988.73	1355.92	1396.19	1554.09

Table 4.4: Tower Top Torsion DEL Values (kNm)

	Højstrup			**Pointed**-Blunt		
	Neutral	**Unstable**	**Very Unstable**	**Neutral**	**Unstable**	**Very Unstable**
8m/s	300.66	392.39	426.56	312.55	316.52	334.74
11m/s	517.17	668.91	753.59	514.10	518.94	567.55
15m/s	724.28	956.75	1080.31	712.29	724.04	800.96

Table 4.5: Blade Root Flap-Wise Moment DEL Values (kNm)

	Højstrup			**Pointed-Blunt**		
	Neutral	**Unstable**	**Very Unstable**	**Neutral**	**Unstable**	**Very Unstable**
8m/s	2111.53	2226.06	2279.92	2171.18	2196.38	2220.06
11m/s	3064.69	3183.25	3261.81	2950.75	2979.51	3008.87
15m/s	3866.20	4085.16	4102.94	3830.23	3814.45	3839.17

Table 4.6: Blade Root Edge-Wise Moment DEL Values (kNm)

	Højstrup			**Pointed-Blunt**		
	Neutral	**Unstable**	**Very Unstable**	**Neutral**	**Unstable**	**Very Unstable**
8m/s	2996.44	3008.68	3062.26	2996.71	2998.36	3001.30
11m/s	3119.67	3138.24	3150.53	3119.02	3120.10	3126.01
15m/s	3100.15	3139.98	3167.40	3098.48	3098.22	3114.42

4.3.1 Normalized Damage Equivalent Loads

For easier comparison between the models, the DELs have been normalized. Figures 4.38 and 4.39 show the neutral, unstable, and very unstable tower base fore-aft moment for Højstrup's Model and the Pointed-Blunt Model, respectively. With Højstrup's Model, there is much more separation of the DEL values as the atmospheric stability becomes more unstable. In the Pointed-Blunt Model, the DEL values are very similar at all the atmospheric stability conditions, with some separation of the very unstable case at higher wind speeds. Just as with the spectral densities, this separation remains consistent with each model though all the tower and blade motions. The rest of the graphs comparing atmospheric stability will be placed in Appendix A.3.2 and A.3.3 for Højstrup's Model and the Pointed-Blunt Model, respectively. Additionally, only the unstable and very unstable atmospheric conditions will used for comparison between models here, the neutral comparisons can be found in Appendix A.3.1

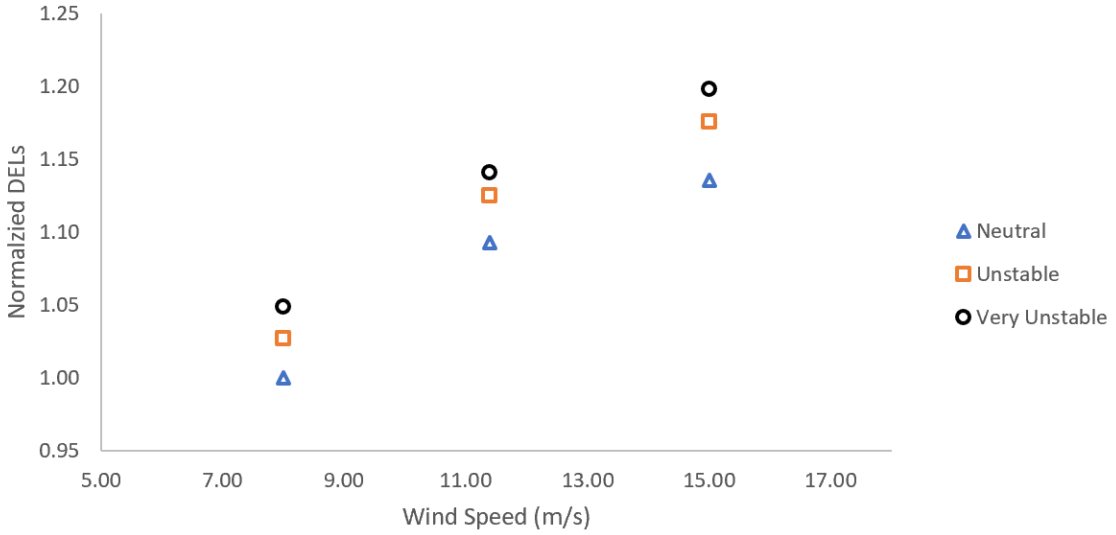

Figure 4.38: DEL for the Tower Base Fore-Aft Moment, Højstrup's Unstable Spectra Model

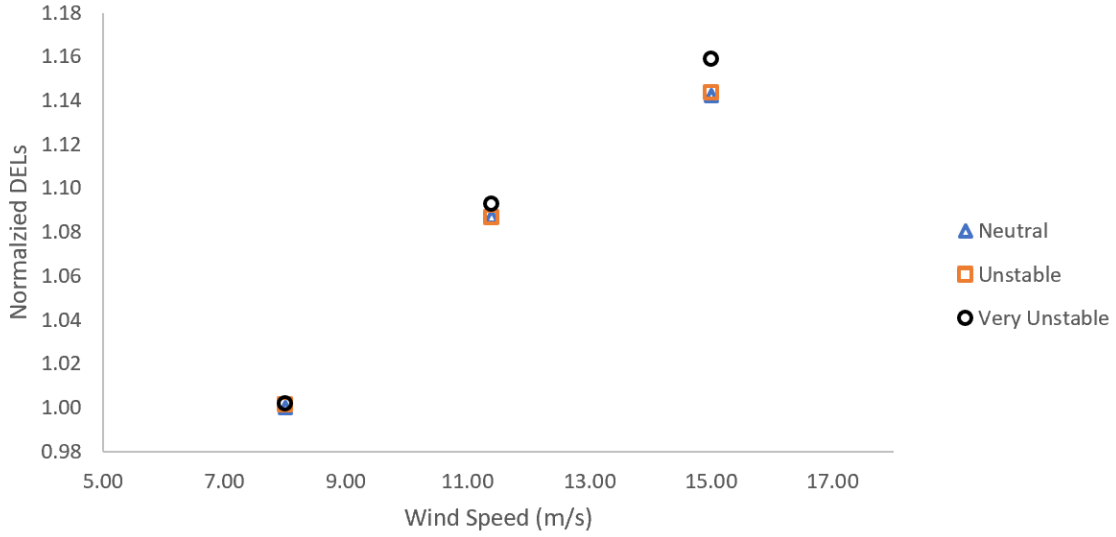

Figure 4.39: DEL for the Tower Base Fore-Aft Moment, Pointed-Blunt Model

As seen with the raw data, Højstrup's Model produces higher DEL values for both unstable and very unstable conditions and at all three wind speeds for the tower base fore-aft moment (Figures 4.40 and 4.41. The tower base fore-aft moment is considerably sensitive to changes in wind speed and also changes in the atmospheric stability.

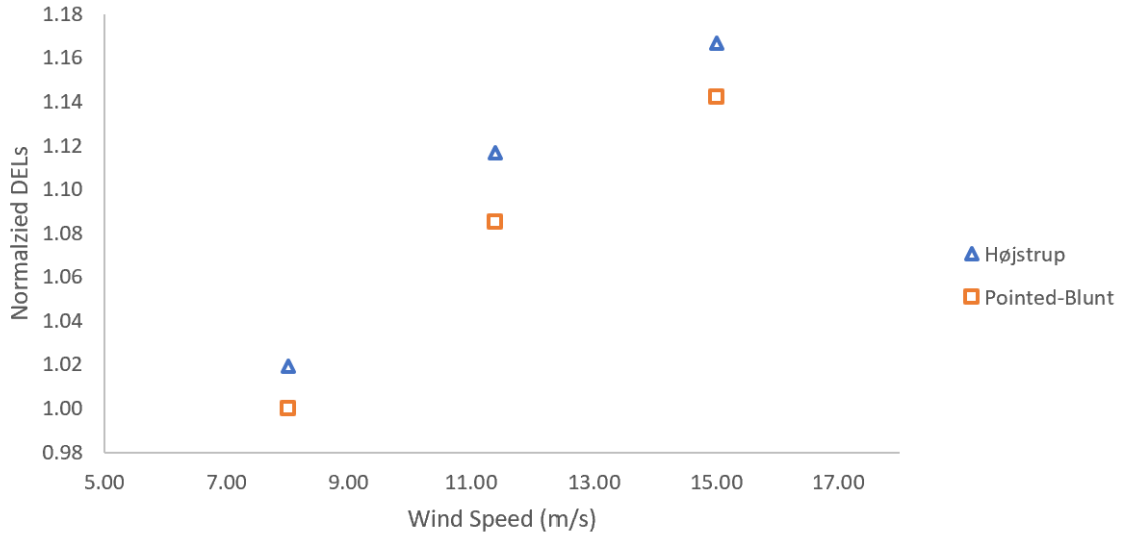

Figure 4.40: DEL for the Tower Base Fore-Aft Moment, Unstable conditions

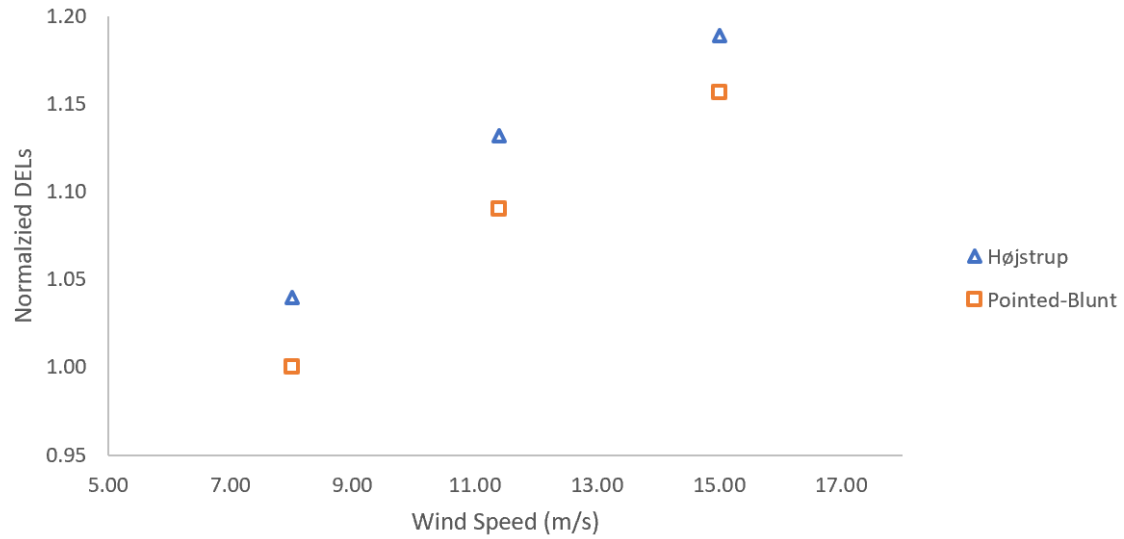

Figure 4.41: DEL for the Tower Base Fore-Aft Moment, Very Unstable conditions

The tower base side-side moment (Figures 4.42 and 4.43) is the standout in terms of its relationship to atmospheric stability and wind speed. It does not have the linear relationship that the tower base fore-aft moment did. Additionally the DEL values between the models are less varied. From the spectral density plots it can be seen that the tower base side-side moment has much less excitation due to the wave spectral peak, and the tower fore-aft moment is the dominant tower moment.

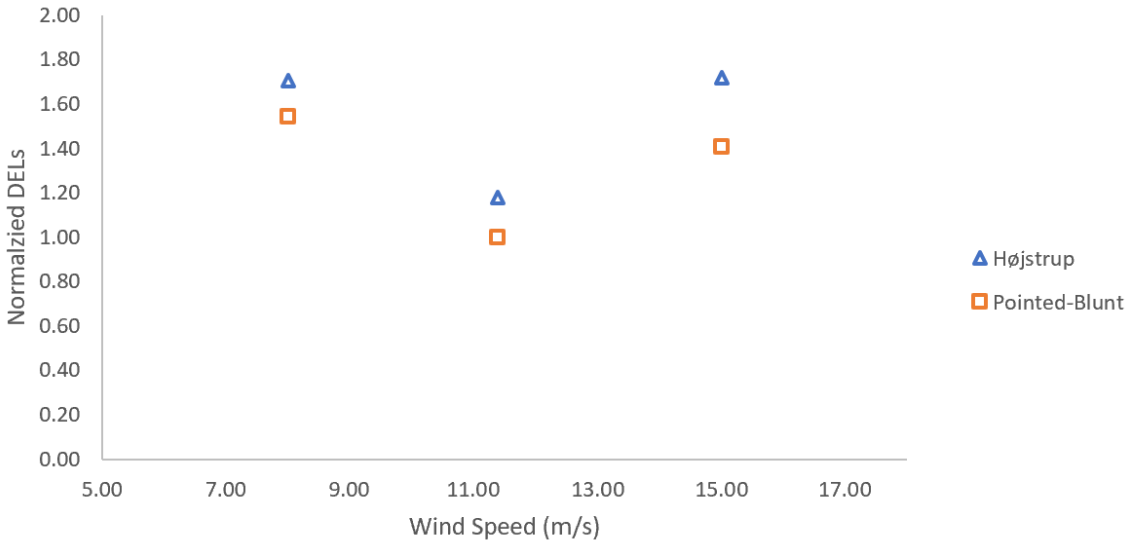

Figure 4.42: DEL for the Tower Base Side-Side Moment, Unstable conditions

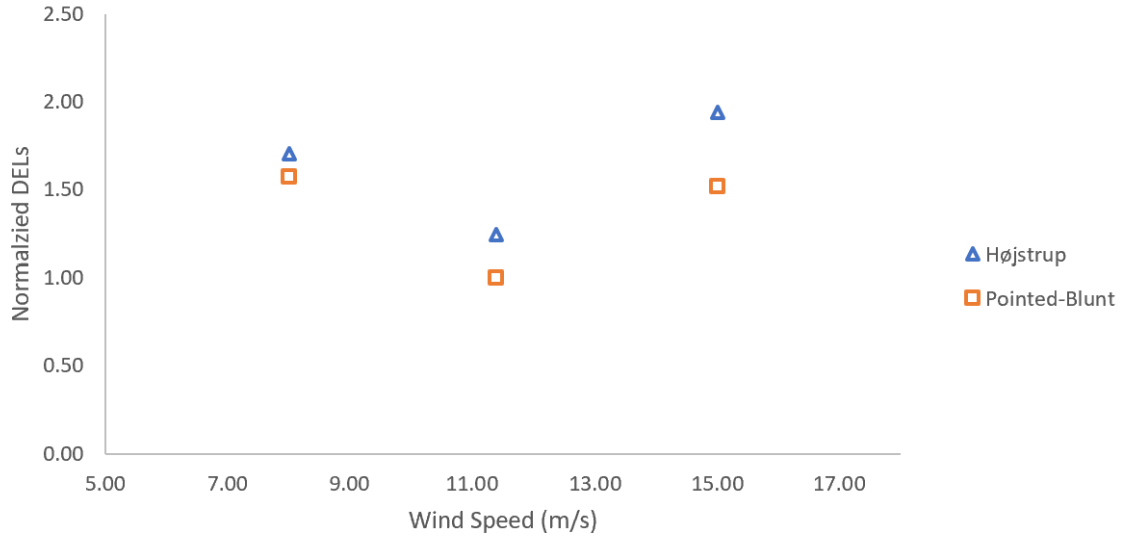

Figure 4.43: DEL for the Tower Base Side-Side Moment, Very Unstable conditions

Figures 4.44 and 4.45 have the normalized DEL values for the tower top torsion. The tower top torsion is the most effected by increasing wind speeds and more unstable wind conditions. With both models, there is a large variation between below rated and above rated wind speeds.

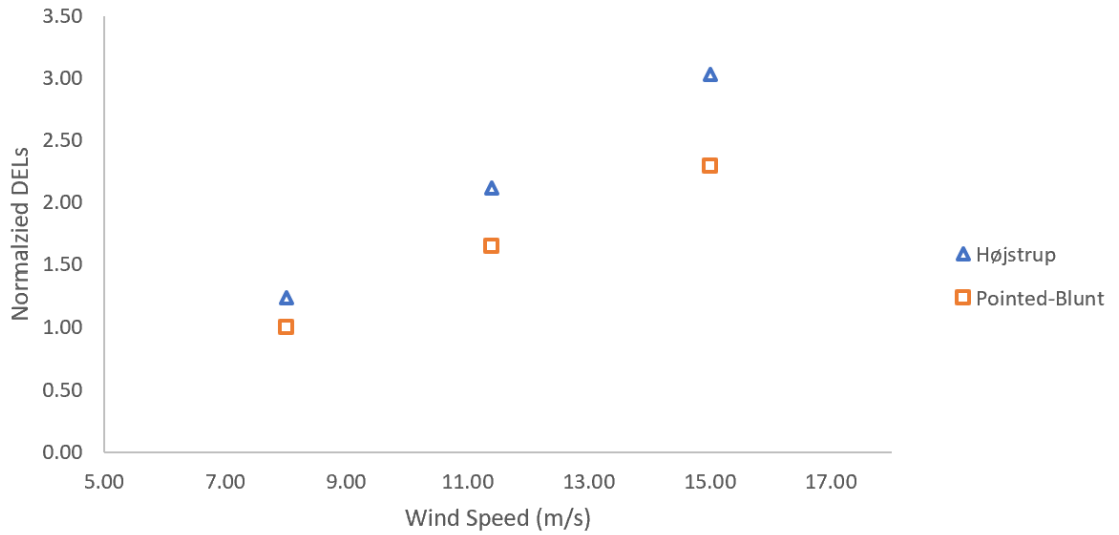

Figure 4.44: DEL for the Tower Top Torsion, Unstable conditions

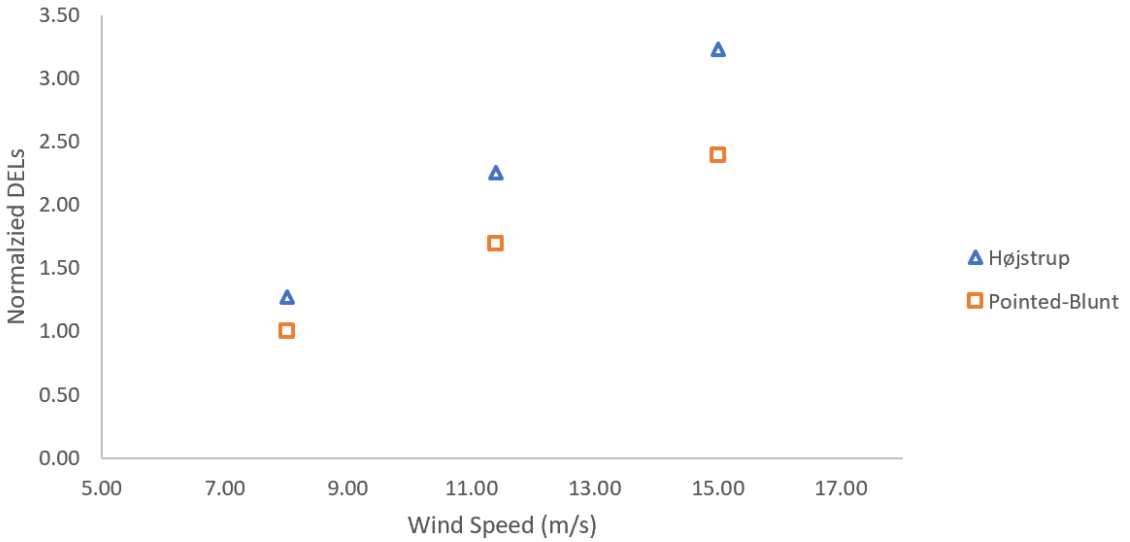

Figure 4.45: DEL for the Tower Top Torsion, Very Unstable conditions

The blade root flap-wise moment was quite similar between the two models (Figures 4.46 and 4.47). The main influence on the DEL values in this case is the changing wind speed.

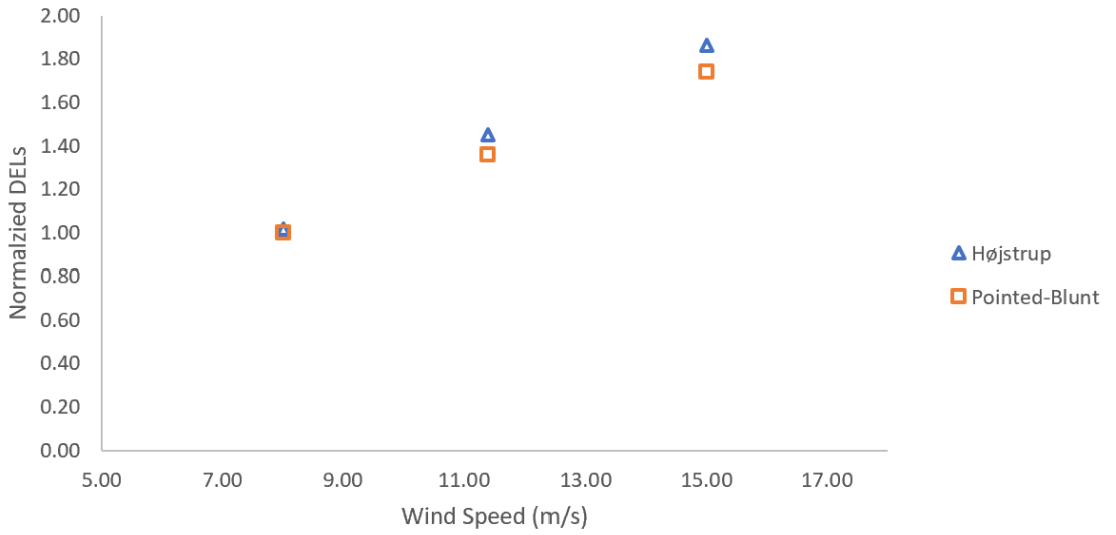

Figure 4.46: DEL for the Blade Root Flap-Wise Moment, Unstable conditions

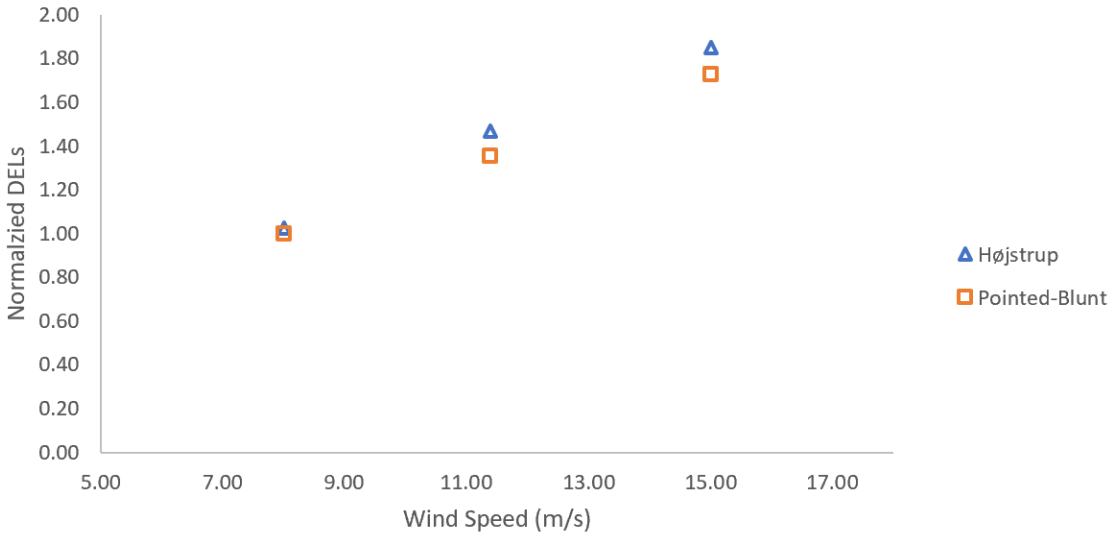

Figure 4.47: DEL for the Blade Root Flap-Wise Moment, Very Unstable conditions

Figures 4.48 and 4.49 show that for the blade root edge-wise moment, there is a big difference between below rated and rated wind speed. The increase in the DEL values as the atmospheric stability becomes more unstable is minor when compared to the increase with increasing wind speed.

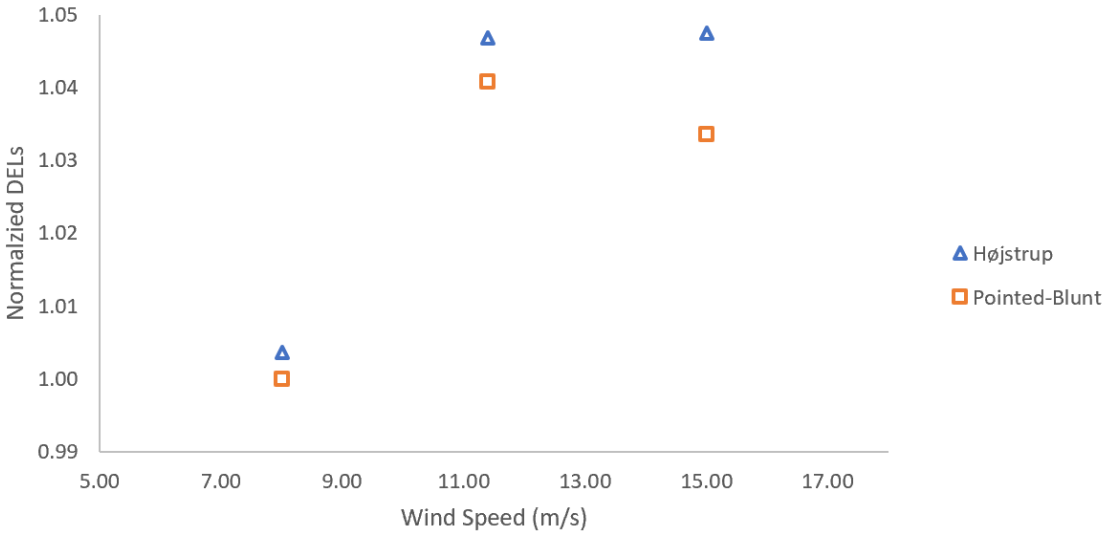

Figure 4.48: DEL for the Blade Root Edge-Wise Moment, Unstable conditions

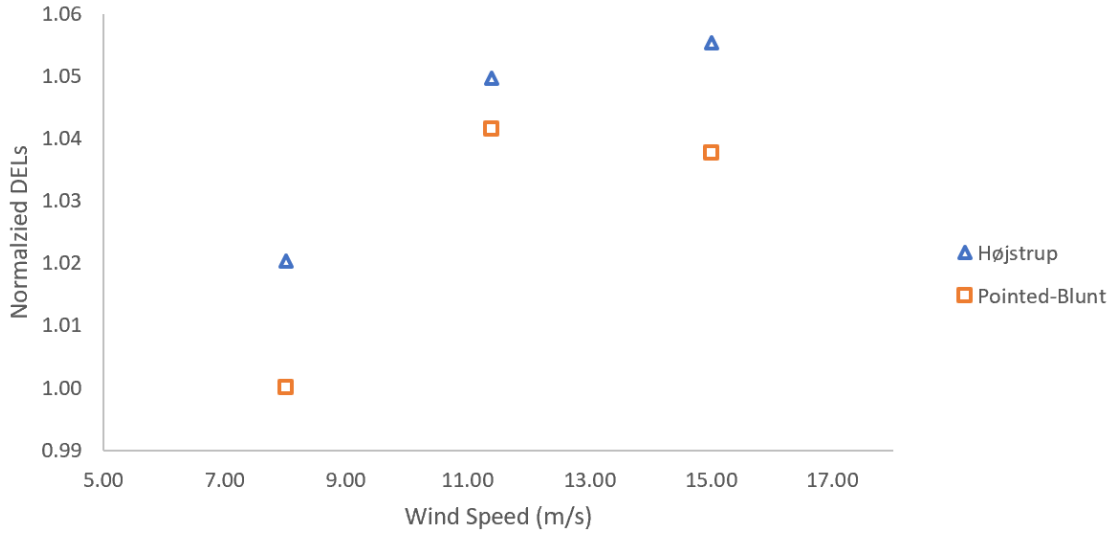

Figure 4.49: DEL for the Blade Root Edge-Wise Moment, Very Unstable conditions

5 Conclusion

This study investigated the influence of unstable wind spectra on the motions and loads of a semi-submersible floating offshore wind turbine. Two models, Højstrup's Unstable Spectra Model, and the Pointed-Blunt Model were used to simulate the wind spectra. The OC4-DeepCwind semi-submerisble wind turbine was used as a model. The spectral densities and damage equivalent loads were found for the tower base fore-aft moment, tower base side-side moment, tower top torsion moment, blade root flap-wise moment, and blade root edge-wise moment. The turbulence intensities were found for both models as well. While the neutral TI values were comparable, as the atmospheric stability becomes more unstable, Højstrup's Unstable Spectra Model was more sensitive to the shift towards very unstable conditions and had higher turbulence intensity values. This results in the larger fatigue loads generated by Højstrup's Model.

The tower base fore-aft moment was found to have the highest damage equivalent loads and was influenced by wind speed and atmospheric stability for both models. The tower base side-side moment has a smaller energy profile than the tower base fore-aft moment in both models. The tower top torsion moment damage equivalent loads experienced the most change with increasing wind speed. It was much more influenced by wind speed than the change in atmospheric stability. The blade root flap-wise moment damage equivalent loads were the most similar when comparing the two models. Finally, the blade root edge-wise moment DEL values seemed to be most effected by the change from neutral to unstable conditions.

Overall Højstrup's Unstable Spectra Model provided higher energy spectra and damage equivalent loads in both unstable and very unstable atmospheric conditions. The Pointed-Blunt Model generates less turbulence intensity and therefore generates smaller DEL values when compared to Højstrup's Unstable Spectra Model for unstable and very unstable atmosphere conditions. Additionally, it was seen that Højstrup's Unstable Spectra Model had more variation in the

results when changing the atmospheric stability. The difference in the neutral, unstable, and very unstable conditions was much less pronounced with the Pointed-Blunt Model.

5.1 Suggestions for Future work

The following suggestions could be used to further the work of this project:

- Changing of the inversion height z_i to further examine the response of Højstrup's Unstable Spectra Model and the Pointed-Blunt Model
- Implementing an eigen frequency analysis for OC4-DeepCwind to determine the associated transfer functions
- Further study into the effect of coherence on the wind profile, particularly utilizing the Modified Davenport Wind Coherence model
- Branching out to larger wind turbines to better simulate what offshore floating wind turbines experience
- To validate the generated results in offshore conditions, further measurements are needed to reduce the uncertainty and estimations in offshore wind turbine design

Bibliography

Abdalla, A., El-Osta, W., & Dekam, E. (2017). The influence of the atmospheric stability conditions on the available wind energy for three libyan coastal cities. *Solar Energy and Sustainable Development*, *6*(2), 16–29.

Blasques, J. P. A. A., & Natarajan, A. (2013). Mean load effects on the fatigue life of offshore wind turbine monopile foundations. *Computational Methods in marine Engineering*, 1–12.

Burton, T., Sharpe, D., Jenkins, N., & Bossanyi, E. (2001). *Wind energy handbook*. Chichester, England: J. Wiley and Sons.

Cheynet, E., Jakobsen, J. B., & Reuder, J. (2018). Velocity spectra and coherence estimates in the marine atmospheric boundary layer. *Boundary-Layer Meteorology*, *169*, 429–460.

Cheynet, E., Jakobsen, J. B., & Snæbjörnsson, J. (2015). Buffeting response of a bridge at the inlet of a fjord. *14th International Conference on Wind Engineering*, 1–13.

Chougule, A., Mann, J., mark Kelly, & Larsen, G. C. (2017). Modeling atmospheric turbulence via rapid distortion theory: Spectral tensor of velocity and buoyancy. *Journal of the Atmospheric Sciences*, *74*, 949–974.

Crasto, G. (2007). *Numerical simulations of the atmospheric boundary layer* (Master's thesis, Università degil Studi di Cagllari).

Davenport, A. G. (1961). The spectrum of horizontal gustiness near the ground in high winds. *Quarterly Journal of the Royal Meteorological Society*, *88*(376), 194–211.

Dnv-rp-c205: Environmental conditions and environmental loads. (2010). Det Norske Veritas AS. Oslo: Veritas Offshore Technology.

Eliassen, L., & Obhrai, C. (2016). Coherence of turbulent wind under neutral wind conditions at fino1. *Energy Procedia*, *94*, 388–398.

GopiReddy, L., Tolbert, L. M., & Ozpineci, B. (2012). Lifetime prediction of igbt in a statcom using modified-graphical rainflow counting algorithm. *IECON 2012-38th Annual Conference on IEEE Industrial Electronics Society*, 3425–3430.

Gryning, S.-E., Batchvarova, E., Brümmer, B., Jørgensen, H., & Larsen, S. (2007). On the extension of the wind profile over homogeneous terrain beyond the surface boundary later. *Boundary-Layer Meteorology*, *124*, 251–268.

Højstrup, J. (1981). A simple model for the adjustment of velocity spectra in unstable conditions downstream of an abrupt change in roughness and heat flux. *Boundary-Layer Meteorology*, *21*(3), 341–356.

Højstrup, J. (1982). Velocity spectra in the unstable planetary boundary layer. *Journal of the Atmospheric Sciences*, *39*(10), 2239–2248.

Højstrup, J. (1999). Spectral coherence in wind turbine wakes. *Journal of Wind Engineering*, *80*, 137–146.

Kaimal, J., Wyngaard, J., Izumi, Y., & Coté, O. R. (1972). Spectral characteristics of surface-layer turbulence. *Quarterly Journal of the Royal Meteorological Society*, *98*(417), 563–589.

Kaldellis, J., & Kapsali, M. (2013). Shifting towards offshore wind energy-recent activity and future development. *Energy Policy*, *53*, 136–148.

Knight, J.-A. (2019). *The influence of an unstable turbulent wind spectrum on the loads and motions on a floating offshore wind turbine* (Master's thesis, Universitet i Stavanger).

Kristensen, L., & Jensen, N. (1979). Lateral coherence in isotropic turbulence and in the natural wind. *Boundary layer Meteorology*, *17*, 353–373.

Krogsæter, O., & Reuder, J. (2015). Validation of boundary layer parameterization schemes in the weather research and forecasting (wrf) model under teh aspect of offshore wind energy applications-part ii: Boundary layer height and atmospheric stability. *Wind Energy*, *18*, 1291–1302.

Mann, J. (1998). Wind field simulation. *Probabilistic Engineering Mechanics*, *13*(4), 269–282.

Monin, A., & Obukhov, A. (1954). Basic laws of turbulent mixing in the surface layer of the atmosphere. *Tr. Akad. Nauk SSSR Geophiz. Inst. 24*(151), 163–187.

Oke, T. (1978). *Boundary layer climates*. London: Methuen.

Panofsky, H., Tennekes, H., Lenschow, D., & Wyngaard, J. (1976). The characteristics of turbulent velocity components in the surface layer under convective conditions. *Boundary-Layer Meteorology*, *11*, 355–361.

Panofsky, H. A., & Mizuno, T. (1975). Horizontal coherence and pasquill's beta. *Boundary-Layer Meteorology*, *9*(3), 247–256.

Peng, Z., Huang, H.-Z., Zhou, J., & Li, Y.-F. (2018). A new cumulative fatigue damage rule based on dynamic residual s-n curve and material memory concept. *Metals*, *8*, 1–17.

Pielke, R., & Panofsky, H. (1970). Turbulence characteristics along several towers. *Boundary-Layer Meteorology*, *1*, 115–130.

Putri, R. (2016). *A study of the coherences of turbulent wind on a floating offshore wind turbine* (Master's thesis, Universitet i Stavanger).

Ramírez, L., Fraile, D., & Brindley, G. (2020). *Offshore wind in europe - key trends and statistics 2019*. WindEurope.

Robertson, A., Jonkman, J., Masciola, M., Song, H., Goupee, A., Coulling, A., & Luan, C. (2003). *Dowec 6 mw pre-design: Aero-elastic modeling of the dowec 6 mw pre-design in phatas*. DOWEC Dutch Offshore Wind Energy Converter 1997-2003 Public Reports.

Robertson, A., Jonkman, J., Masciola, M., Song, H., Goupee, A., Coulling, A., & Luan, C. (2014). *Definition of the semisubmersible floating system for phase ii of oc4*. National Renewable Energy Laboratory. Golden, CO.

Robertson, A., Jonkman, J., Vorpahl, F., Popko, W., Qvist, J., Frøyd, L., ... Guérinel, M. (2015). Offshore code comparison collaboration continuation within iea wind task 30: Phase ii results regarding a floating semisubmersible wind system. *nternational Conference on Offshore Mechanics and Arctic Engineering*, *45547*, 1–15.

Ropelewski, C., Tennekes, H., & Panofsky, H. (1973). Horizontal coherence of wind fluctuations. *Boundary-Layer Meteorology*, *5*, 353–363.

Royal Academy of Engineering. (2010). Wind turbine power calculations. RWE Npower Renewables, Mechanical and Electrical Engineering Power Industry.

Saranyasoontorn, K., Manuel, L., & Veers, P. S. (2004). A comparison of standard coherence models for inflow turbulence with estimates from field measurements. *Journal of Solar Energy Engineering*, *126*, 1069–1082.

Sathe, A., Mannn, J., Barlas, T., Bierbooms, W., & van Bussel, G. (2013). Influence of atmospheric stability on wind turbine loads. *Wind Energy*, *16*, 1013–1032.

Schroeder, M. J., & Buck, C. C. (1970). *Fire weather: A guide for application of meteorological information to forest fire control operations*. Agricultural Handbook 360. Washington, D.C.: U.S. Department of Agriculture.

Sohoni, B., Gupta, S., & Nema, R. (2016). A critical review on wind turbine power curve modelling techniques and their applications in wind based energy systems. *Journal of Energy*, *2016*.

Solari, G. (1987). Turbulence modeling for gust loading. *Journal of Structural Engineering*, *113*(7), 1550–1569.

Solari, G., & Piccardo, G. (2001). Probabilistic 3-d turbulence modeling for gust buffeting of structures. *Probabilistic Engineering Mechanics*, *16*(1), 73–86.

TC88-MT, I. (2005). *Iec 61400-3: Wind turbines-part1: Design requirements*. International Electrotechnical Commission. Geneva, Switzerland.

The Editors of Encyclopaedia Britannica. (2016). Lapse rate. Retrieved from https://www.britannica.com/science/lapse-rate.

Xu, Y.-L. (2013). *Wind effects on cable-supported bridges*. Singapore: John Wiley & Sons Singapore Pte. Ltd.

A Appendix

A.1 U-Component Spectra

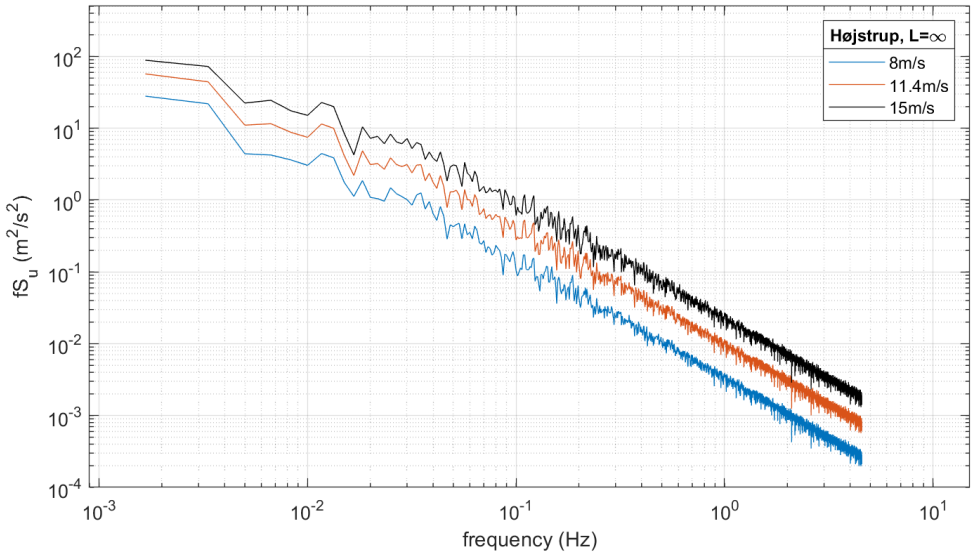

Figure A.1: Spectral Density for u-component, Højstrup's Model, Neutral Conditions

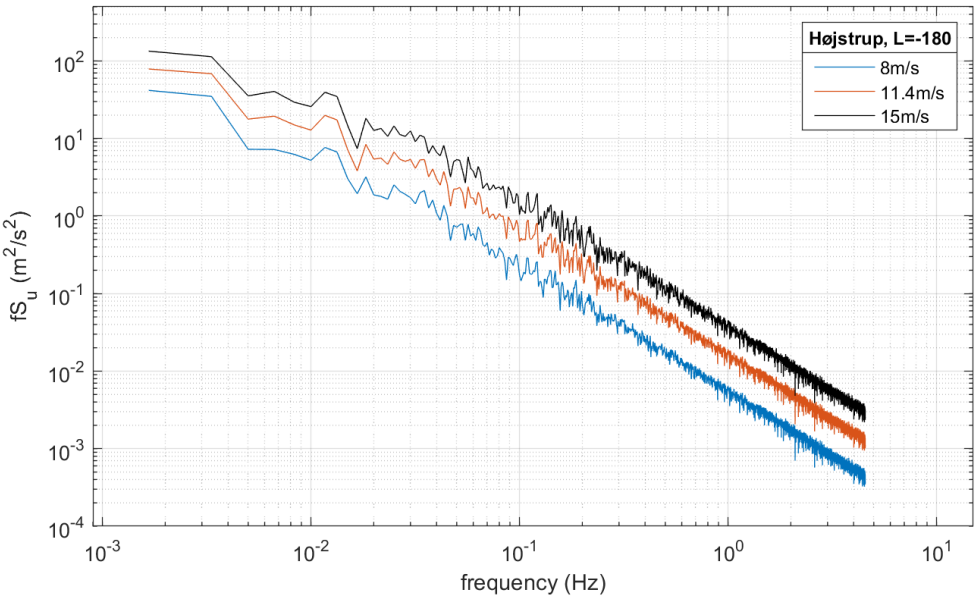

Figure A.2: Spectral Density for u-component, Højstrup's Model, Unstable Conditions

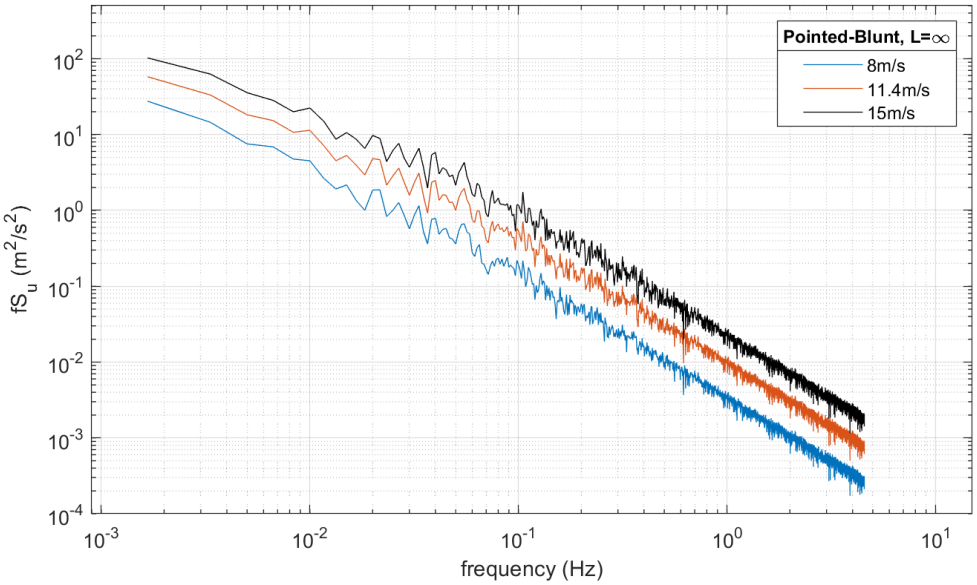

Figure A.3: Spectral Density for u-component,Pointed-Blunt Model, Neutral Conditions

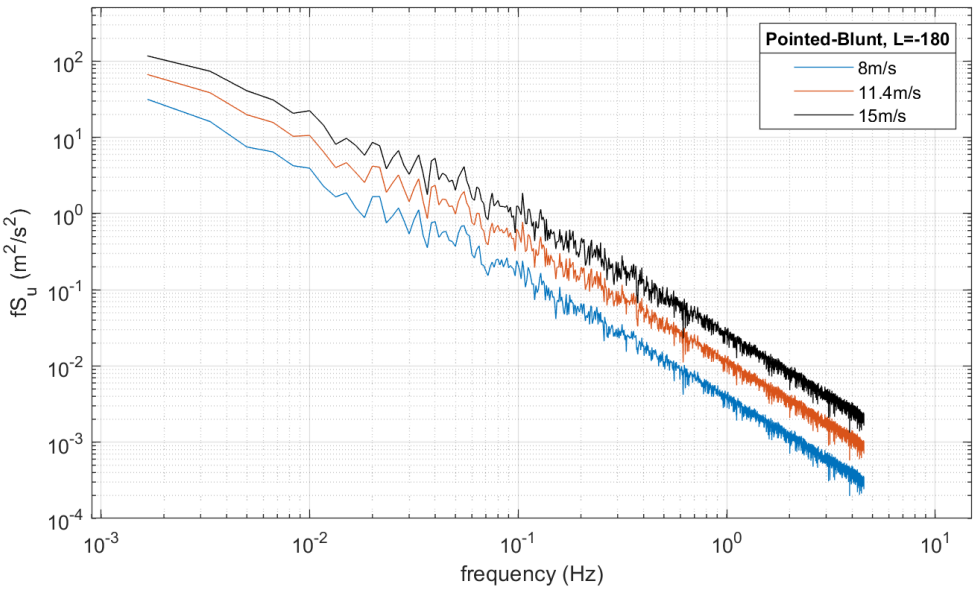

Figure A.4: Spectral Density for u-component, Pointed-Blunt Model, Unstable Conditions

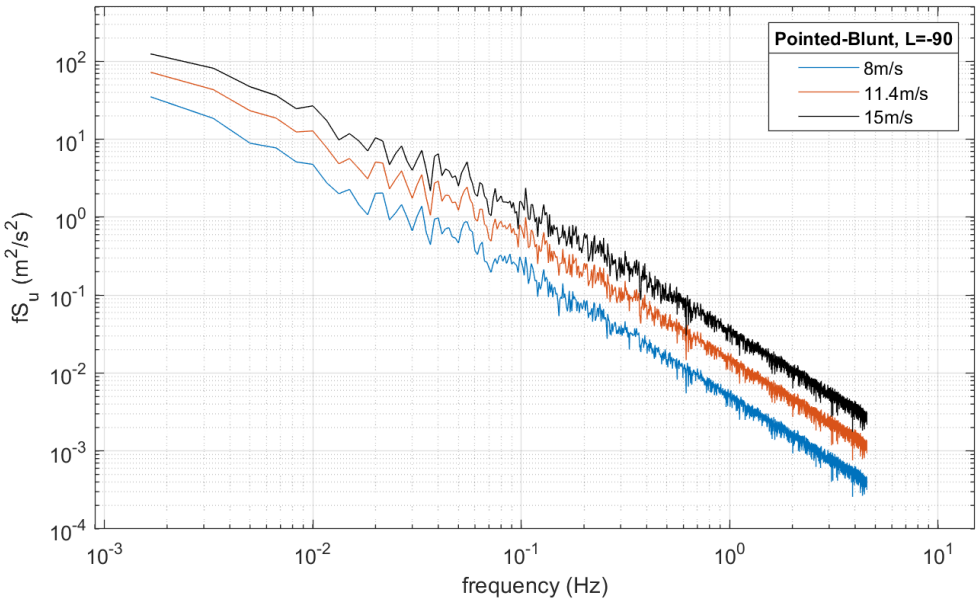

Figure A.5: Spectral Density for u-component, Pointed-Blunt Model, Very Unstable Conditions

A.2 Spectral Density Results

A.2.1 Neutral Results

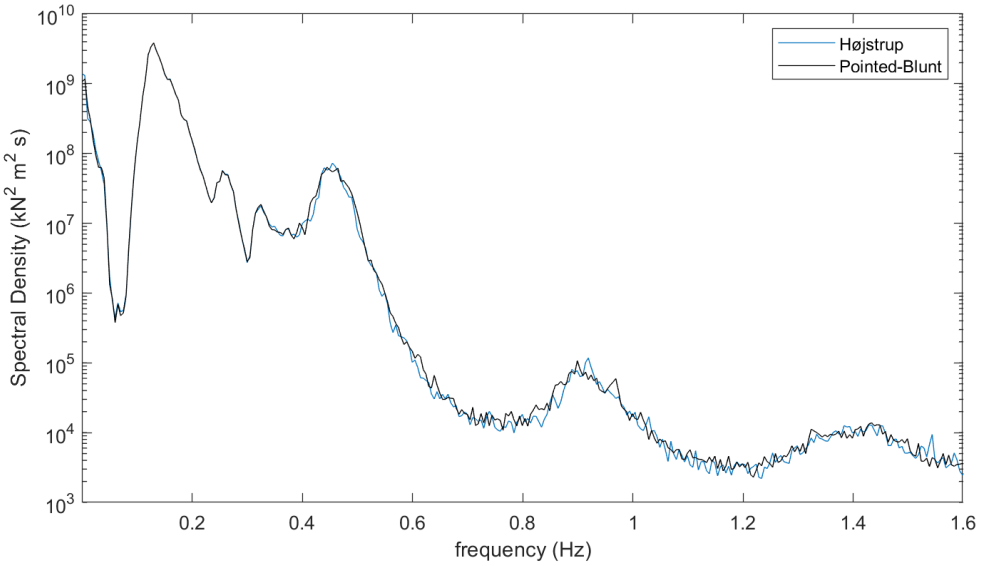

Figure A.6: Spectral Density for Tower Base Fore-Aft Moment, 8m/s, Neutral Conditions

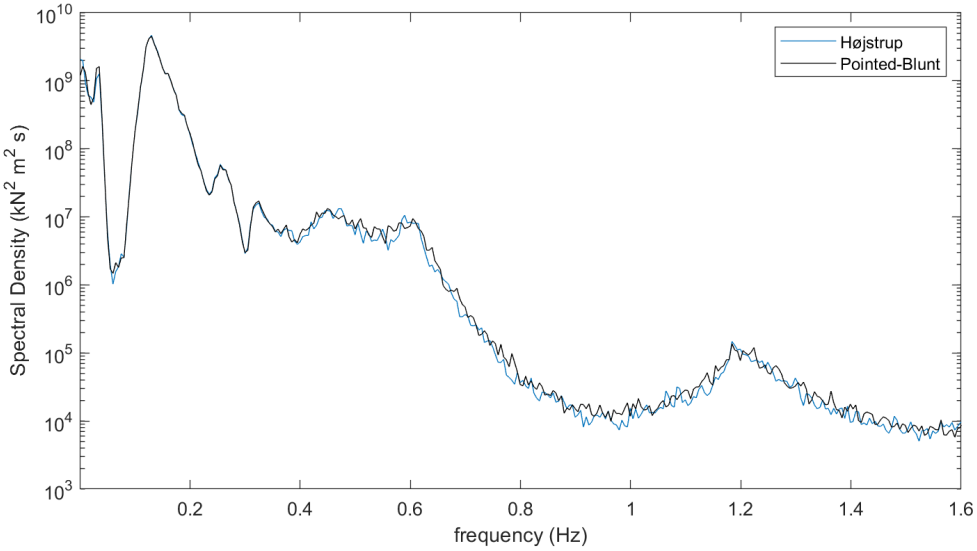

Figure A.7: Spectral Density for Tower Base Fore-Aft Moment, 11.4m/s, Neutral Conditions

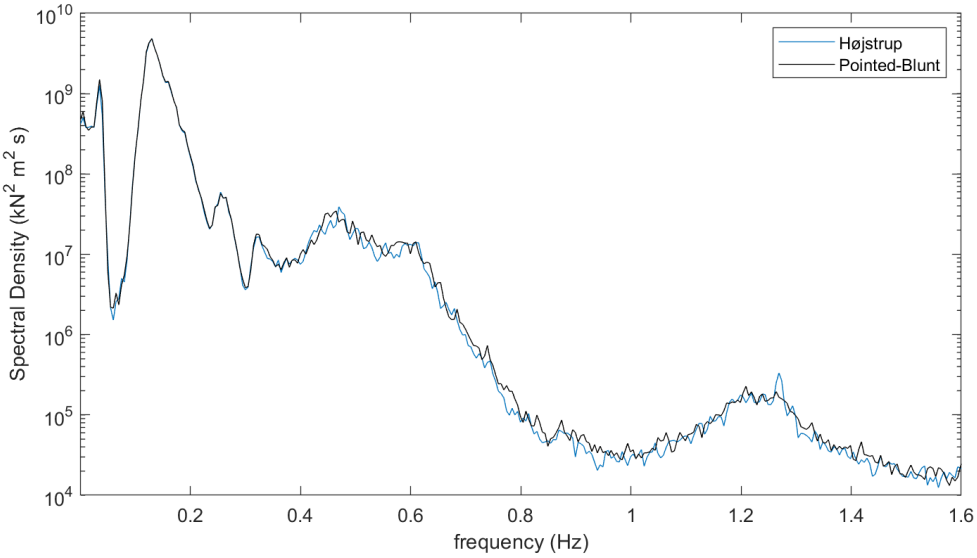

Figure A.8: Spectral Density for Tower Base Fore-Aft Moment, 15m/s, Neutral Conditions

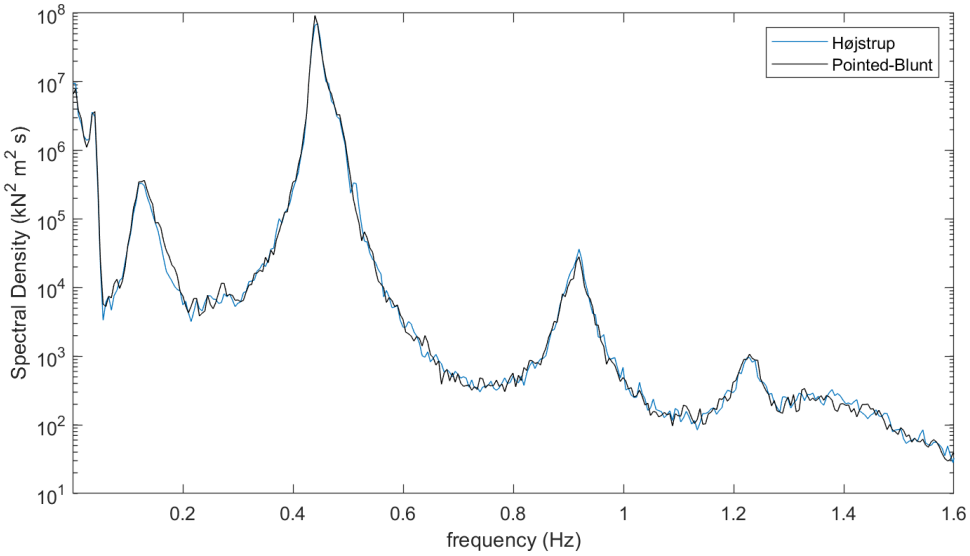

Figure A.9: Spectral Density for Tower Base Side-Side Moment, 8m/s, Neutral Conditions

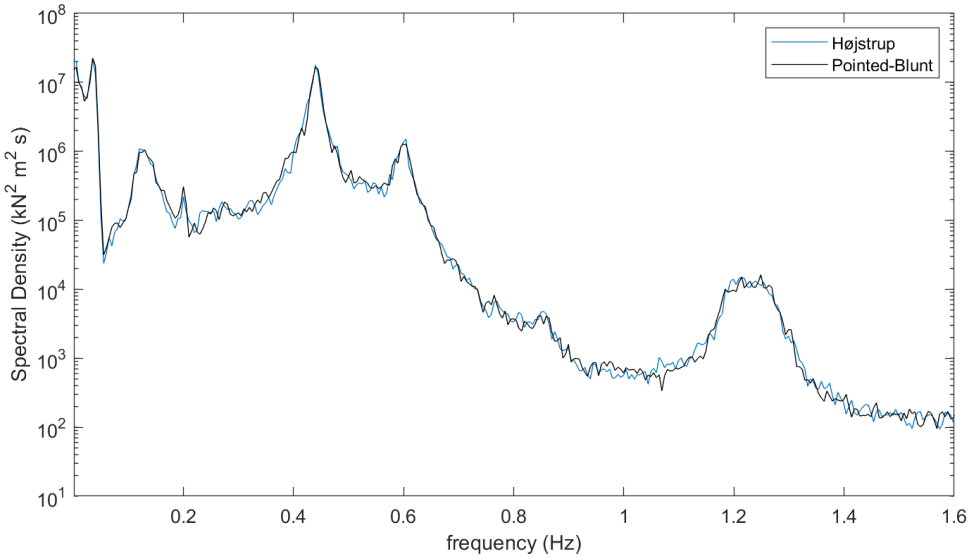

Figure A.10: Spectral Density for Tower Base Side-Side Moment, 11.4m/s, Neutral Conditions

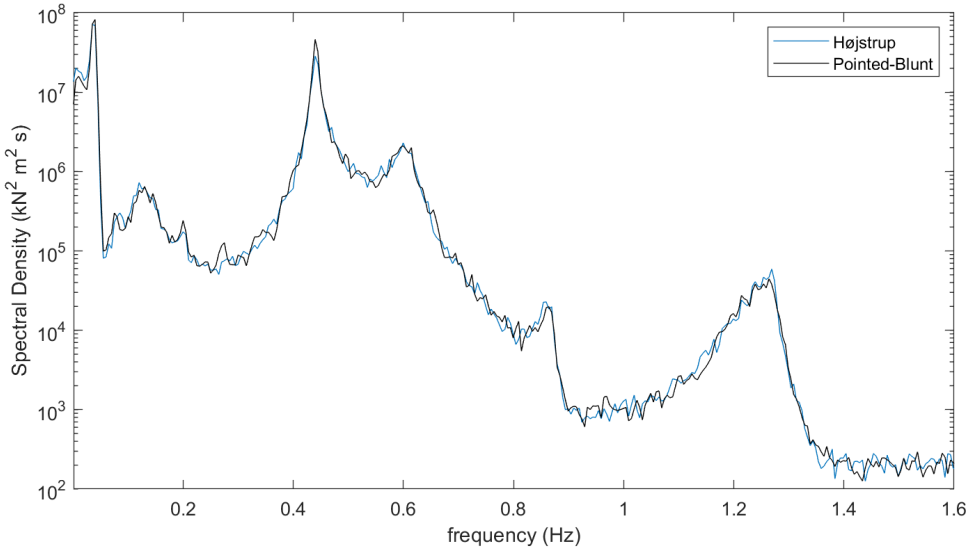

Figure A.11: Spectral Density for Tower Base Side-side Moment, 15m/s, Neutral Conditions

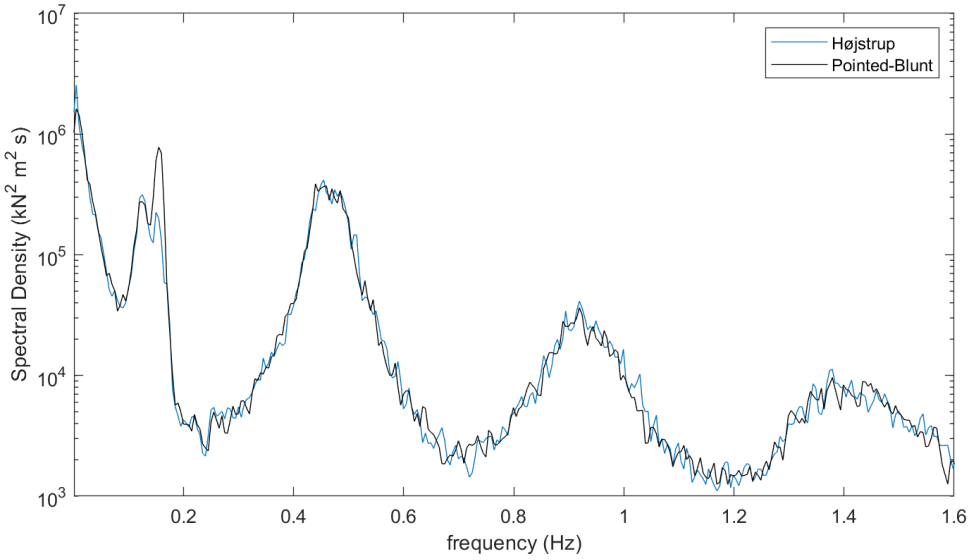

Figure A.12: Spectral Density for Tower Top Torsion Moment, 8m/s, Neutral Conditions

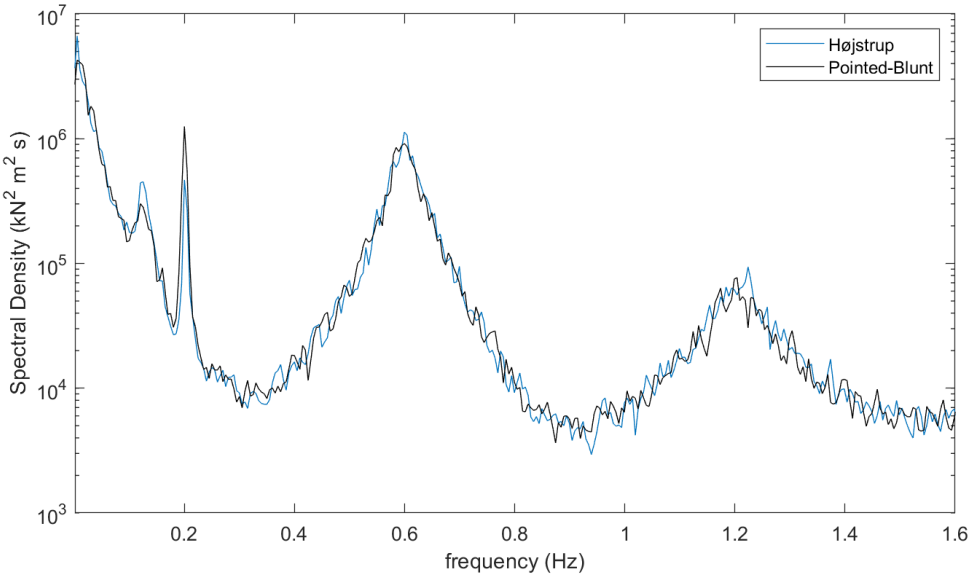

Figure A.13: Spectral Density for Tower Top Torsion Moment, 11.4m/s, Neutral Conditions

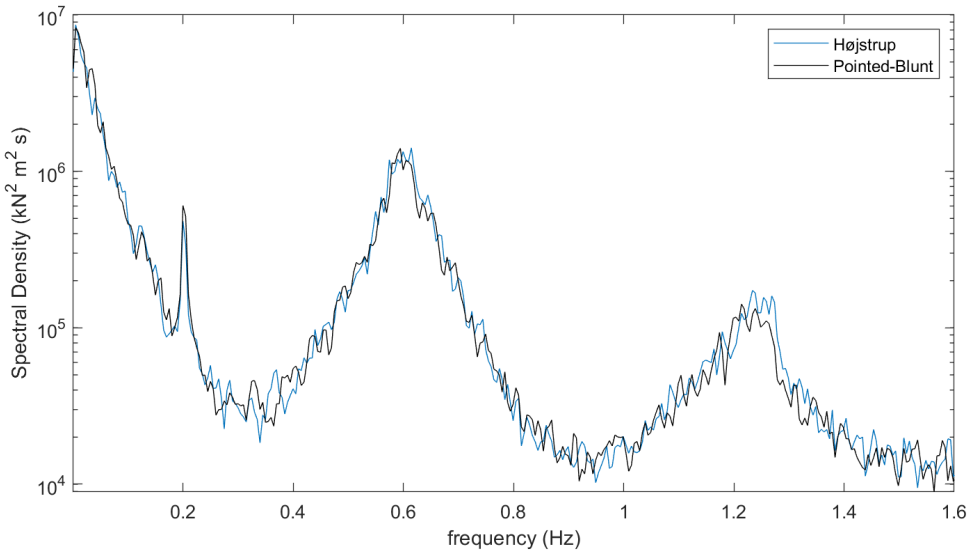

Figure A.14: Spectral Density for Tower Top Torsion Moment, 15m/s, Neutral Conditions

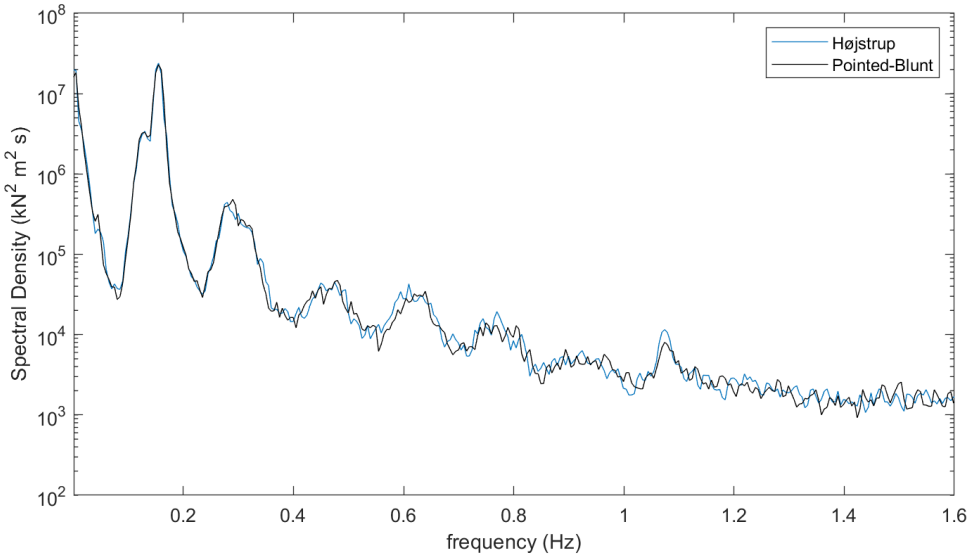

Figure A.15: Spectral Density for Blade Root Flap-Wise Moment, 8m/s, Neutral Conditions

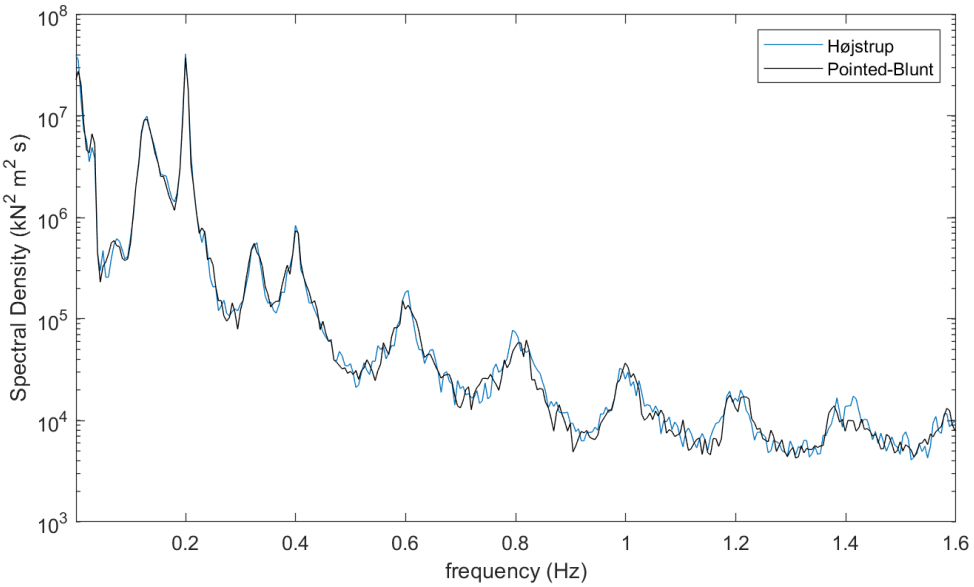

Figure A.16: Spectral Density for Blade Root Flap-Wise, 11.4m/s, Neutral Conditions

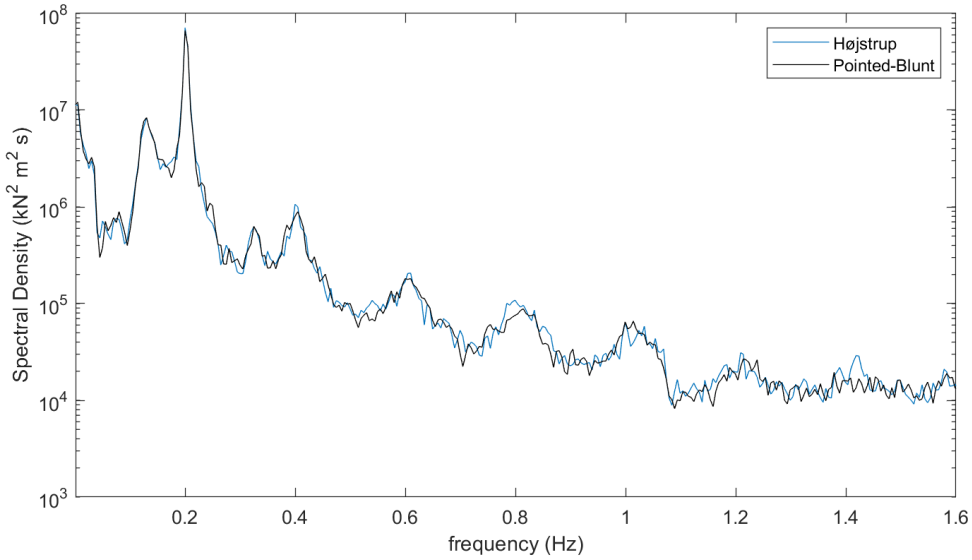

Figure A.17: Spectral Density for Blade Root Flap-Wise, 15m/s, Neutral Conditions

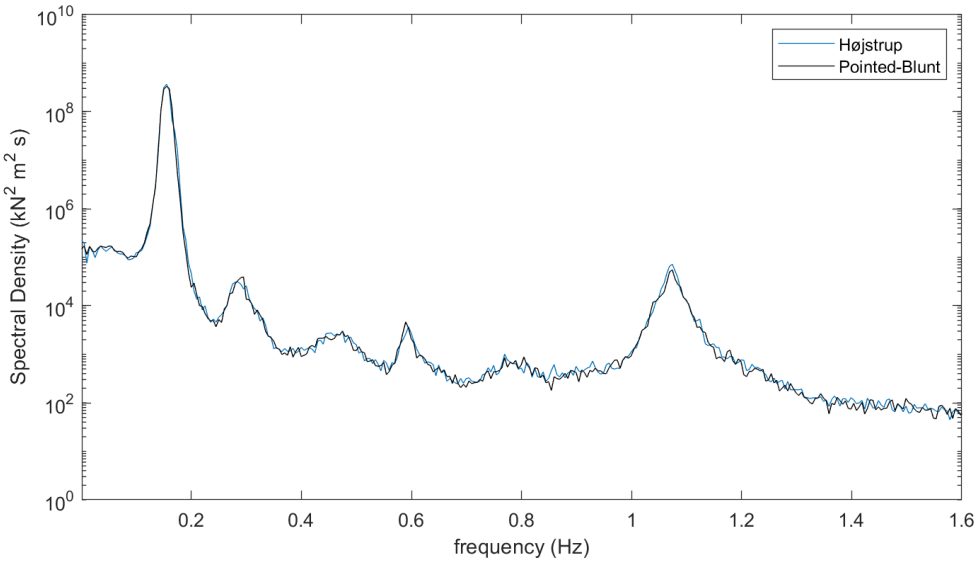

Figure A.18: Spectral Density for Blade Root Edge-Wise Moment, 8m/s, Neutral Conditions

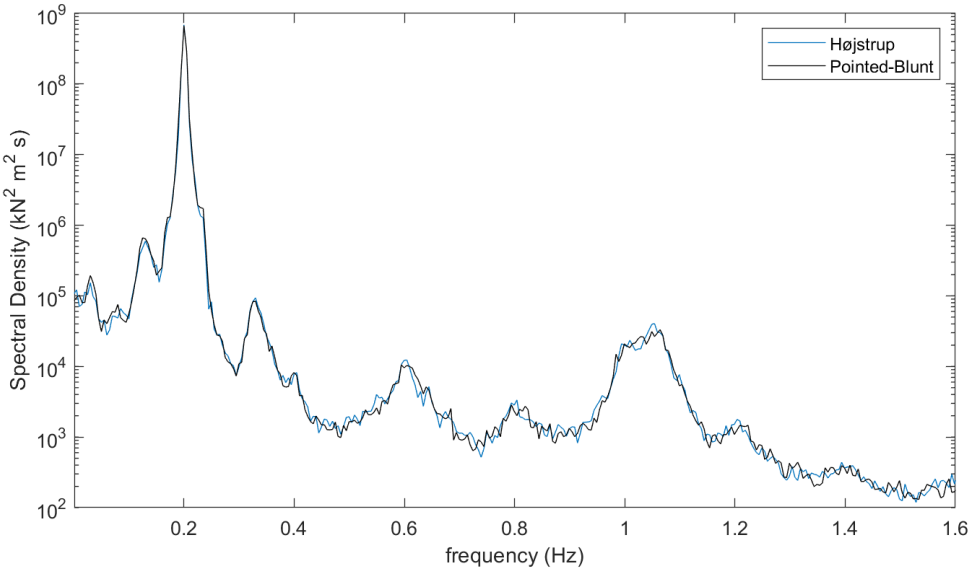

Figure A.19: Spectral Density for Blade Root Edge-Wise, 11.4m/s, Neutral Conditions

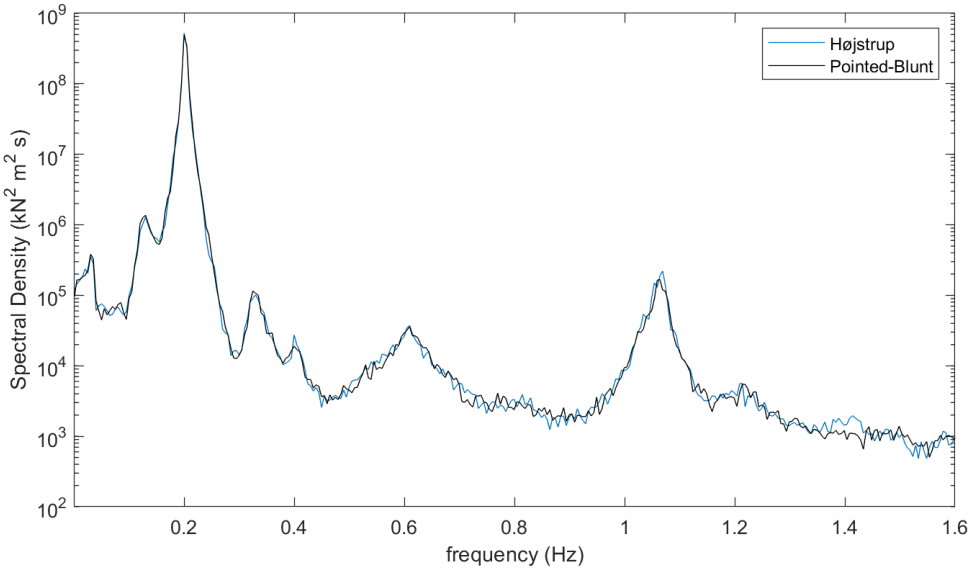

Figure A.20: Spectral Density for Blade Root Edge-Wise, 15m/s, Neutral Conditions

A.2.2 Højstrup's Model, Varying Atmospheric Conditions

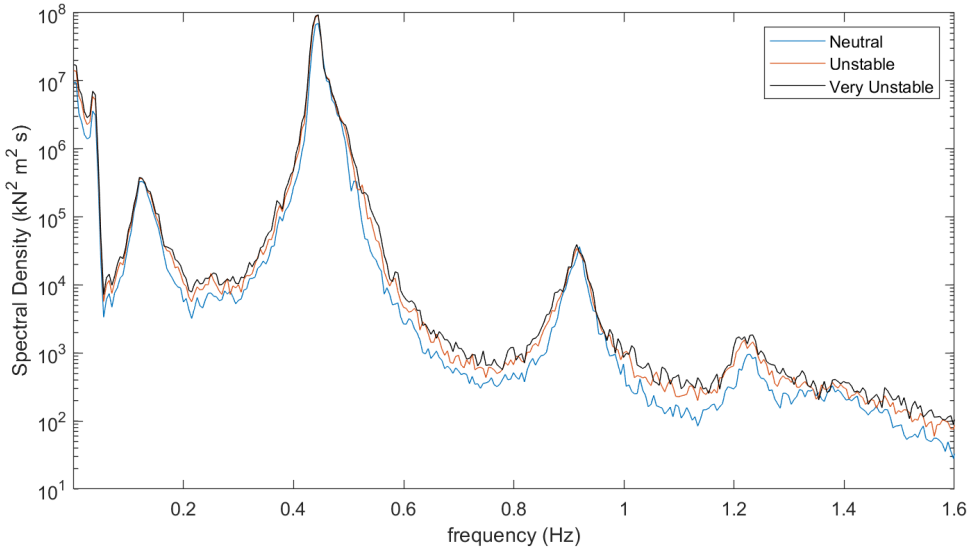

Figure A.21: Spectral Density for Tower Base Side-Side Moment, Højstrup's Model, 8m/s

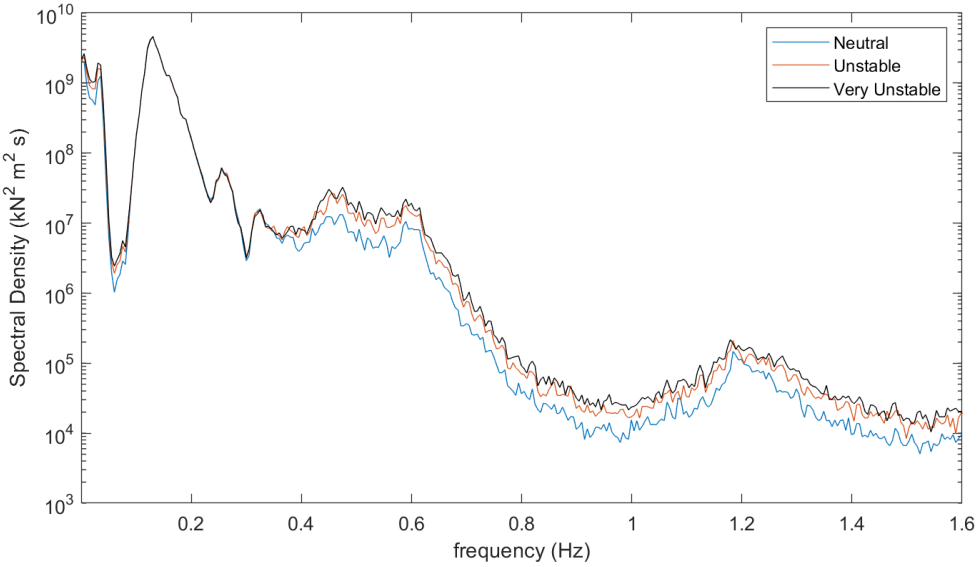

Figure A.22: Spectral Density for Tower Base Side-Side Moment, Højstrup's Model, 11.4m/s

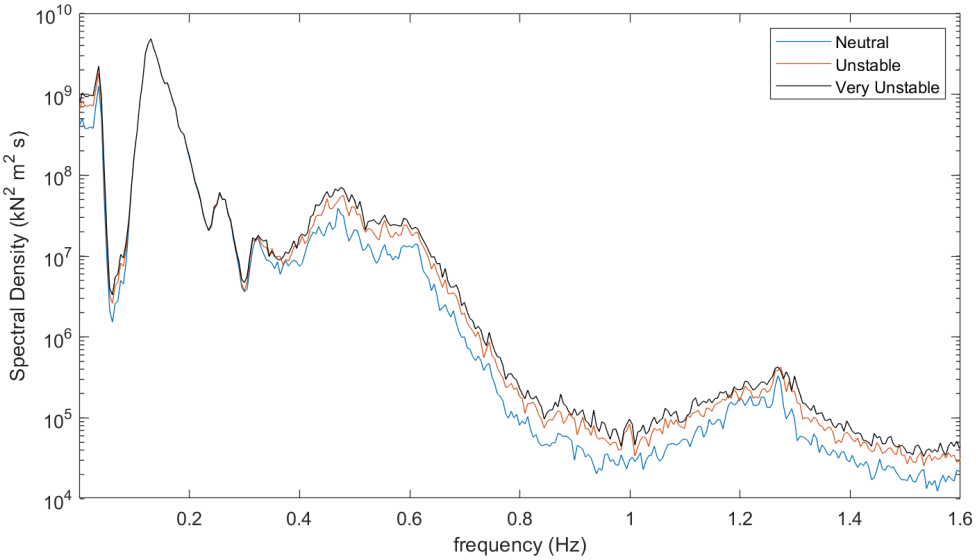

Figure A.23: Spectral Density for Tower Base Side-Side Moment, Højstrup's Model, 15m/s

The tower top torsion moment is mainly influenced by 3P and 6P frequencies. The wave spectral

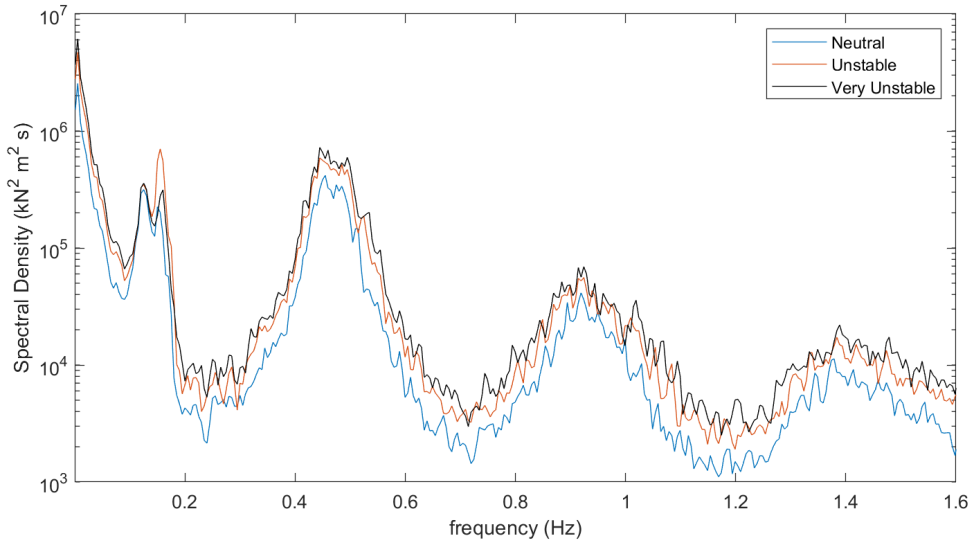

Figure A.24: Spectral Density for Tower Top Torsion, Højstrup's Model, 8m/s

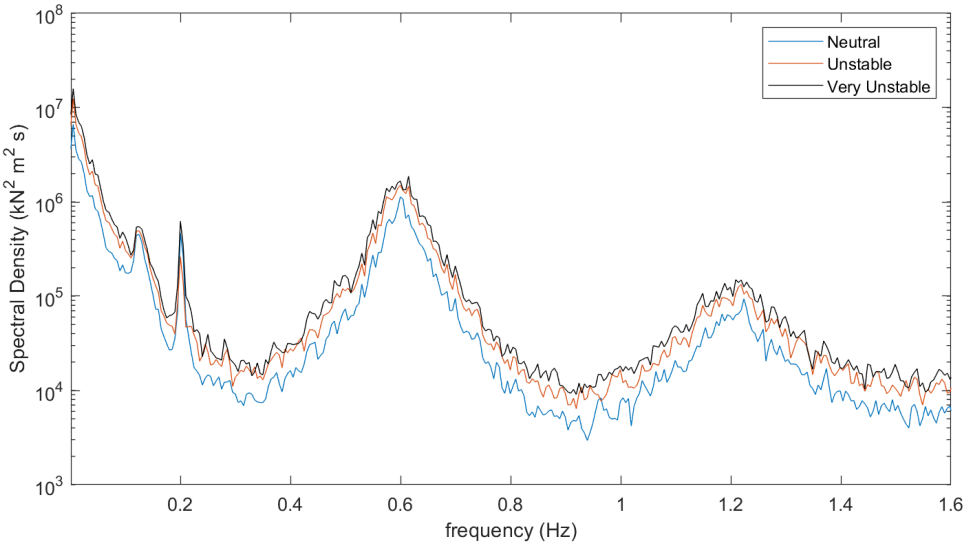

Figure A.25: Spectral Density for Tower Top Torsion, Højstrup's Model, 11.4m/s

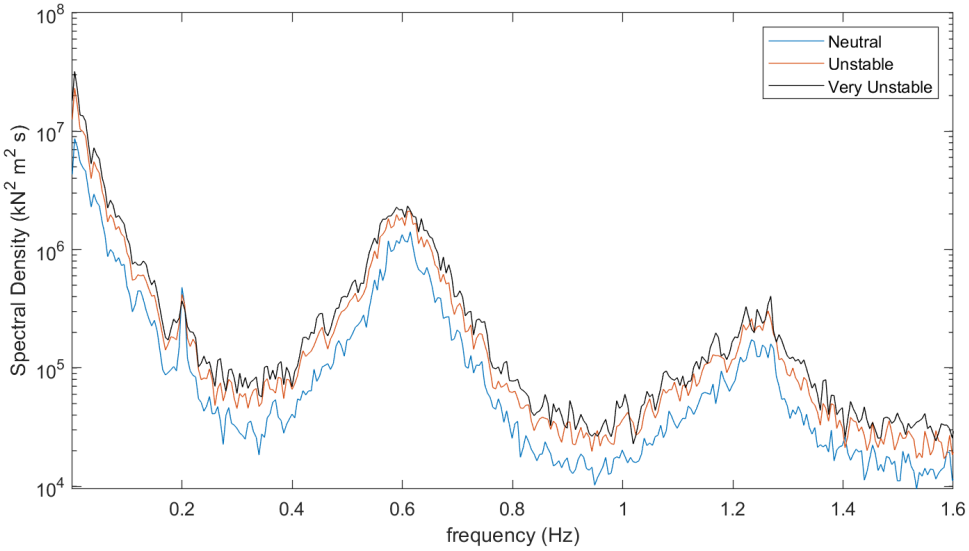

Figure A.26: Spectral Density for Tower Top Torsion, Højstrup's Model, 15m/s

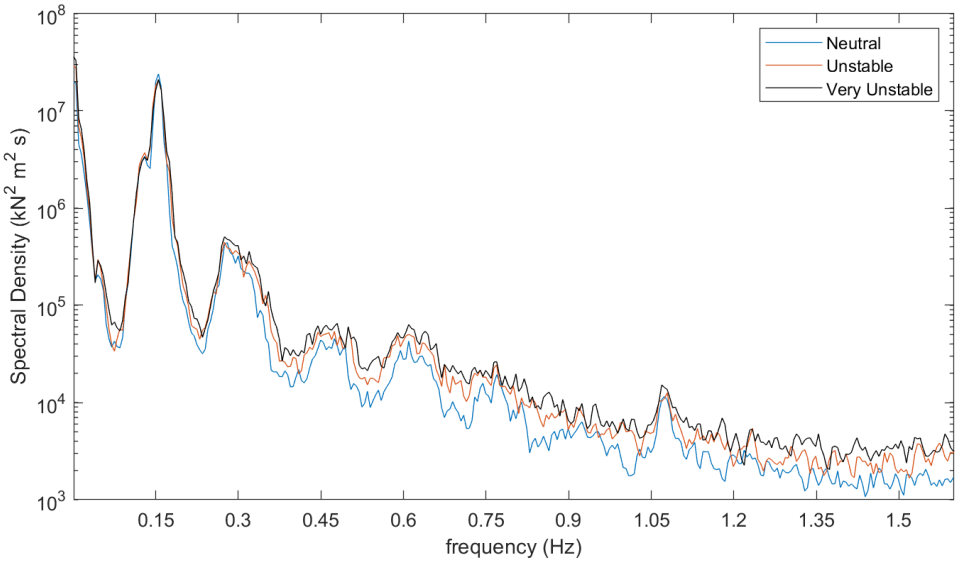

Figure A.27: Spectral Density for Blade Root Flap-Wise Moment, Højstrup's Model, 8m/s

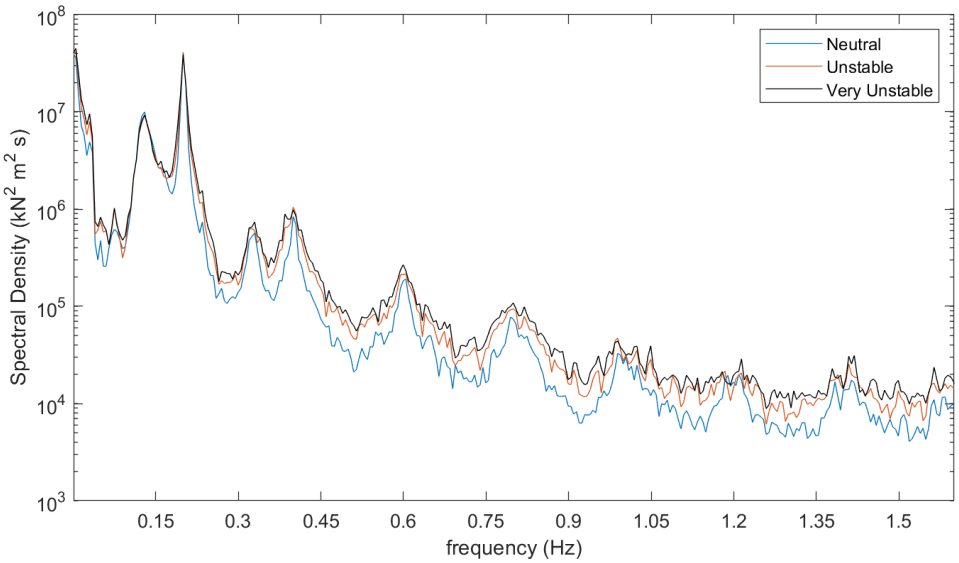

Figure A.28: Spectral Density for Blade Root Flap-Wise Moment, Højstrup's Model, 11.4m/s

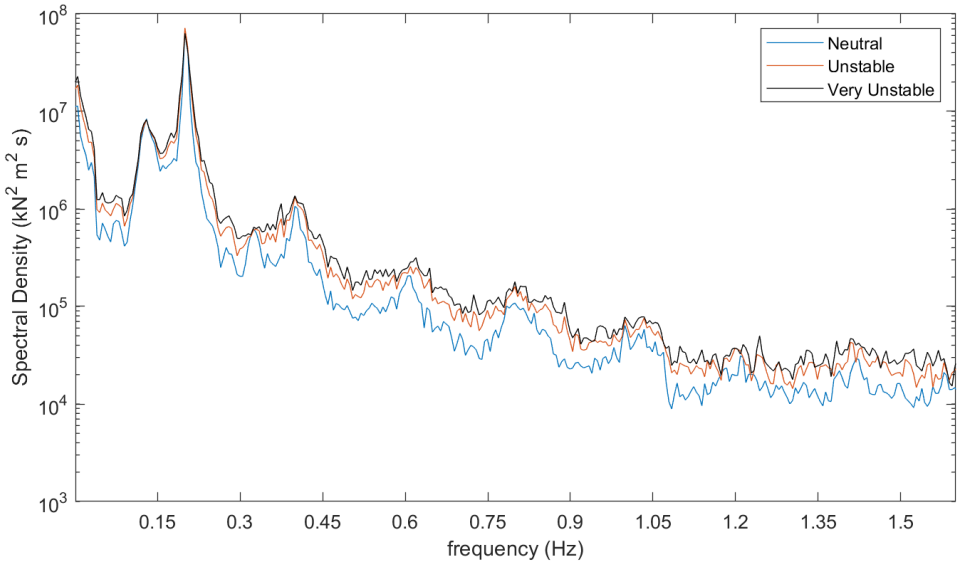

Figure A.29: Spectral Density for Blade Root Flap-Wise Moment, Højstrup's Model, 15m/s

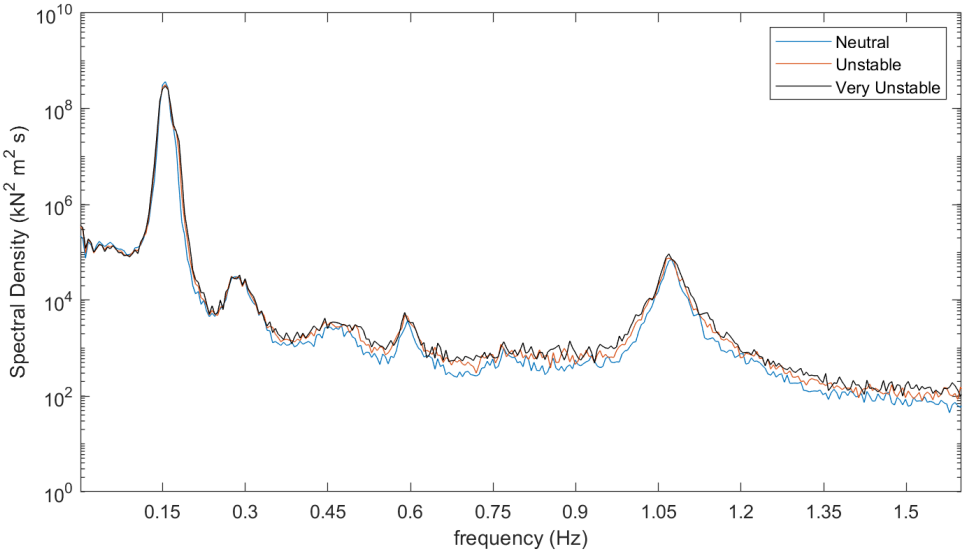

Figure A.30: Spectral Density for Blade Root Edge-Wise Moment, Højstrup's Model, 8m/s

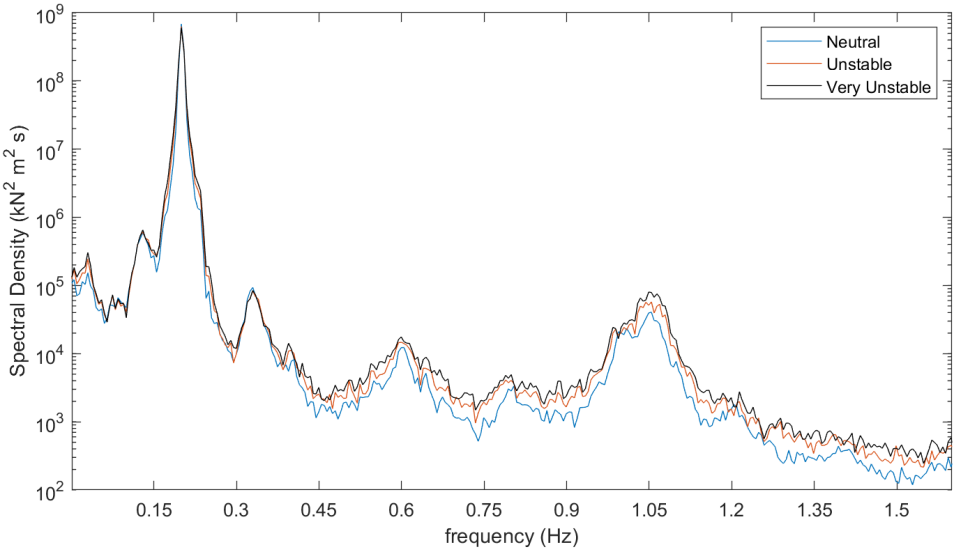

Figure A.31: Spectral Density for Blade Root Edge-Wise Moment, Højstrup's Model, 11.4m/s

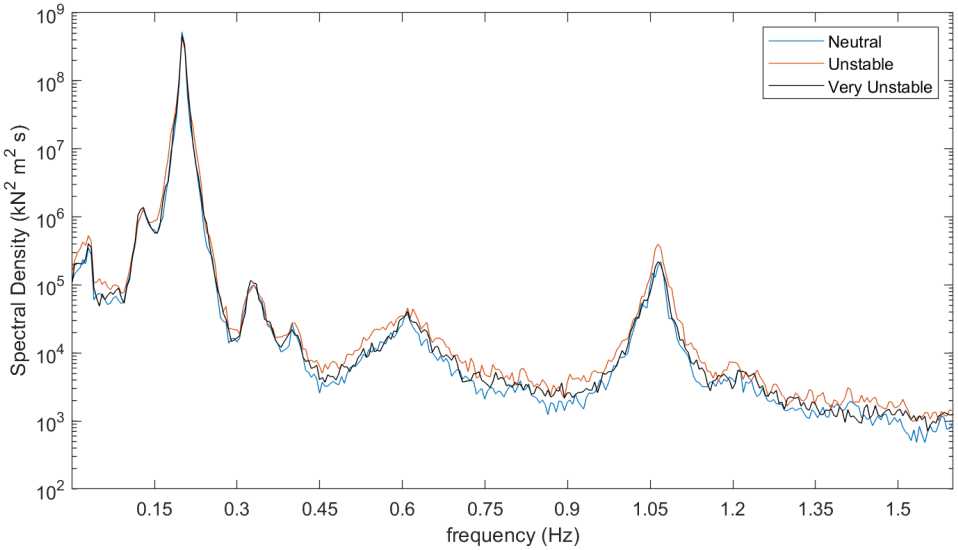

Figure A.32: Spectral Density for Blade Root Edge-Wise Moment, Højstrup's Model, 15m/s

A.2.3 Pointed-Blunt Model, Varying Atmospheric Conditions

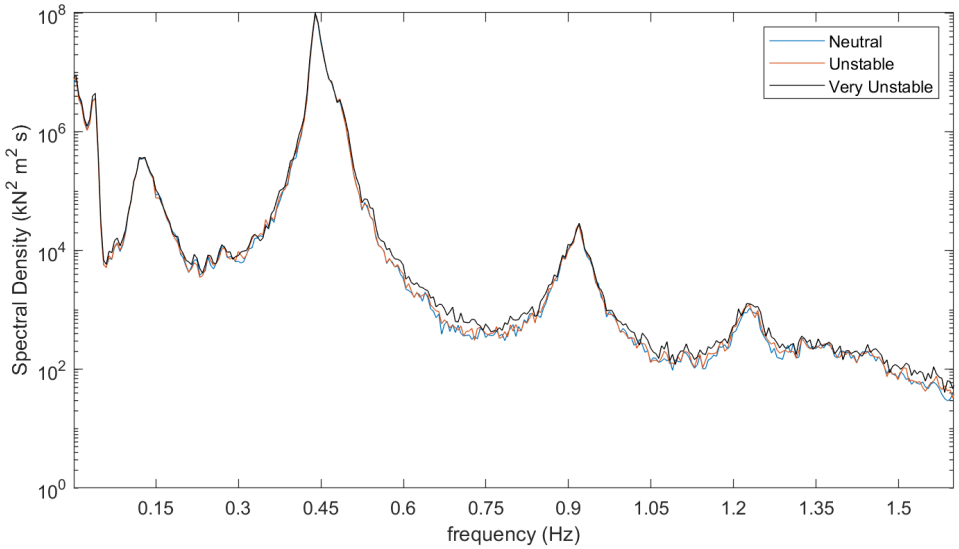

Figure A.33: Spectral Density for Tower Base Side-Side Moment, Pointed-Blunt Model, 8m/s

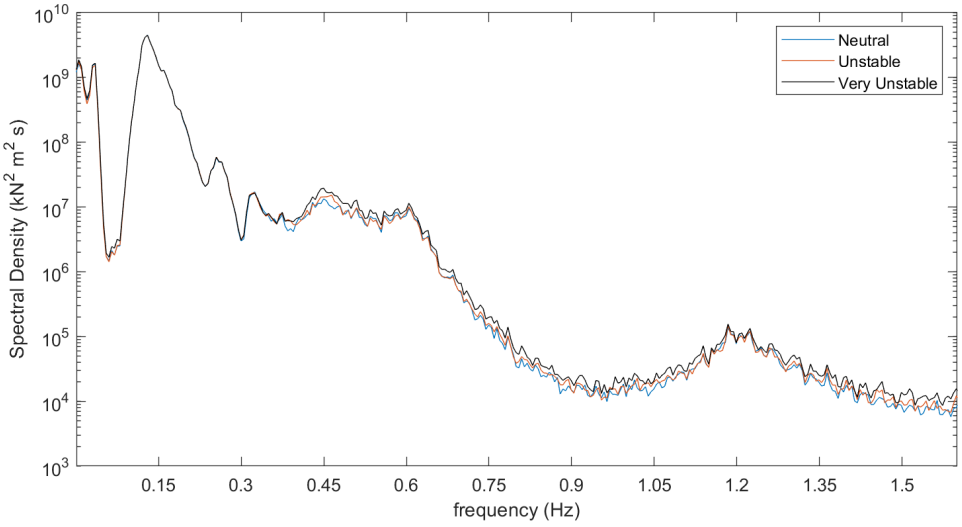

Figure A.34: Spectral Density for Tower Base Side-Side Moment, Pointed-Blunt Model, 11.4m/s

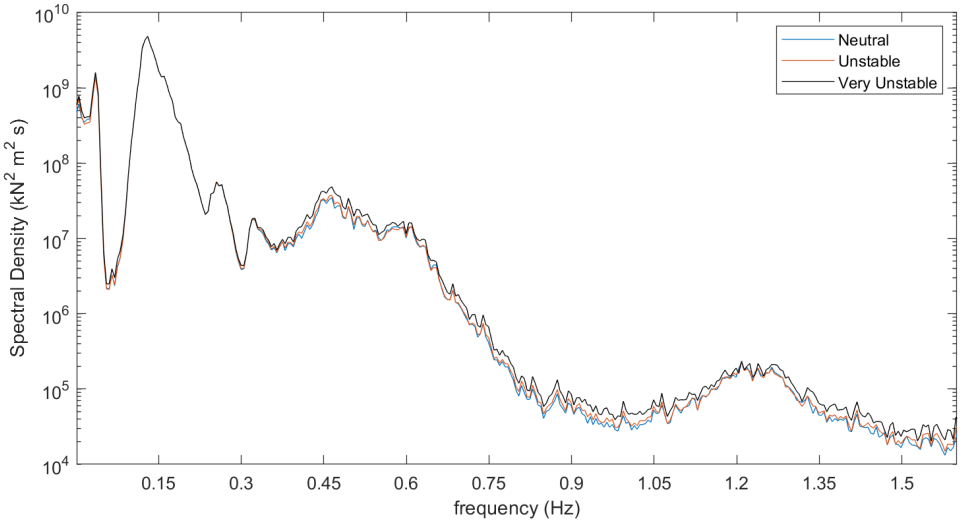

Figure A.35: Spectral Density for Tower Base Side-Side Moment, Pointed-Blunt Model, 15m/s

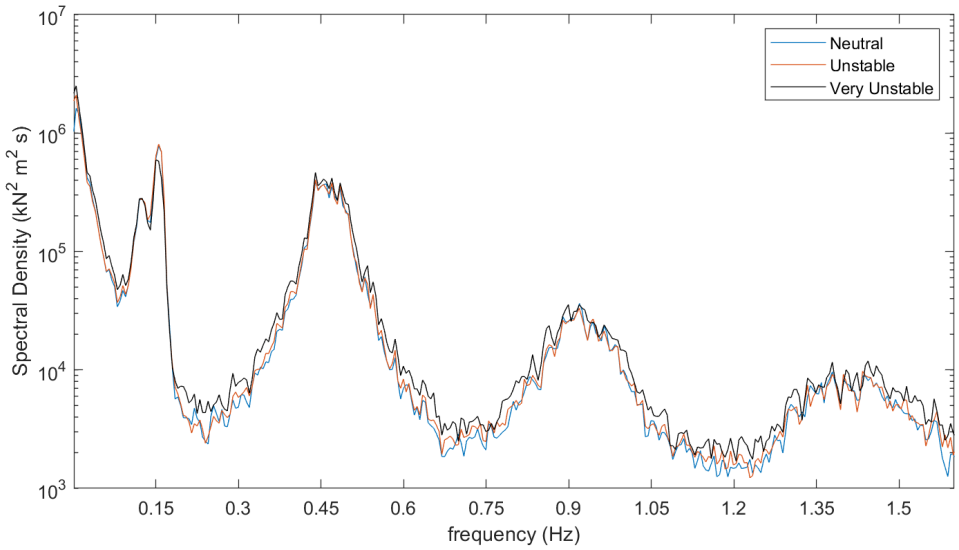

Figure A.36: Spectral Density for Tower Top Torsion, Pointed-Blunt Model, 8m/s

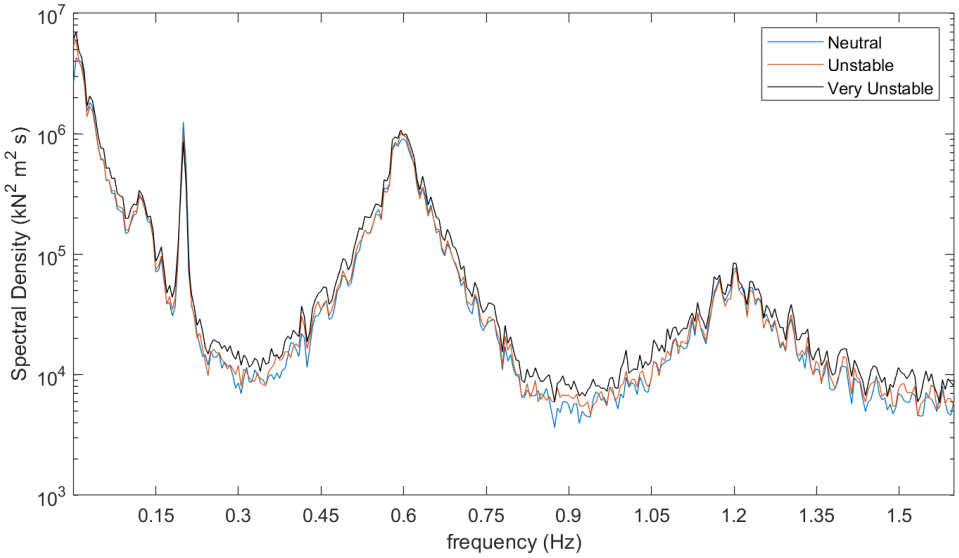

Figure A.37: Spectral Density for Tower Top Torsion, Pointed-Blunt Model, 11.4m/s

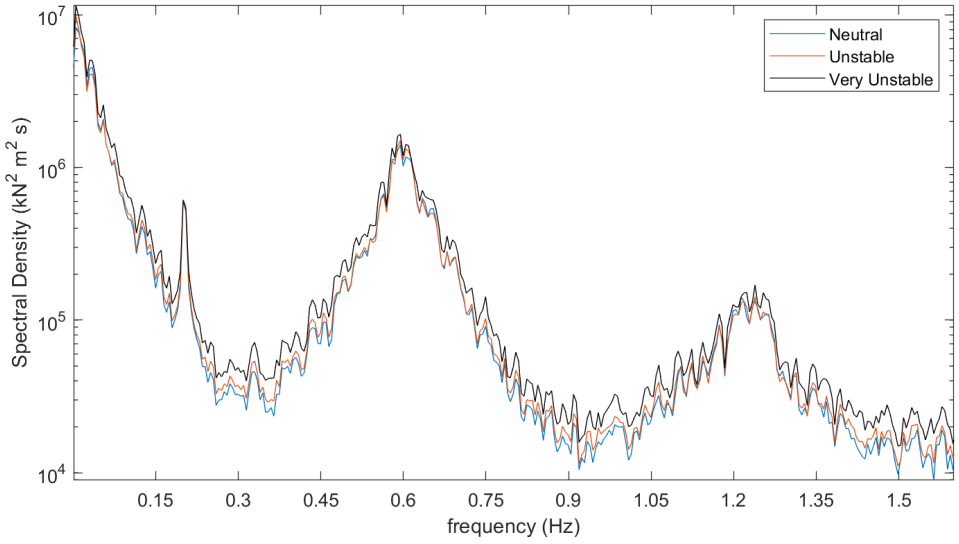

Figure A.38: Spectral Density for Tower Top Torsion, Pointed-Blunt Model, 15m/s

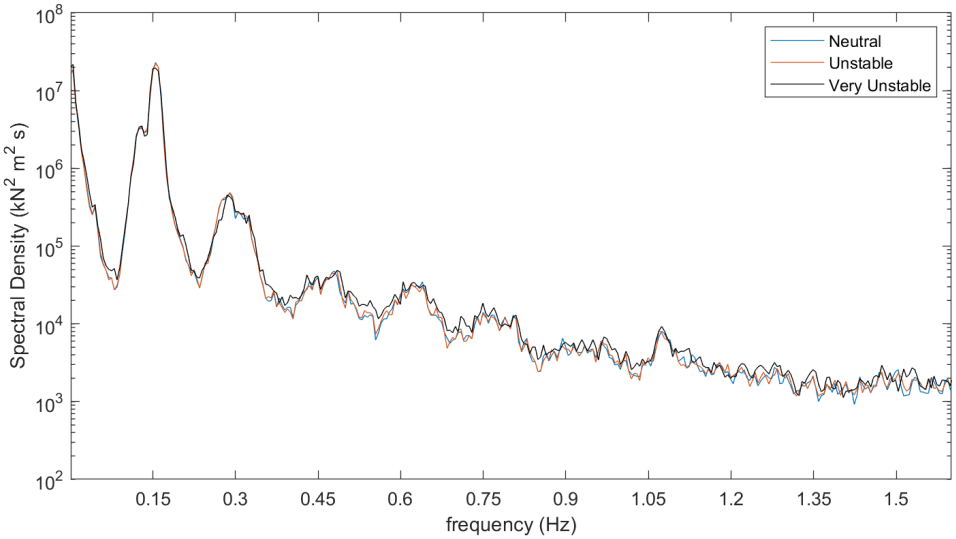

Figure A.39: Spectral Density for Blade Root Flap-Wise Moment, Pointed-Blunt Model, 8m/s

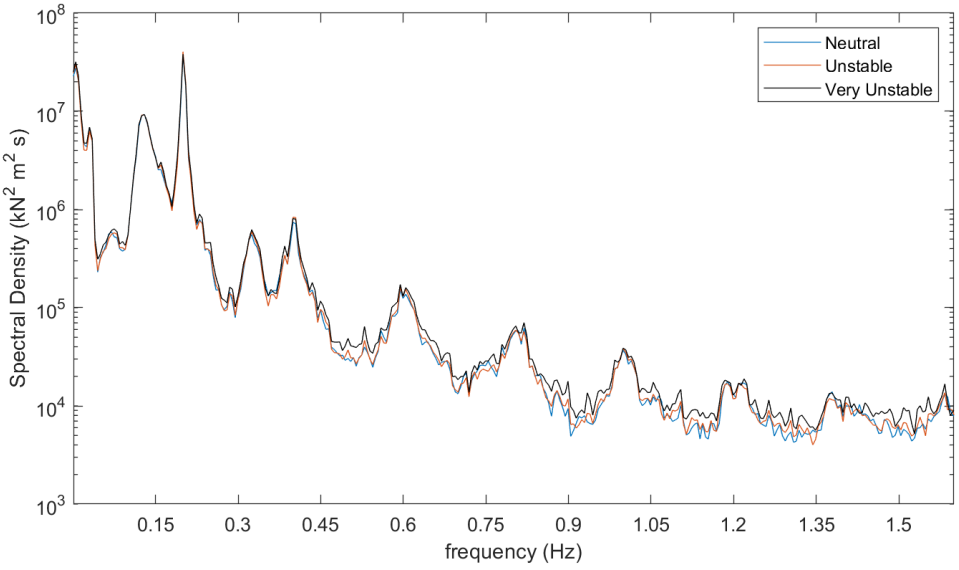

Figure A.40: Spectral Density for Blade Root Flap-Wise Moment, Pointed-Blunt Model, 11.4m/s

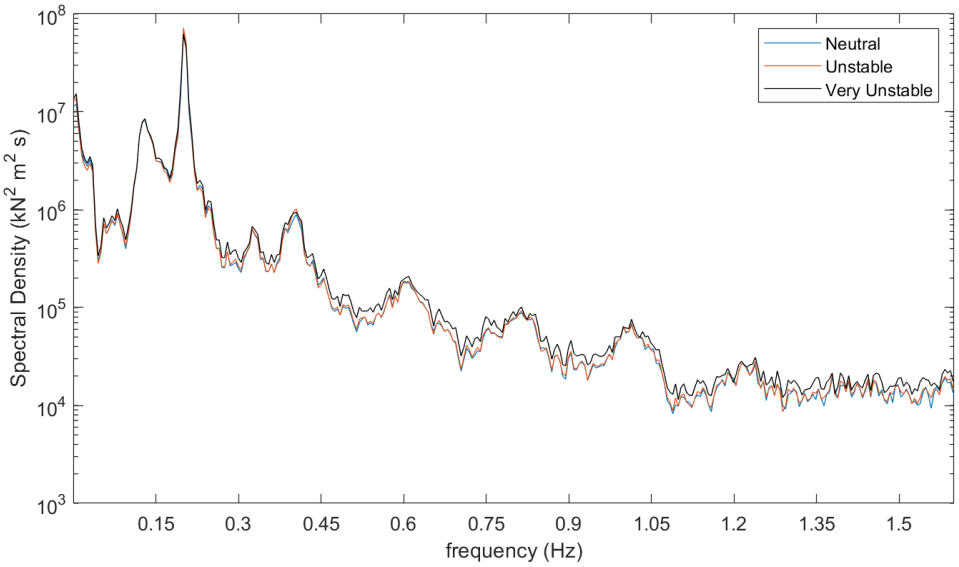

Figure A.41: Spectral Density for Blade Root Flap-Wise Moment, Pointed-Blunt Model, 15m/s

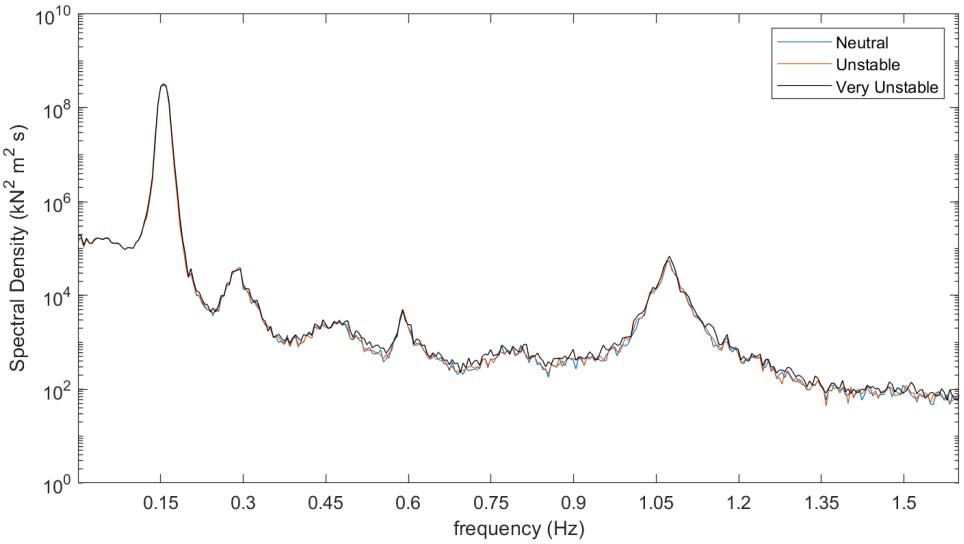

Figure A.42: Spectral Density for Blade Root Edge-Wise Moment, Pointed-Blunt Model, 8m/s

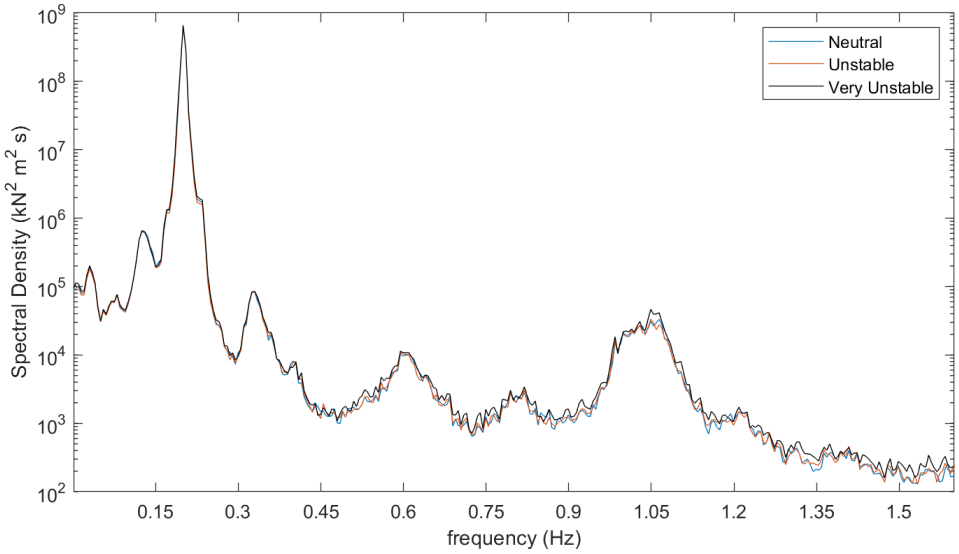

Figure A.43: Spectral Density for Blade Root Edge-Wise Moment, Pointed-Blunt Model, 11.4m/s

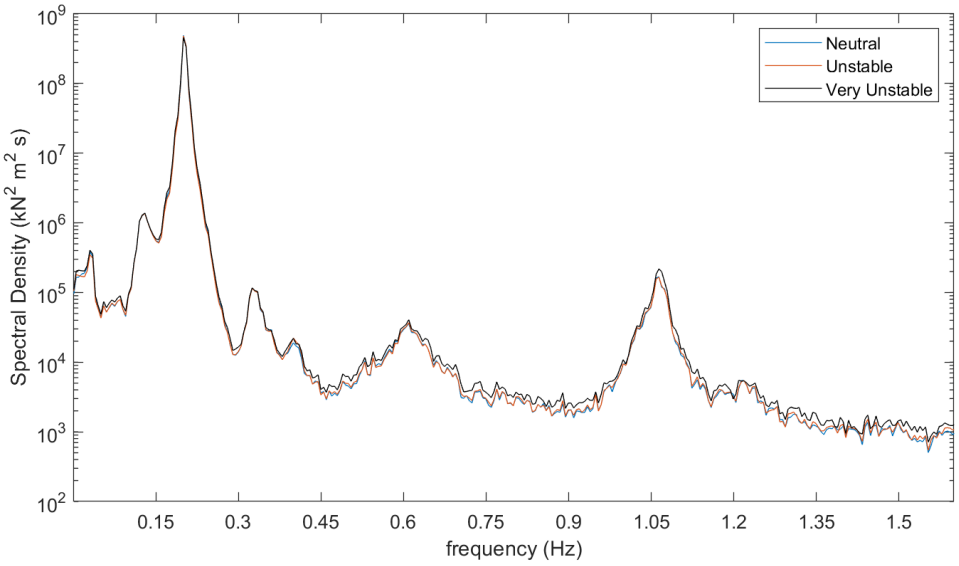

Figure A.44: Spectral Density for Blade Root Edge-Wise Moment, Pointed-Blunt Model, 15m/s

A.3 Damage Equivalent Loads

A.3.1 Neutral DELs

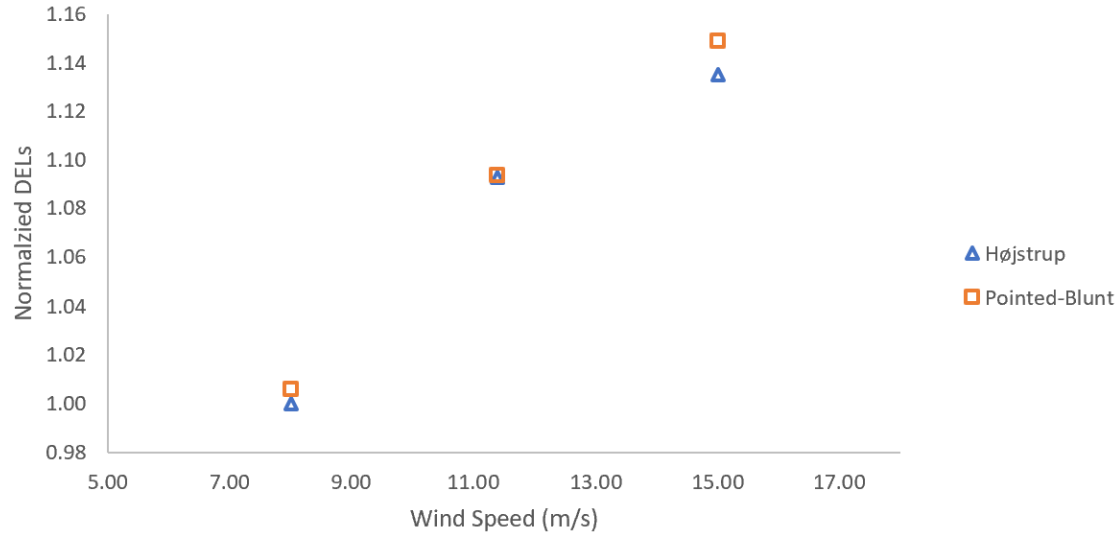

Figure A.45: DEL for the Tower Base Fore-Aft Moment, Neutral Conditions

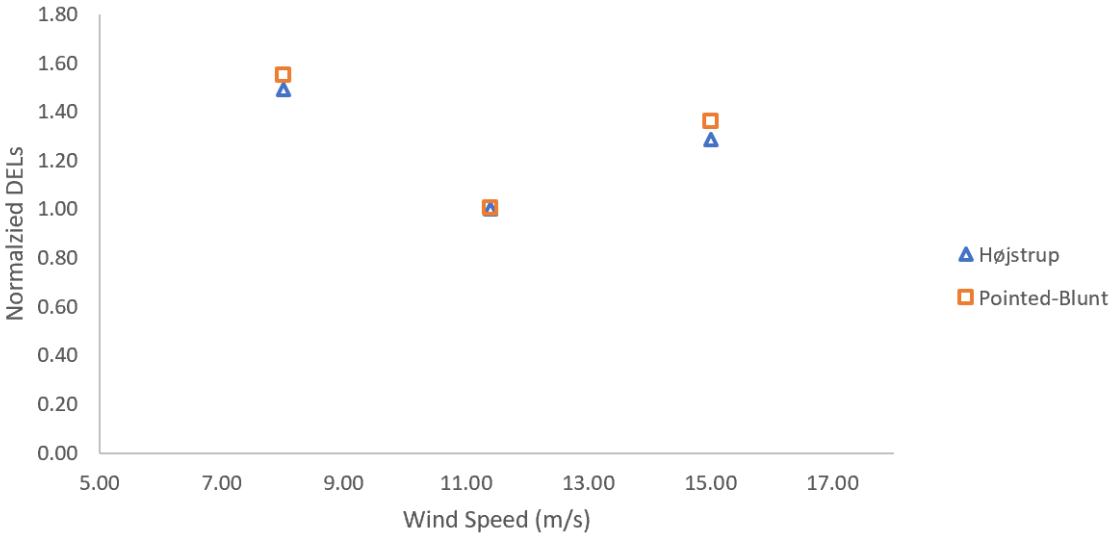

Figure A.46: DEL for the Tower Base Side-Side Moment, Neutral Conditions

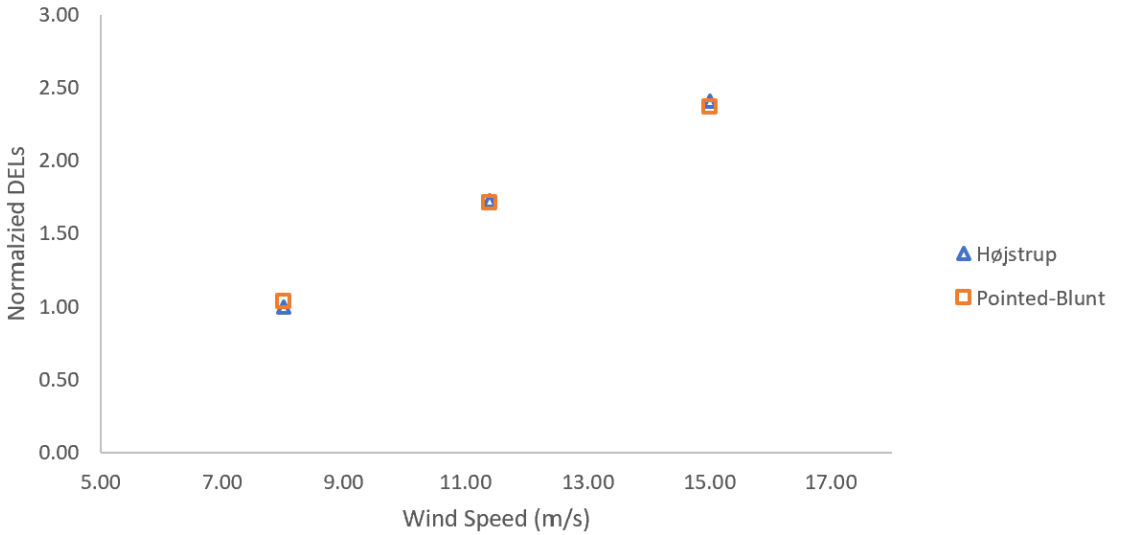

Figure A.47: DEL for the Tower Top Torsion, Neutral Conditions

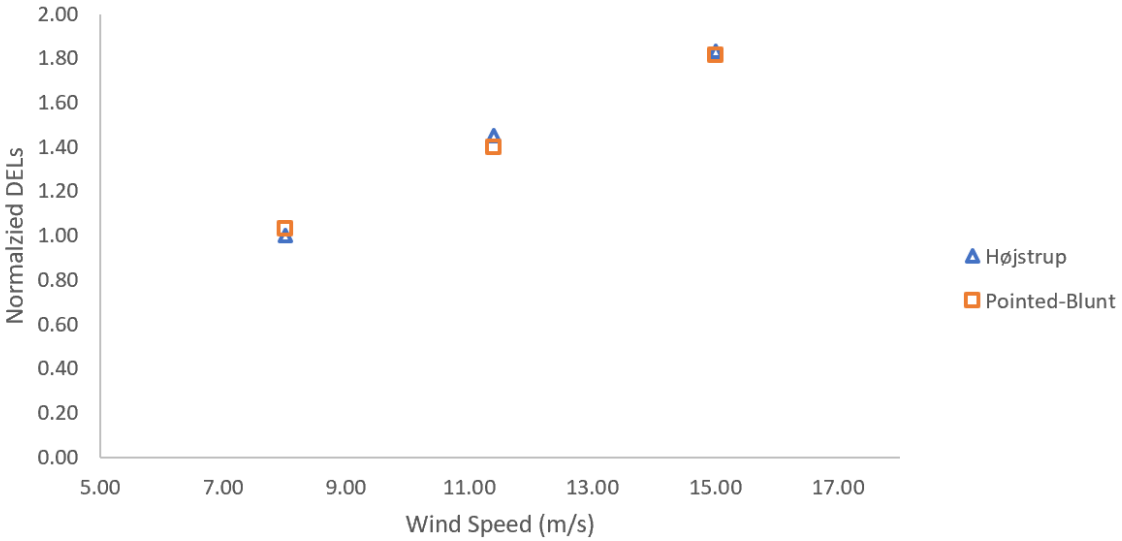

Figure A.48: DEL for the Blade Root Flap-Wise Moment, Neutral Conditions

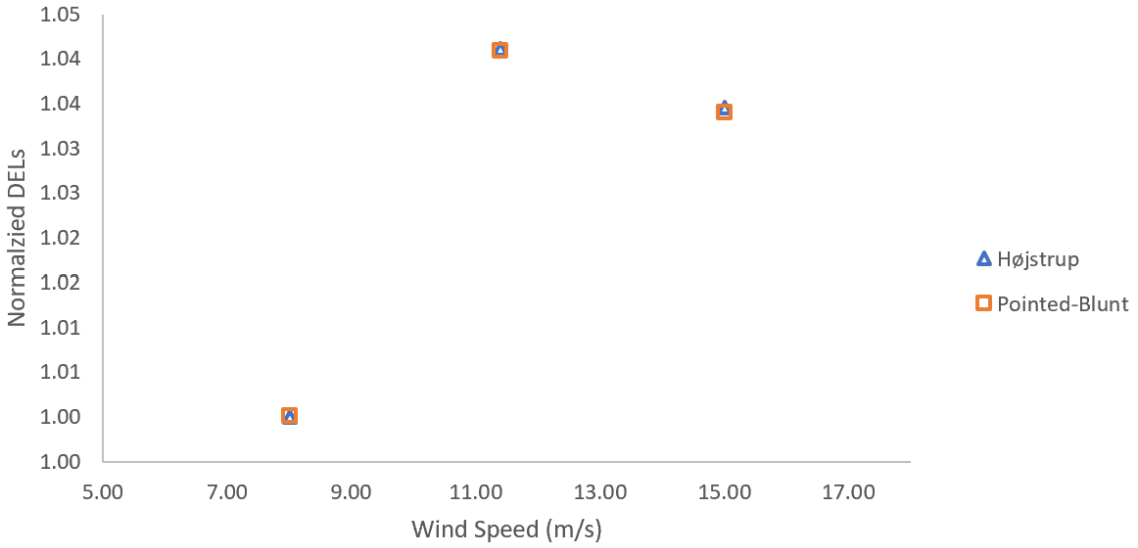

Figure A.49: DEL for the Blade Root Edge-Wise Moment, Neutral Conditions

A.3.2 Højstrup Normalized DELs

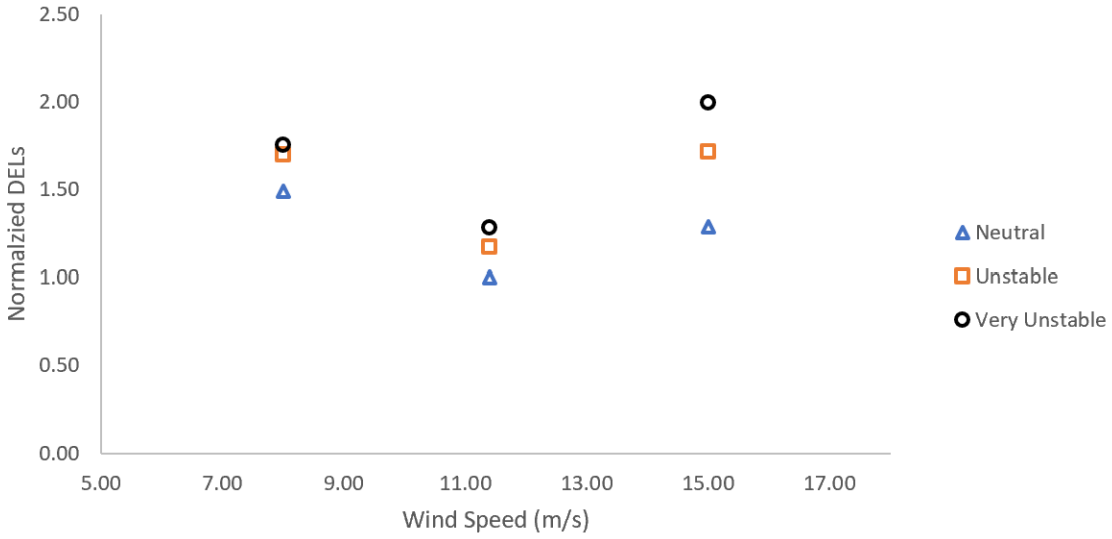

Figure A.50: DEL for the Tower Base Side-Side Moment, Højstrup's Unstable Spectra Model

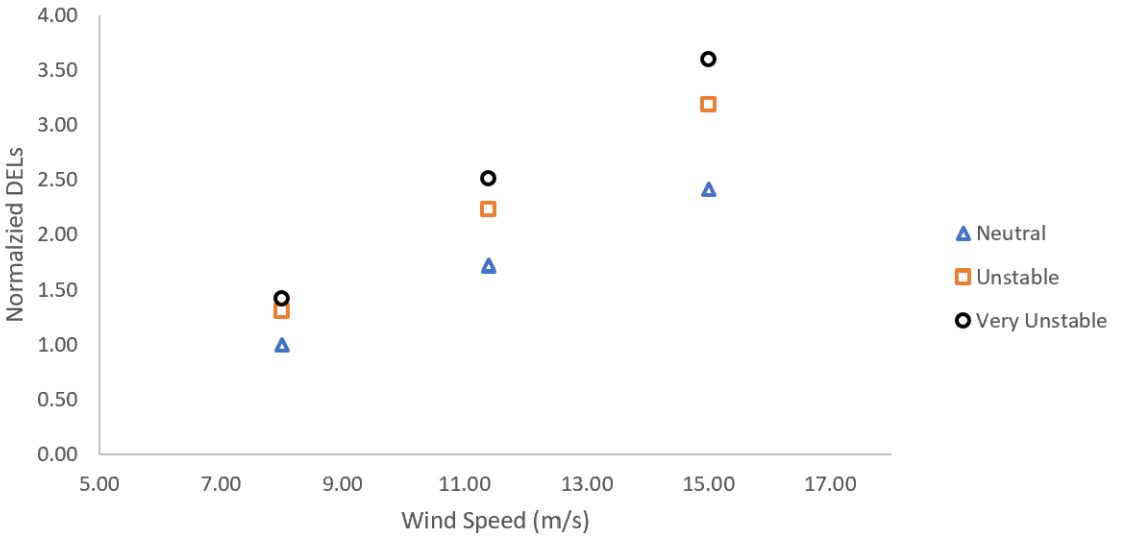

Figure A.51: DEL for the Tower Top Torsion, Højstrup's Unstable Spectra Model

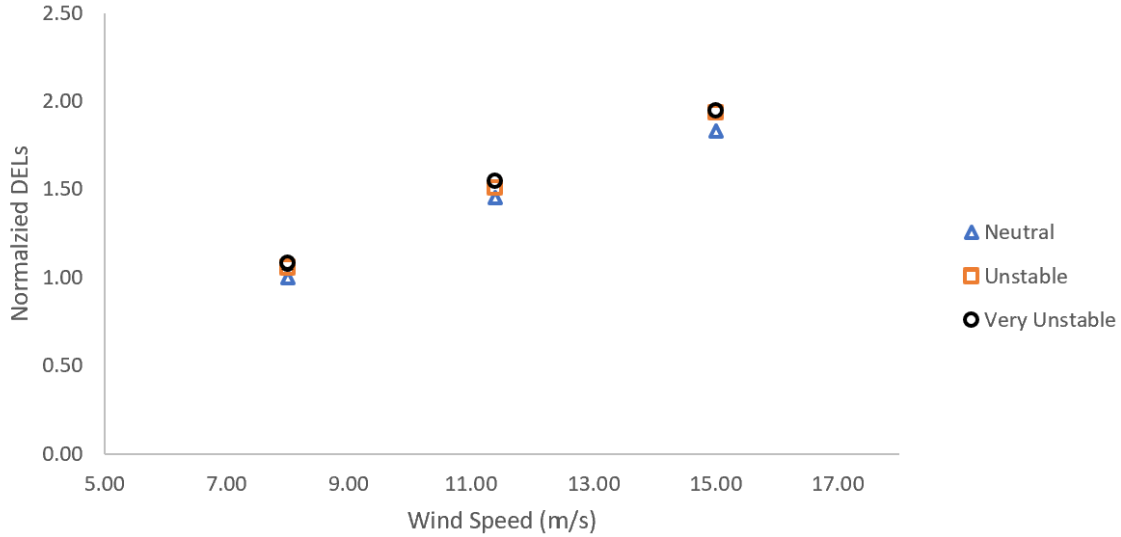

Figure A.52: DEL for the Blade Root Flap-Wise Moment, Højstrup's Unstable Spectra Model

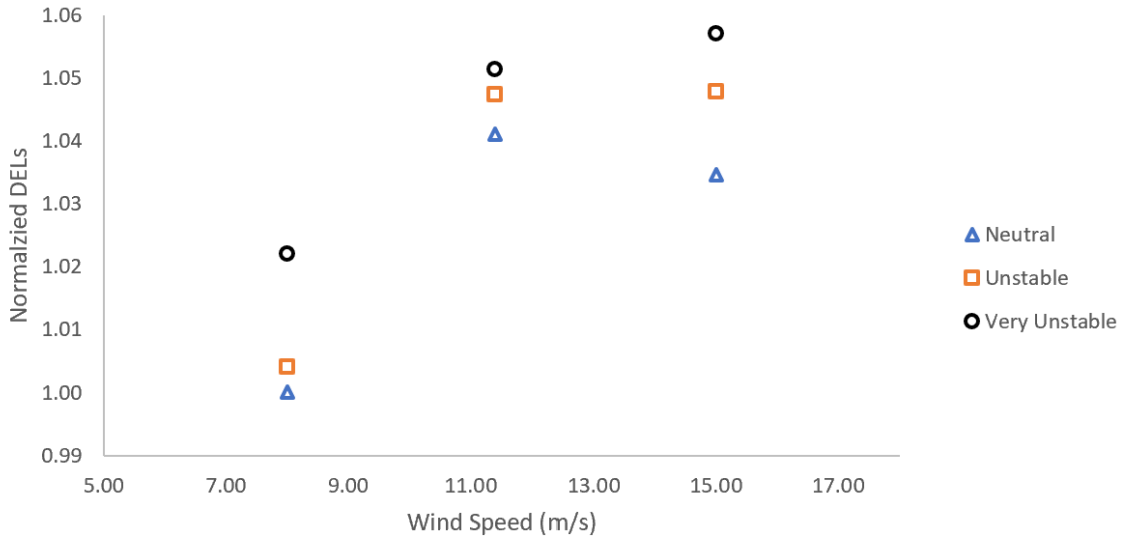

Figure A.53: DEL for the Blade Root Edge-Wise Moment, Højstrup's Unstable Spectra Model

A.3.3 Pointed-Blunt Normalized DELs

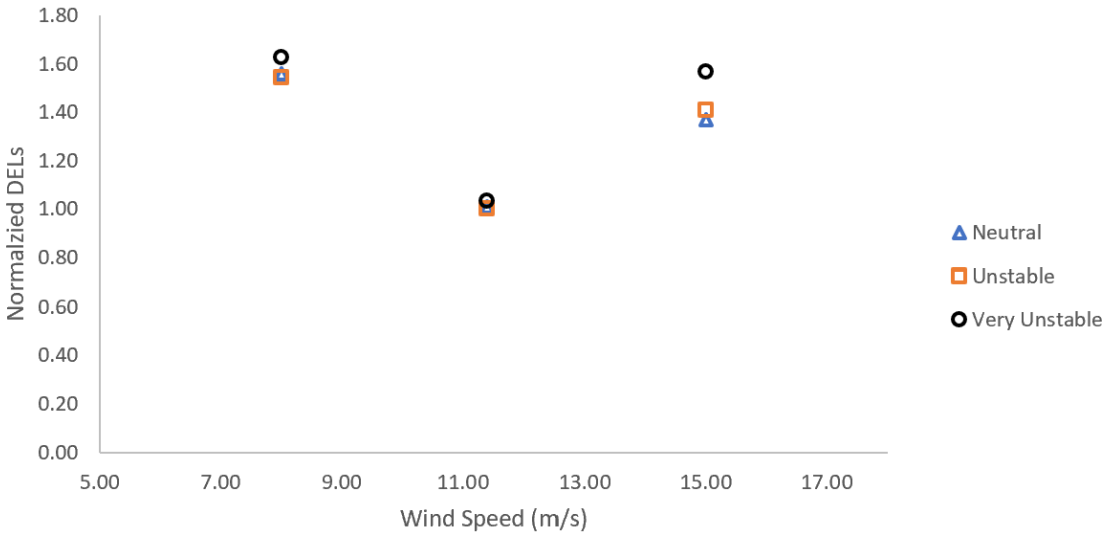

Figure A.54: DEL for the Tower Base Side-Side Moment, Pointed-Blunt Model

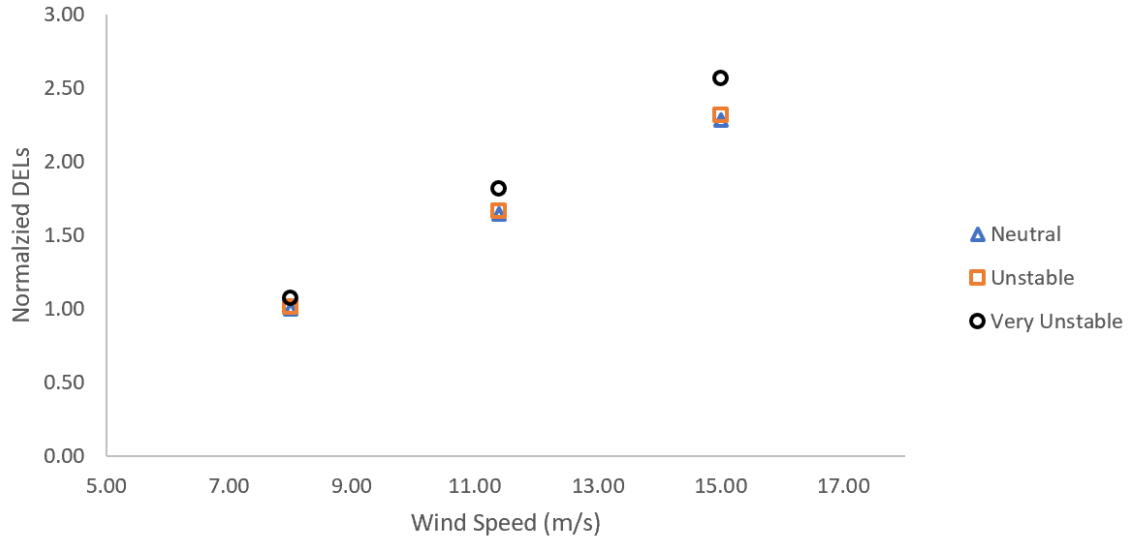

Figure A.55: DEL for the Tower Top Torsion, Pointed-Blunt Model

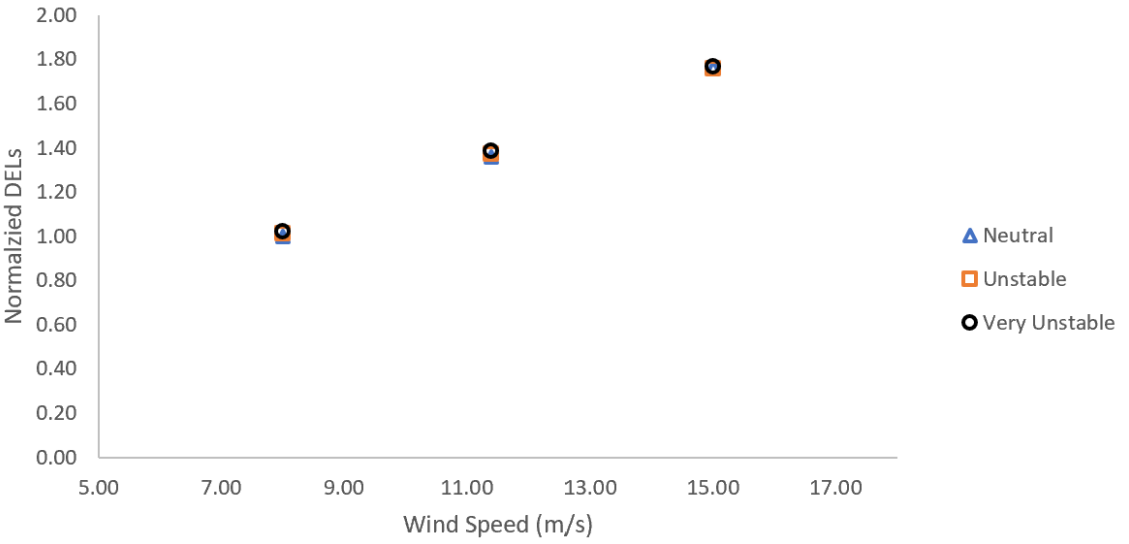

Figure A.56: DEL for the Blade Root Flap-Wise Moment, Pointed-Blunt Model

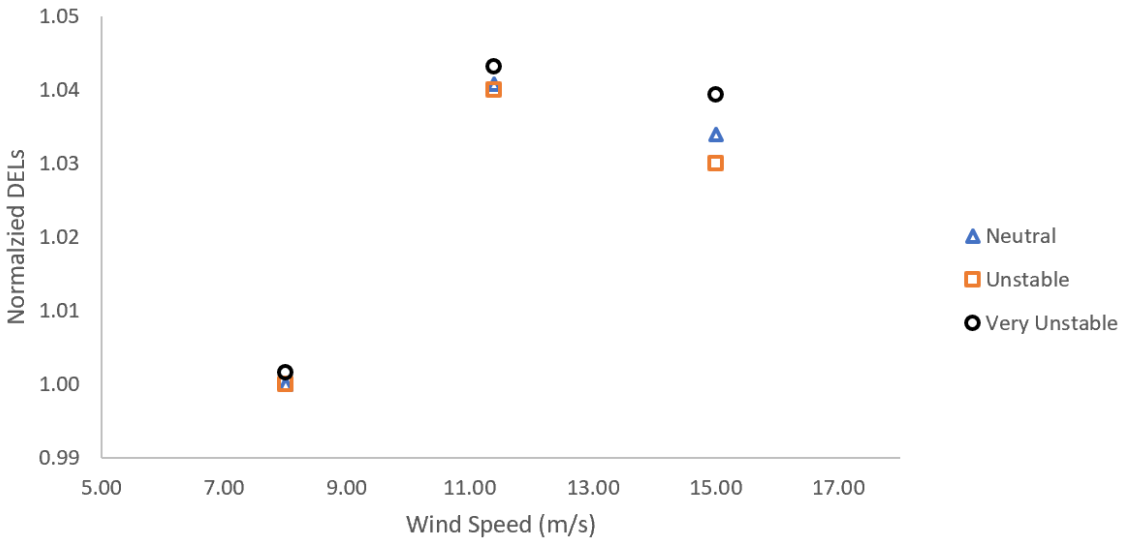

Figure A.57: DEL for the Blade Root Edge-Wise Moment, Pointed-Blunt Model